UNIVERSITY OF SOUTHAMPTON

FACULTY OF PHYSICAL SCIENCES AND ENGINEERING

Electronics and Computer Science

A Bayesian Approach to Characterize Fold Change Detection in *Dictyostelium Discoideum*

by

Muhammad Shahreeza Safiruz Bin Kassim

Thesis for the degree of Doctor of Philosophy

December 2018

UNIVERSITY OF SOUTHAMPTON

ABSTRACT

FACULTY OF PHYSICAL SCIENCES AND ENGINEERING
Electronics and Computer Science

Doctor of Philosophy

A BAYESIAN APPROACH TO CHARACTERIZE FOLD CHANGE DETECTION IN *DICTYOSTELIUM DISCOIDEUM*

by Muhammad Shahreeza Safiruz Bin Kassim

The survivability of *Dictyostelium* cells is highly dependent on how cells sense and response to cyclic-AMP chemoattractant. A key factor in the sense-response mechanism is a feature called 'fold change detection' (FCD), where cells response to the fold changes in stimulus as opposed to its absolute values. Studies have proposed models of the signalling pathway for the sense-response mechanism and skeletal network motifs that exhibit FCD. However, FCD properties in models of sense-response mechanism compatible with experiments that exhibit FCD are poorly understood. In this thesis, we characterize the properties of FCD of *Dictyostelium* cells by using a mathematical model of experiments that incorporates biochemical variables of the signalling pathway. We created a population of virtual cells by estimating posterior distributions of the model parameters using a Bayesian method. We studied the responses of the virtual cells to various fold changes in stimulus and found that the population of cells is more consistent in sensing lower fold changes. By computing the overlapping areas of distribution of responses we found that the population of cells can distinguish lower fold changes better than higher fold changes. We propose a hyperbolic equation to describe the stimulus-response relation with a logarithmic relation to characterize the uncertainties of the stimulus. We inferred the posterior probability of detecting fold changes using Bayes' theorem and introduce a novel model of prior probability of fold changes. We found that the chances of detecting lower fold changes is higher and posteriors are biased strongly by the conditional probability. To derive the population of cells' perception of fold change, a Bayesian Observer model is constructed and evaluated. It is found that the population of cells perceive uncertainties of lower fold changes better than higher fold changes. There is also a stark difference between perceptions derived from priors modelled from chemotaxis experiment and priors from known families of distribution. We quantified the biases in the perceptions and discovered that biases are more prominent in higher fold changes. The fold distinguishability threshold is also evaluated and its relation with the perceptual bias examined. Our work shows that the characterization of FCD in models of sense-response mechanism can derive theoretical insights not seen in experiments and impose constraints for model selection.

Contents

List of Figures

List of Tables

Declaration of Authorship

I, Muhammad Shahreeza Safiruz Bin Kassim , declare that the thesis entitled *A Bayesian Approach to Characterize Fold Change Detection in Dictyostelium Discoideum* and the work presented in the thesis are both my own, and have been generated by me as the result of my own original research. I confirm that:

- this work was done wholly or mainly while in candidature for a research degree at this University;
- where any part of this thesis has previously been submitted for a degree or any other qualification at this University or any other institution, this has been clearly stated;
- where I have consulted the published work of others, this is always clearly attributed;
- where I have quoted from the work of others, the source is always given. With the exception of such quotations, this thesis is entirely my own work;
- I have acknowledged all main sources of help;
- where the thesis is based on work done by myself jointly with others, I have made clear exactly what was done by others and what I have contributed myself;
- none of this work has been published before submission

Signed:.....

Date:.....

Acknowledgements

Alhamdulillah, all praise to Allah who guided me at times of light and darkness, and surrounded me with loved ones who were always there to support me. My utmost thanks and appreciation to Dr Srinandan Dasmahapatra, my supervisor and my mentor for insisting on the importance of forming the research questions and to always ask what is the meaning behind everything, guiding this research as it grows organically. I dedicate this thesis especially to my lovely, strong and faithful wife, Wan Nur Syieda Binti Wan Ibrahim, for all the sacrifices, the patience and the endless love . Truly without you I do not know whether I would have ever survive the darkest hour. To my mother, Rahani Binti Hamzah who taught me my first memorable lesson which is to listen, focus and to truly try to understand any lessons and who always believed in me. To my father Kassim Bin Sudin for the everlasting support. To my dear daughter Sara Aisyah, may you someday understand the millions of smiles that you have brought upon Abi and Umi. To my family, siblings, in-laws and those who cheered me along this incredible journey. Many thanks for your endless help and kindness. May Allah reward you and guide us all.

Nomenclature

F_i	Fold change of i
$F[i,j]$	Compared fold change i,j
x	Background concentration
x'	New level of concentration
θ_i	Parameter i
$\boldsymbol{\theta}$	Parameter vector
$\boldsymbol{\theta}^*$	Best estimated parameter vector
$\boldsymbol{\Theta}$	Matrix of parameter
μ	Mean of distribution
σ	Standard deviation of distribution
c_v	Coefficient of variance
$I_p^{x_i,F_j}$	Response to background stimulus x_i with corresponding fold change F_j
$\tilde{I}_p^{\,x_i,F_j}$	Mean of distribution of responses $I_p^{x_i,F_j}$
σ_{x_i,F_j}	Standard deviation of distribution of responses $I_p^{x_i,F_j}$
$< I_p^{F_j} >$	Mean of distribution of responses independent of background
$s_{F_j} >$	Standard deviation of distribution of responses independent of background
$A_{x_0}^{F[i,j]}$	Overlapped area between fold i,j with background x_0
$\mathbf{A}$	Matrix of overlapped areas with element $A_{x_0}^{F[i,j]}$
$\mathbf{J}$	Jacobian matrix
k_d	Dissociation rate constant
$\mathcal{N}(\mu,\sigma^2)$	Normal distribution with mean μ and variance σ^2
$P(F)$	Prior probability of fold change F
$P(I_p)$	Marginalized response I_p
$P(I_p\|F)$	Likelihood of response I_p given fold change F
$P(F\|I_p)$	Posterior probability of fold change F given response I_p

Chapter 1

Introduction

1.1 Motivation

Biological systems respond dynamically to changes in their surrounding environment. For example, cells can sense molecular stimuli using transmembrane protein based receptors and respond via signalling pathways by transcribing genes, synthesizing enzymes or by changing their shapes for motility. Fascinatingly, the complex sense-response behaviour observed are often executed with only a handful of chemical species and without the need of a central nervous system (CNS) (Nakagaki, 2001). Moreover the sensing process takes place is an environment surrounded by elements of uncertainty such as the fluctuating levels of proteins since gene expression is a stochastic process. Hence, the key question of *'How exactly do biological systems and biological cells in particular execute these complex functions under such environments?'* has been a subject studied by many.

In this thesis, we focus on the sensing of chemoattractant cyclic-adenosine monophsophate (cAMP) molecules by the *Dictyostelium Discoideum* cells (referred hereafter as *Dictyostelium*). In the pioneering experiment conducted by John T. Bonner 70 years ago, it is found that starving *Dictyostelium* cells secreted chemoattractant (cAMP) to which downstream cells responded by aggregating towards the gradient source (Bonner and Savage, 1947; Konijn et al., 1967). The cellular slime mould uses a molecular relay where it both secretes and senses the same intracellular and extracellular cAMP in order to communicate with conspecific cells during the aggregation phase (Dinauer et al., 1980a). The chemoattractant therefore plays a major role in both cell chemotaxis and inter-cell signalling where the survival of the species lies on the ability of individual *Dictyostelium* cells to sense and secrete cAMP molecules.

The key question one then ask is *'How does Dictyostelium execute the complex sense-response of cAMP?'*. Given such importance, a considerable amount of literature (reviewed in chapter 2) has been dedicated to understand the intracellular biochemical reactions of *Dictyostelium* when stimulated with cAMP. Although the complete signalling pathway is yet unclear, it has been shown that changes in cAMP elicits a transient response (Devreotes and Steck, 1979) before returning to pre-stimulus level. This desensitising of cellular response upon prolonged stimulation is a feature called 'adaptation' (Dinauer et al., 1980b,c). Adaptation itself is a common property to a wide range of sensory systems (Koshland, 1974; Sterling and Laughlin, 2015) involving biochemical and ionic processes.

A more recent experiment has dissected the biochemical signalling network responsible for cAMP response at specific nodes of the network by fluorescent reporter constructs in microfluidic chambers where cAMP levels are administered in steps of concentration changes. The transient response to changes in cAMP is observed in the activation levels of the Ras protein (RasGTP) (Takeda et al., 2012) before adaptation sets in. It has also been shown that the molecular agents responsible for chemotaxis (through polarization and formation of pseudopods) and secretion of intracellular cAMP lies downstream of this protein's activation. Therefore understanding the features observed in the upstream process might be a key to understanding how cell chemotaxis and cAMP signalling is regulated.

FCD in *Dictyostelium*

However, adaptation is not a feature observed in isolation. A further quantification of the amplitude of the transient RasGTP has been described as characteristic of fold-change detection (FCD) (Takeda et al., 2012; Adler et al., 2014). We describe here a formal definition of FCD. A response is said to depict FCD if its magnitude depends on the ratio of two successive input signals (Koshland, 1974), not their difference (Goentoro and Kirschner, 2009; Shoval et al., 2010). This is shown in more detail in Fig. 1.1A and Fig 1.1B where (input, output) pairs (x, z) with transient responses due to step changes in the input from x_0 to x_1. When two step inputs $x_0 = 1, x_1 = 10$ and $x_1 = 10, x_2 = 100$ of the same fold change (ratio) $F = x_1/x_0 = x_2/x_1$ but of different absolute values $|x_1 - x_0| \neq |x_2 - x_1|$ are introduced sequentially, a system exhibiting FCD produces identical responses z that only depends on F (Fig. 1.1B) (Shoval et al., 2011). A system without this property reacts to the absolute values of inputs and produces output z where z differs in amplitude, shape or duration for different step inputs (Fig. 1.1A). A system with FCD is where output z is identical for step inputs of the same fold but yields distinct responses for different fold inputs. In both the instances shown in Fig. 1.1 the system shows adaptation to a sustained stimulus. In this thesis the term input-output and stimulus-response is used interchangeably.

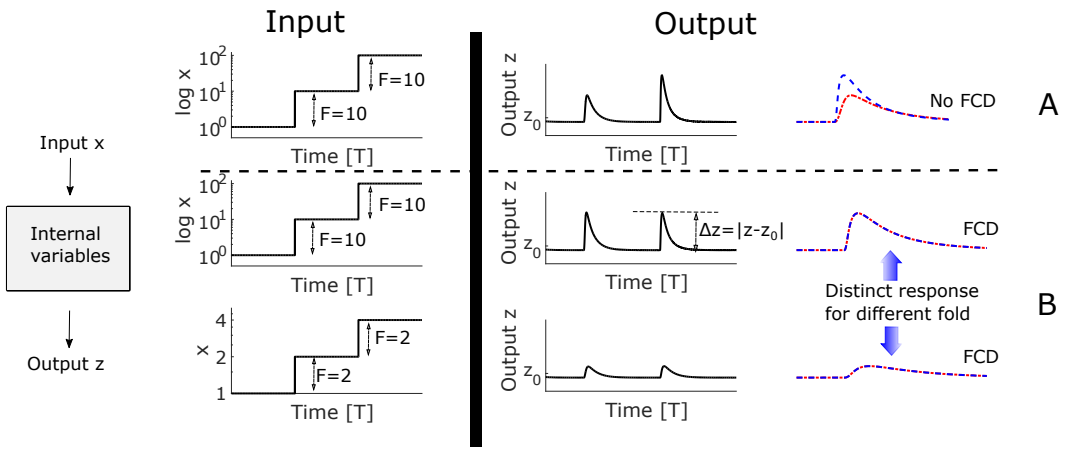

Figure 1.1: Characterization of FCD to show how a system with exact FCD responses to a two step input stimuli. (A) A non-FCD system produces two outputs z which differs in either amplitude, shape or duration. (B) A system with FCD has identical output z for both step inputs which can be clearly seen when the outputs are overlapped.

Network motifs to explain qualitative behaviour in experiments

From the definition we can see that adaptation is a consequence of FCD. The transient activation of RasG, which is the earliest measurable signalling event downstream of G protein activation that eventually leads to chemotaxis and intercellular signalling, has been shown to display FCD. It is thus natural to further ask what role adaptation and FCD play in the sense-response mechanism. Indeed, in answering such a qualitative question, it is not sufficient to only conduct in vitro experiments and map out the network of signalling molecules and package it into a system of ordinary differential equations (ODEs) with each variable representing the proteins in the network, as is done in the field of system biology. A broader objective is to extract the 'design principles' that unify different systems that exhibit the same behaviour (Alon, 2007a). This is made possible due to complex biological networks are often found made of recurring sub networks of a certain motifs (Milo et al., 2002) and is not entirely random. In principle, if it is possible to identify a network motif that exhibits adaptation or FCD behaviour found in *Dictyostelium* , then other organisms which share a similar network motif can possibly exhibit the same behaviour (Kashtan et al., 2004). The FCD property after all is not unique only to *Dictyostelium* cells but is widely reported in other biological systems as well including gene expression in the Wnt signalling pathway (Goentoro and Kirschner, 2009), ERK2 response in cancer cells (Cohen-Saidon et al., 2009) and also in bacterial chemotaxis (Mesibov et al., 1973; Lazova et al., 2011; Masson et al., 2012; Edgington and Tindall, 2014). Other studies have reported on the possibility of FCD in the *Rhodobacther sphaeroides* chemotaxis (Kojadinovic et al., 2013; Hamadeh et al., 2013).

Network motifs for FCD

What are the network motifs suggested for adaptation and FCD ? The design principles of adaptation (Martiel and Goldbeter, 1987) is already an active area of interest across a diverse set of organism and systems(Barkai and Leibler, 1997; Yi et al., 2000; Ma et al., 2009). For FCD, a particular network motif (Alon, 2007b) called the incoherent feed-forward (IFF) loop has been implicated in the FCD response (Goentoro and Kirschner, 2009; Shoval et al., 2010). Features of the IFF architecture – when antagonistic or "paradoxical" influences of activation and inhibition (Hart and Alon, 2013) are provided by a molecular agent – were incorporated in a mathematical model involving proteins in the signalling pathway of the cAMP response in the *Dictyostelium* experiment mentioned earlier (Takeda et al., 2012). Parameters of this system of ordinary differential equations (ODEs) were fit using optimisation methods to a time series of a fluorescent reporter of the transient response(Takeda et al., 2012). It was also shown that among the few common ways of achieving adaptation in biological networks (Ma et al., 2009), this IFF network architecture better explains the data on transient responses (Takeda et al., 2012).

1.2 The problem of sensing accuracy

At this point, we should be able to answer partially the key question of *'How do Dictyostelium cells execute FCD sense-response mechanism ?'* by pointing to the IFF suggested in Takeda et al. (2012) and Goentoro et al. (2009) as the network motif responsible for explaining the role of FCD observed in experiments as done byAdler et al. (2014). However, upon further deliberation we find that there are crucial questions yet to be addressed, which forms the foundation of our research.

In both Takeda et al. (2012) and Kamino et al. (2017), although FCD is reported to be observed in the transient responses of *Dictyostelium* cells to a range of inputs, little is known about the *accuracy* of FCD. How well does single *Dictyostelium* cells senses fold change? Is the sensing of fold change equally accurate for any given fold? Error bars in the experiment by Takeda et al. (2012) and Kamino et al. (2017), indicates that there are different responses to the same step input cAMP due to cell-cell variability. In principle if we want to quantify the accuracy of FCD sensing mechanism at single cells level then we should stimulate single cells of *Dictyostelium* repetitively with the stimulus fold cAMP of interest but with the initial stimulus varied. However, numerous exposure of fluorescent-tag cells to illumination induces phototoxicity and therefore such iteration of measurement is not feasible.

While FCD accuracy derived from mathematical models are commonly investigated using skeletal networks, there is no single studies that focusses on the accuracy of FCD

derived by detailed models such as the model ODEs given by Takeda et al. (2012). To quantify the accuracy of FCD dynamics from models of ODEs, one approach is to evaluate the same model with different set of parameters as done by Goentoro et al. (2009) with the skeletal three node IFF network motif. In this setting, the cell-cell variability is emulated through the different sets of parameter values. A model that can exhibit FCD dynamics across a wide range of parameter values is then deemed to be more useful than one that can only exhibit FCD within a narrow range. To our best knowledge, the model ODEs with IFF structure suggested by Takeda et al. (2012) represents the most intricate and therefore the best known model to describe the molecular actors that govern the upstream dynamics of *Dictyostelium* cells in response to step input of chemoattractant cyclic AMP. It is important to note however, that the model was structured with the intention of characterizing the adaptation behaviour of *Dictyostelium* cells and not of FCD. The notion that the same model in the same experiment exhibit FCD was put forth by Adler et al. (2014). What then is the range of parameter values that the model ODEs exhibit FCD?

Understanding the accuracy of FCD may potentially assist cell biologists in designing future experiments where stimulation of cells can be focussed within a biologically realistic range. But more importantly this study offers some important insights into how the cell's decision making: -to initiate motility or to secrete intracellular cAMP- is regulated and constrained by the modelled upstream sensing mechanism. We argue that if the fate of the species lies in the ability of *Dictyostelium* cells to sense cAMP molecules, then cells must be able to interpret the fold change in extracellular cAMP concentration as accurately as possible, and collectively execute the swimming aggregation dynamics observed by Bonner and Savage (1947).

1.3 Biophysical laws governing sensory systems

In the studies of design principles of FCD, researchers not only analyse network circuits that enable FCD, but also relate the FCD property with biophysical laws found in well studied sensory system such as vision and hearing of humans. For example, Goentoro et al. (2009) suggested that FCD is a modified version of the Weber's law where the minimally noticeable difference between two stimulus is proportional to the level of the background stimulus compared. Adler et al. (2014) suggested that the stimulus-response relation of the *Dictyostelium* experiment by Takeda et al. (2012) obeys the Weber-Fechner's logarithmic law where the magnitude of responses increase logarithmically. The definition of both laws and the findings of the two studies are further elaborated in chapter 2. It is important to note that the biophysical laws described stemmed from the field of psychology and cognitive neuroscience. Therefore the laws are used to explain sensory behaviour of organisms with central nervous systems. On the other hand, the models studied for FCD are relatively simple and mainly consist of 3 to 4

nodes. Moreover as reviewed in Ferrell (2009), FCD is found in cell signalling process where any notion of a cognitive system is non-existent. However, by associating FCD to biophysical laws, one may be provide an explanation to why a property such as FCD is desirable in lower level signalling systems.

In this thesis we are inspired by the idea that there exists a unifying theme for cellular level signalling networks as what we have seen in complex sensory systems. Since a *Dictyostelium* cell is a sensory system, are there other physical laws that it shares with more complex sensory systems? Can we draw concepts from the field of neuroscience as what Adler et al. (2014) and Goentoro et al. (2009) had done and analyse the sense-response mechanism of *Dictyostelium* cells in the same way researches investigate the responses of cognitive systems? By answering these questions and by viewing cells as computational modules, we hope that we can further the discussion to how single cell organisms such as the *Dictyostelium* process or compute extracellular information.

1.4 Thesis approach and contributions

To address the issues underlined in section 1.2 and 1.3, we evaluate the accuracy of FCD sense-response mechanism in *Dictyostelium* , not through experiments but by examining variability in behavioural outcomes in the context of variability in model parameters that are compatible with the observations in Takeda et al. (2012) and assess the relevance of the input-output characterisation of the sensing module in shaping the autonomous actuating responses. We explicitly state here that the model ODEs as characterized by Takeda et al. (2012) is the core model which we based our research upon. As we are exploring constraints on mathematical models, we acknowledge inadequacies such as the complexity of assigning pertinent values for certain model parameters, limitations by model structures and the deterministic nature of the model.

The contributions of this thesis are briefly summarised as below,

- We present a characterization of the accuracy of FCD using an intermediate sensory representation as derived from the model ODEs of Takeda et al. (2012) when stimulated with a wide range of fold stimulus. We demonstrate an approach which enables us to generalise the quantification of the FCD accuracy to a wider range of stimulus and background cAMP. We propose a hyperbolic equation to describe the stimulus-response relation and the logarithmic encoding hypothesis to describe the underlying distribution of responses.
- We characterize the posterior probability of detecting fold changes using a Bayesian approach and introduce a novel model for prior probability of fold changes in concentration based on empirical data. We introduce the FCD sense-response mechanism in the context of a Bayesian observer to characterize its perception and

evaluate its biases. We present a novel model for characterizing the uncertainties in the extracellular fold changes.

1.5 Thesis structure

This thesis is organized as below,

- Chapter 2, **Fold Change Detection (FCD) in the signalling pathway of *Dictyostelium* cells: Experiments and models**- We present a review of biological experiments responsible for uncovering the cyclic-AMP sensing mechanism in *Dictyostelium* cells and for identifying the molecular proteins involved in the signalling pathway. We also introduce fundamental models and their properties used to explain the adaptation and FCD behaviours in biological systems. More importantly we present in detail the experiment and modelling results by Takeda et al. (2012) as this is the starting point of our research.

- Chapter 3, **Model analysis and parameter estimation**- We begin expanding our understanding of FCD in *Dictyostelium* by analysing the model ODEs of Takeda et al. (2012) which this thesis is built upon. We explore the dynamical features of the model in the context of steady states and stability analysis in enabling the FCD mechanism. But more importantly in this chapter we estimate parameters of the model ODEs using a Bayesian method to emulate heterogeneity properties as seen in experiments of Takeda et al. (2012). We analyse the resulting posterior densities of parameters and derive insights to how different parameters influences the detection of fold.

- Chapter 4, **The accuracy of Fold Change Detection**- In this chapter we present our main contribution in the characterization of the accuracy of FCD by means of log-normal approximation to the density of responses generated from the estimated parameters in chapter 3. We further generalise the quantification of FCD accuracy by estimating coefficients to quadratic functions that is used to define the parameters of the log-normal approximation itself. We also characterize the *fold distinguishability* property.

  In this chapter we also revisit the biophysical laws suggested for governing FCD in *Dictyostelium* cells. Specifically we probe whether it is possible to observe the Weber-Fechner's law using the model by Takeda et al. (2012). We also ask whether there are other laws that better describe the stimulus-responses relation.

- Chapter 5, **Inferring the posterior probability of fold change**- To characterize the accuracy of FCD as derived from the model ODEs of Takeda et al. (2012) in a Bayesian approach, we infer the posterior probability of fold change given

response by using densities of responses as derived in chapter 4. We present a novel prior modelled from an experiment of *Dictyostelium* chemotaxis in order to compute the posterior and compare with priors chosen from known families of distributions. We also analyse the influence of background cAMP to each Bayesian components.

- Chapter 6, **Relation with the external world**- In this chapter we view the *Dictyostelium* cells in the context of a Bayesian Observer model. We characterize a novel model of the extracellular fold change and the population cells' perception of fold change. We evaluate in detail the perception's accuracy by computing its divergence from the model of extracellular fold change. We also characterize and evaluate perceptual bias and distinguishability threshold of the Observer model and examine the relation between these two measures of perception.

- Chapter 7, **Conclusions**- Finally, we summarize our work in this chapter and highlight significant questions for future work.

Chapter 2

Fold Change Detection (FCD) in *Dictyostelium* cells: Experiments and models

2.1 Introduction

This chapter presents the biological and mathematical knowledge required in order to understand how fold change behaviour is observed in *Dictyostelium* cells and how the dynamics of the behaviour is modelled. We start by describing the life cycle of *Dictyostelium* cells and its main phases followed by the description of the signalling pathway where FCD is observed. This is followed by a detail explanation of the core experiment by Takeda et al. (2012) said to successfully capture the FCD behaviour of *Dictyostelium* cells. We then introduce the concept of network motifs and describe several networks that are said to exhibit FCD. We describe how the protein interactions in the *Dictyostelium* chemotaxis signalling pathway can be viewed as a network and introduce the incoherent feedforward network as proposed by Takeda et al. (2012). Most importantly, we introduce the model ODEs used by Takeda et al. (2012) to describe the dynamics of the incoherent feedforward network that is said as the best model that captures the experimental data. This model ODEs by Takeda et al. (2012) is the core model that we based our research upon.

2.2 Life cycle of *Dictyostelium* cells

In this section we will explain one of the three life cycles of *Dictyostelium* cells, highlighting only the main stages of the cycle and ignoring most of the molecular biology details. The objective is not only to provide an overview of the *Dictyostelium* cell's

development but also to understand at which stage FCD is observed and appreciate the consequences if *Dictyostelium* cells were unable to carry out FCD. We illustrated the life cycle of *Dictyostelium* cells in Figure 2.1.

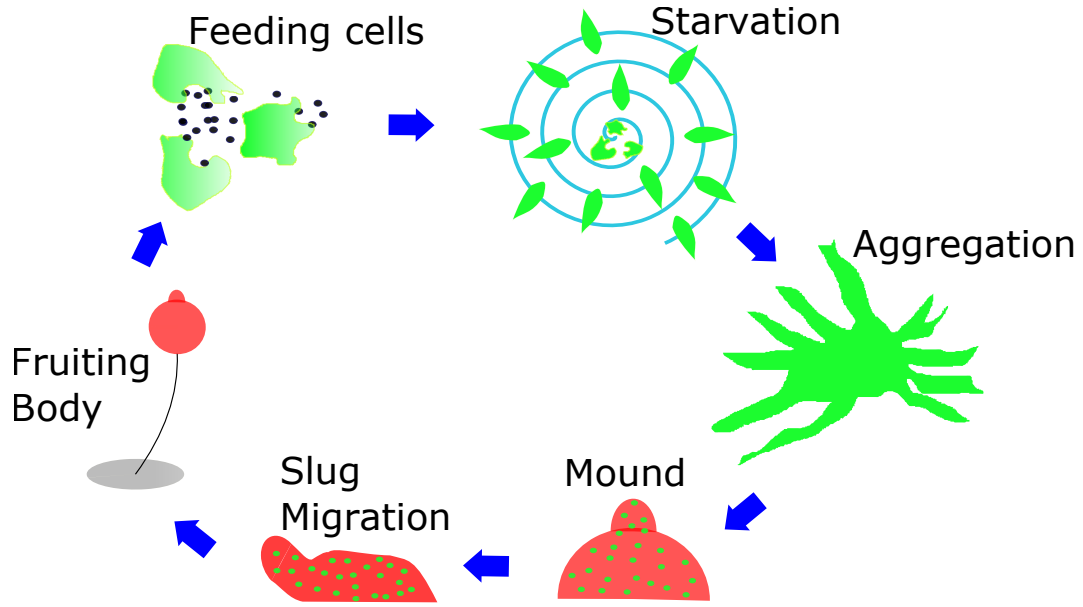

Figure 2.1: Life cycle of *Dictyostelium Discoideum* . Cells are indicated in green and black dots represent bacteria. Propagation of wave cAMP is indicated by the blue spiral. FCD occurs in the starvation and aggregation stages. Refer text for more details.

The *Dictyostelium Discoideum* species was first discovered by Kenneth Raper (Burris and Newcomb, 1991; Raper, 1935) nearly 83 years ago in the Appalachhian Mountains of North America. In the early stages, *Dictyostelium* cells behave independently and engulf surrounding bacteria. However, the continuous engulfing of bacteria and the increase in the number of cells due to cell-division leads to depletion of food. The cells are aware of this event as they have been tracking the ratio of cell density to food source by secreting prestarvation factor (PSF) (Clarke et al., 1988). As cells enter the starvation phase, one part of the population begin to secrete cyclic AMP in pulses (Konijn et al., 1967). The propagated wave of cAMP is then sensed by downstream cells and cells aggregate towards the gradient source while at the same time secreting cAMP molecules (Raper, 1935; Bonner and Savage, 1947). The aggregated cells then form a mound. Cells underneath the mound then push the mound upwards (Siegert and Weijer, 1995) causing the growing mound to topple, forming a slug consisting cells in the range of a few hundred to a hundred thousand. The slug then migrates for up to two weeks and then forms a fruiting structure consisting of stalk and spore cells (Raper, 1940). The stalk and spore cells are found at the anterior and the posterior of the fruiting body respectively.

It is important to note that it is during both starvation and aggregation stages that *Dictyostelium* cells are most likely to carry out FCD as experiments have shown that FCD

is found in intracellular responses of *Dictyostelium* cells when sensing cAMP gradients (Takeda et al., 2012; Kamino et al., 2017). FCD has been suggested as a mechanism that guides the chemotaxis of cells and therefore the absence of FCD implies the inability of cells to move towards the aggregation centre.

2.3 The signalling pathway of *Dictyostelium*

From the life cycle of *Dictyostelium* cells, we understand that FCD in *Dictyostelium* cells most likely occur during the starvation and aggregation stages as sensing fold change in cAMP gradient during these stages guide the chemotaxis of cells towards the aggregation centre. Here we will zoom in the signalling pathways regulating chemotaxis of *Dictyostelium* cells. In doing so we will also identify the pathway responsible for secretion of cAMP. As FCD is observed in the transient response of RasGTP protein (Takeda et al., 2012), the goal here is to understand the location of RasGTP in the signalling pathway and the implications of not having FCD to the pathway.

There are many models proposed to explain the signalling pathway of *Dictyostelium* cells for chemotaxis as biologists continue to pinpoint the molecular agents involved and fully understand their interactions. Examples are the model proposed by Kortholt et al. (2011) or the model described by Kölsch et al. (2008). We illustrated the signalling pathways for both chemotaxis and self secretion of cAMP by *Dictyostelium* cells in Figure 2.2. Figure 2.2 represents our approximation of the signalling pathway in the context of FCD through survey of literatures and does not in any way represents a complete or definitive form of the chemotaxis signalling pathway.

When chemoattractant cAMP molecules bind to the surface receptors cAR1 of the *Dictyostelium* cell during the starvation and aggregation stages, it initialize the intracellular signalling system through the dissociation of the receptor-coupled heterotrimeric G proteins (Klein et al., 1985; Sun and Devreotes, 1991). The signal from the G proteins is then transduced downstream to RasGEFs (guanine nucleotide exchange factors) which then activate Ras proteins by causing RasG bound guanosine diphosphate-RasGDP proteins to bind to guanosine triphosphate(GTP), creating the activated Ras-GTP proteins (Kae et al., 2007). RasGTP proteins are shown to regulate downstream signalling molecules of PI3K- which in turn translocate phosphatidylinositol-(3,4,5)-triphosphate (PIP3) to the plasma membrane (Sasaki et al., 2004). PIP3 then allows the binding of pleckstrin homology (PH) domain which contains proteins such as cytosolic regulator of adenylyl cyclase (CRAC) and protein kinase B (Parent et al., 1998; Meili et al., 1999). Proteins contained in the PH domain are key candidates suggested for activation of actin polymerization crucial for the formation of pseudopods (Iijima and Devreotes, 2002). A pseudopod is an extension of the cell's leading edge, enabling chemotaxis of the cell. Meanwhile, CRAC also has been found to be an important element for the activation of

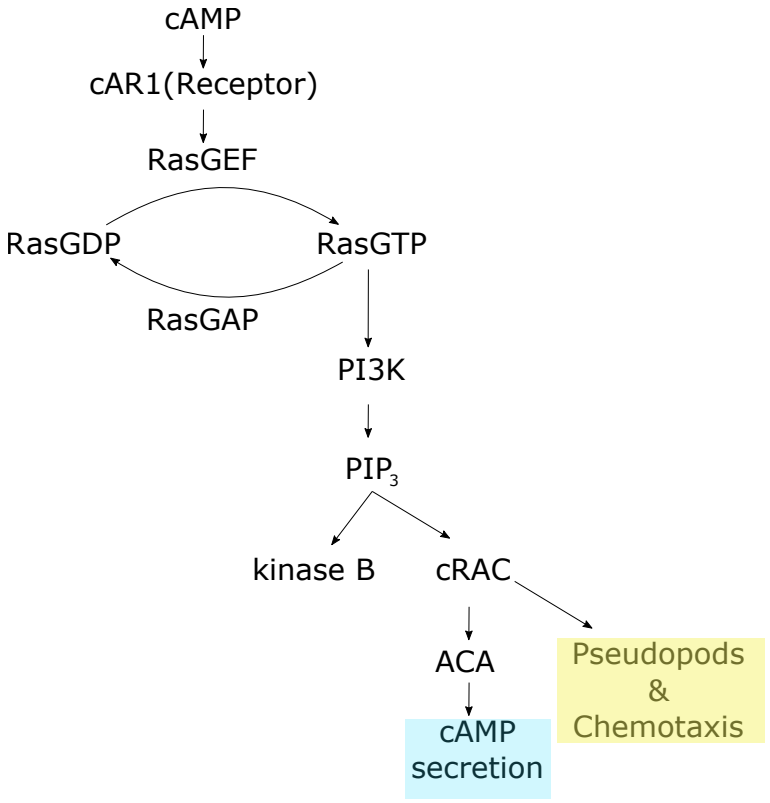

Figure 2.2: Approximation of *Dictyostelium* cell's signalling pathway for chemotaxis and cAMP secretion.

ACA (Comer et al., 2005; Comer and Parent, 2006) which leads to secretion of cAMP molecules(Saran et al., 2002).

Hence, the activation of PI3K signalling pathway by Ras protein -triggered when cAMP molecules bind to surface receptors- not only causes chemotaxis but also the secretion of cAMP by the cell. Due to Ras protein is the single upstream effector regulating both downstream pathways, FCD observed in transient responses of Ras-GTP (Takeda et al., 2012) is believed to play a significant role in determining chemotaxis and self secretion of cAMP.

2.4 FCD observed in the experiment by Takeda et al. (2012)

From the chemotaxis signalling pathway of *Dictyostelium* as shown in Figure 2.2, we know that RasGTP protein is crucial in mediating signals for both chemotaxis and internal cAMP secretion. We present here the experiment by Takeda et al. (2012) which provides evidences supporting the claim that *Dictyostelium* cells respond to fold changes in concentration and not of the absolute level of cAMP through studying the changes in RasGTP protein. It is interesting to note that the experiment by Takeda et al. (2012) was not designed for the observation of FCD but of adaptation behaviour. The existence

of FCD property in the experiment by Takeda et al. (2012) was pointed out by Adler et al. (2014) and has been confirmed later in the experiment by Kamino et al. (2017).

2.4.1 Experiment methods and results

In the experiment by Takeda et al. (2012), *Dictyostelium* cells were placed in a microfluidic device and stimulated with a sudden increase in concentration of cAMP, simulating a step change in input. The step input is illustrated in Figure 2.3A. One might ask whether the step input is a realistic representation of the changes in concentration for when the wave of cAMP passes through stationary *Dictyostelium* cells. The scheme of cAMP wave proposed by Tomchik and Devreotes (1981) by looking at distribution of cAMP waves captured in fluorographs may provide a hint to the answer. In the scheme, the minimum time it takes for the concentration in the cAMP wave to change from 10nM to 1μM is said to be half a minute given that the wave travels at the velocity of 300μm/min. Therefore, a step input from 10nM to 1μM is not biologically realistic. However, as shown in experiments of Takeda et al. (2012); Kamino et al. (2017) and also Sgro et al. (2015), step inputs are commonly applied by biologists in the study of cell's response to stimulus.

The responses of *Dictyostelium* cells in the microfluidic device to step input cAMP are monitored not by studying the chemotaxis behaviour of cells but by recording the level of brightness of the RBD-green fluoroscent protein(GFP) (referred hereafter as RBD). RBD acts as a reporter for the RasGTP protein of the cells. Hence, in the experiment by Takeda et al. (2012), changes in RasGTP protein of *Dictyostelium* cells is the quantity of interest.

We describe the experiment by Takeda et al. (2012) and the changes in protein of the signalling pathway which can be easier understood by referring to Figure 2.2. As shown in Figure 2.3, before time t_0, cAMP concentration in the microfluidic device is at a basal level x and RasGDP - the non activated state of RasGTP- is distributed uniformly across the cell. When the concentration increases rapidly to x' in a step like manner at t_0, the activated RasG protein- RasGTP, translocate to the leading edge of the cell's membrane. RBD fluorescent reporter protein then binds to RasGTP at the cell's membrane and consequently the intensity or the brightness of certain cytosol region decreases as illustrated in Figure 2.3B and Figure 2.3C. The intensity of RBD fluorescent protein $I(t)$ then gradually returns to its pre-stimulus level of z_0 even in the continuous presence of new cAMP level x', indicating adaptation.

The magnitude of the peak response I_p and the time to reach to the peak T_p were then measured and recorded. Unfortunately there is no data on the adaptation time T_{adapt} in the experiment by Takeda et al. (2012), although the central theme of the study is the adaptation behaviour of RasGTP. The experiment results for responses to various step

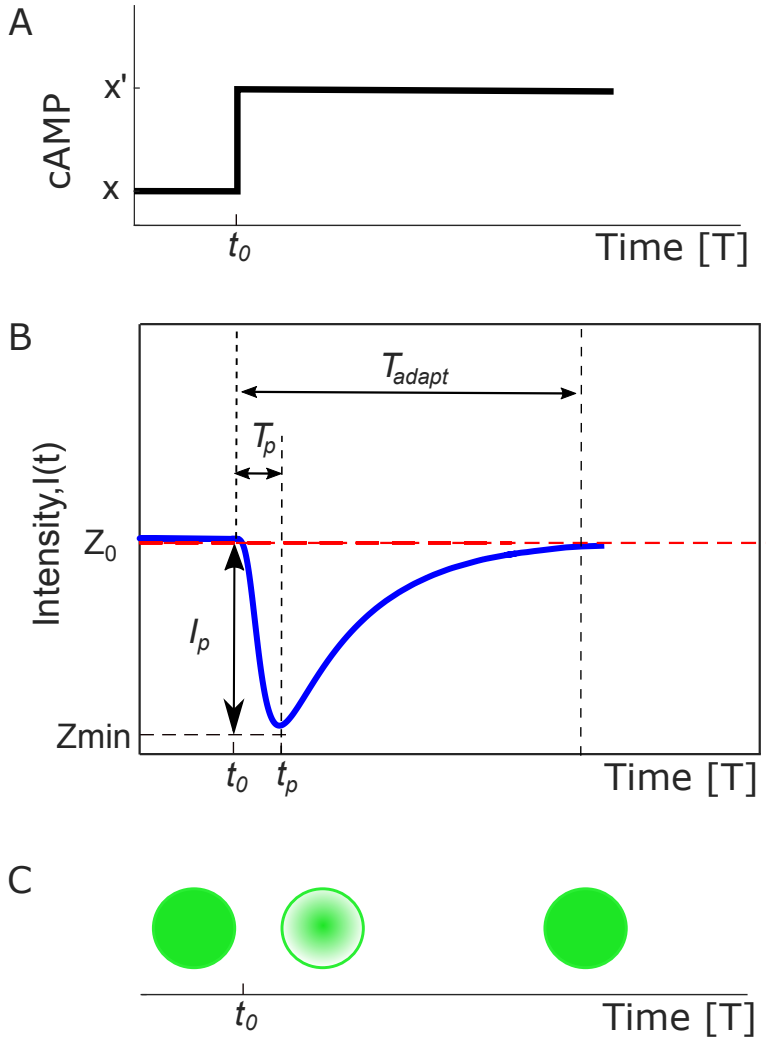

Figure 2.3: Illustration of the *Dictyostelium* cells response to stimulus cAMP experiment by Takeda et al. (2012). (A) cAMP inputs were introduced in a step like manner where x is the basal level and x' is the newly increased level of cAMP at time t_0. (B) Response of RasGTP protein measured by the intensity of RBD fluorescent reporter protein. The intensity rapidly decreases when a new level of cAMP x' is introduced and reaches minimum at z_{min}, followed by a gradual return to its basal level z_0. The magnitude of the peak response $I_p = z_{min} - z_0$ and time to reach it $T_p = t_p - t_0$ were measured and recorded. I_p and T_p values varies with background x (shown later in Figure 2.4). The average time for T_{adapt} is $\approx$ 50s (Takeda et al., 2012). (C) Changes in cell intensity as new level of cAMP is introduced where the intensity is concentrated at the cell's membrane as RBD binds to RasGTP.

inputs are reproduced as Figure 2.4A for I_p and Figure 2.4B for T_p. I_p responses are normalized by responses of x = 0nM, x' = 1000nM. From Figure 2.4, it is interesting to note that I_p responses of *Dictyostelium* cells were also measured for step inputs with basal level $x = 0$ and therefore represents undefined fold changes in input concentration.

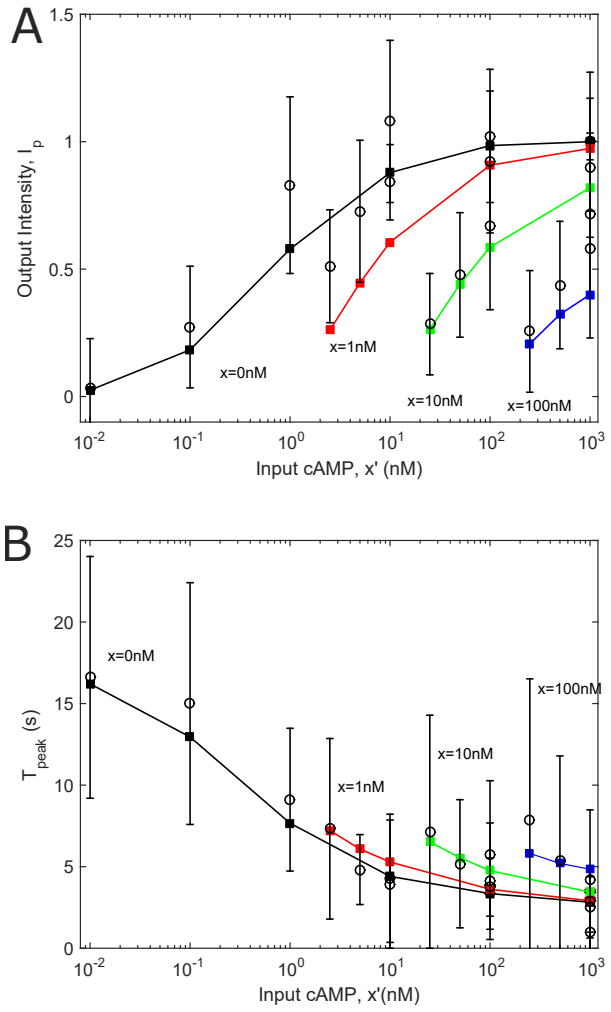

Figure 2.4: Figure 2C and Figure 2D experiment results by Takeda et al. (2012) reproduced. Black circles indicate average responses and error bars represent standard deviation. Squares indicate outputs generated from parameters derived by Takeda et al. (2012) and solid lines are the corresponding interpolations discussed in section 2.5.3. x is the initial stimulus and x' is the new level of cAMP. Data for each background cAMP is colour coded where Black:$x = 0$nM, Red:$x = 1$nM, Green:$x = 10$nM, Blue:$x = 100$nM. (A) I_p responses. (B) T_p responses.

2.4.2 Weber-Fechner's Logarithmic law

However, FCD is not obvious from the measured I_p in Figure 2.4A. Therefore we selected I_p responses to step inputs of nonzero basal level ($x \neq 0$) and replotted as a function of fold change $F = x'/x$ in Figure 2.5. As can be seen, although the responses overlap each other, different fold input does have a different range of I_p thus displaying 'FCD-like response' (Adler et al., 2014). 'FCD-like response' in the sense that stimulation with the same background concentration but with different fold input leads to different outputs. If the responses follow exact FCD, then we would expect that responses for the same fold input is identical regardless of background cAMP and therefore the error bars would

disappear and there would be only one data point for each fold inputs. The responses between different fold input must remain distinct although there is no requirement that the relation between fold input and output to be linear.

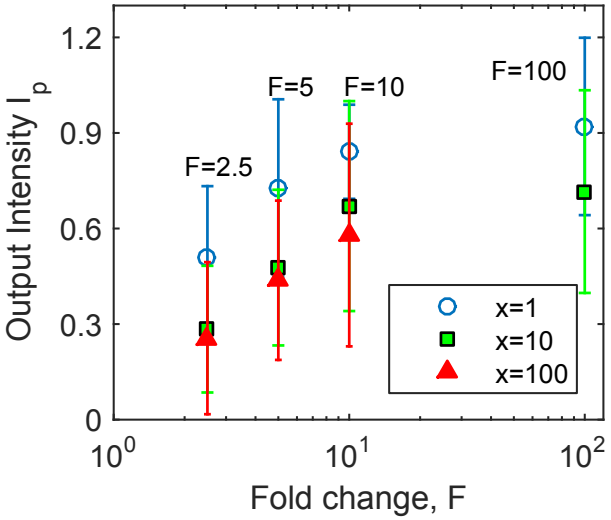

Figure 2.5: I_p measurements by Takeda et al. (2012) of Figure 2.4A replotted as a function of fold change.

The FCD response as observed in Figure 2.5 is said to be a manifestation of Weber's law (Goentoro et al., 2009). We briefly describe Weber's law and its derivative, the Fechner logarithmic law and its relation to FCD. Weber's law was established from experiments conducted by Ernst Heinrich Weber in the 19th century to explain the relation between stimulus and responses in human sensory system such as vision and is often expressed as

$$\frac{\Delta S}{S_1} = k \tag{2.1}$$

where k is a constant, S_1 is the initial stimulus and ΔS is the just noticeable difference. Weber's law stated that when comparing two stimulus S_1 and S_2 where $S_2 > S_1$, the 'just noticeable difference' between two stimulus $\Delta S = S_2 - S_1$ is proportional to the inital stimulus of S_1. Therefore, as the compared background stimulus increases, S_2 needs to be proportionally larger than S_1 in order to be distinguishable. From equation 2.1, the relation between responses R to stimulus S is said to follow a logarithmic function of

$$R = k \ln S \tag{2.2}$$

where responses R represents the perceived stimulus. Equation 2.2 is the Fechner logarithmic law and is shown in Figure 2.6. If FCD observed in Figure 2.5 is to obey Weber's law, responses I_p must increases proportionally to increased stimulus fold in order to sustain distinguishability of stimulus. The relation between I_p and stimulus

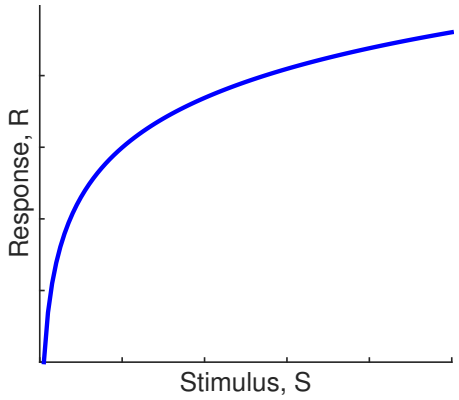

Figure 2.6: Weber-Fechner's logarithmic law with Weber's constant $k = 1$.

fold F is then also logarithmic. This logarithmic relation has been suggested by Adler et al. (2014) as best describes the relation between fold change (input) and RBD fluorescent protein intensity (output). However, the stimulus S in Weber-Fechner's law is of absolute magnitude while fold change F is a ratio of two stimulus. Therefore the logarithmic law suggested for Figure 2.5 is a modified version of the Weber-Fechner's law.

2.5 FCD network motifs

The interactions between different proteins as mapped out in signalling pathway of Figure 2.2 and described in the experiment by Takeda et al. (2012) can be viewed in the context of network motifs. In this section, we will introduce the concept of network motifs followed by which network motifs are said to exhibit FCD. We will then explain which category of motif does the protein network in the experiment by Takeda et al. (2012) belongs to.

2.5.1 Definition and examples of network motifs

A network can be described as a directed graph with nodes. In a biological network, nodes represent biochemical elements such as proteins or genes and directed edges represent their interactions. For example, a two node network of $X \rightarrow Y$ can be used to represent transcription factor X activating gene Y. In this example X is an activator for Y. X can also be an inhibitor by suppressing the expression of gene Y, indicated by $X \dashv Y$. FCD and adaptation behaviour in biological systems are mainly investigated using simplified three nodes networks. A recent study of ~500,000 three nodes network motifs found that only several hundreds of them exhibit FCD (Adler et al., 2017). The main and most commonly studied networks for FCD are the incoherent feedforward, the non-linear integral feedback and the log-differential network (Shoval et al., 2010;

Hironaka and Morishita, 2014). The networks are shown in Figure 2.7 where X is the input node, Y is the internal variable node and Z is the output node. Input node X activates both Y and Z.

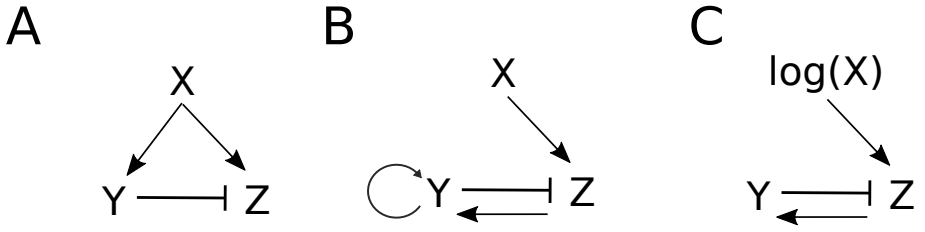

Figure 2.7: Network motifs that are found to exhibit FCD. X is the input Y is the internal variable and Z indicates the system's output. (A) Incoherent feedforward loop type 1 (IFFL-1). (B) Non-linear integral feedback loop. (C) Logarithmic input with linear feedback.

Assigning a different combination of functions to nodes results in a different type of incoherent feedforward network. It has been mathematically proven that the incoherent feedforward loop type 1 (IFFL-1) can exhibit exact FCD when Y strongly represses the production of Z (Goentoro et al., 2009). In such condition, the dynamics of IFFL-1 can be described by a set of two ODEs as

$$\frac{dY}{dt} = k_1 X - k_{-1} Y \tag{2.3}$$

$$\frac{dZ}{dt} = \frac{k_2 X}{Y} - k_{-2} Z \tag{2.4}$$

where k_1, k_2 and k_{-1}, k_{-2} are the activation and degradation rates of node Y and Z respectively. As can be seen in equation 2.4, Z is dependent only on the fold change in input X and not on the absolute level (Goentoro et al., 2009) due to Y itself is a function of X.

2.5.2 Modelling experiment results of Takeda et al. (2012): Incoherent feedforward network

In the experiment by Takeda et al. (2012), only the changes of RasGTP protein were measured through its RBD reporter protein. Therefore, we do not know the changes occurring in other proteins in the signalling pathway such as the RasGEF, or receptor R as mapped out in Figure 2.2. As such, Takeda et al. (2012) proposed an incoherent feedforward network model shown in Figure 2.8A to describe the experimental results.

If we compare Figure 2.8A to the signalling pathway of Figure 2.2, we can see that the network proposed by Takeda et al. (2012) characterizes the dynamics of proteins upstream of PI3K. The deactivation of RasGTP to RasGDP is mediated by RasGAP

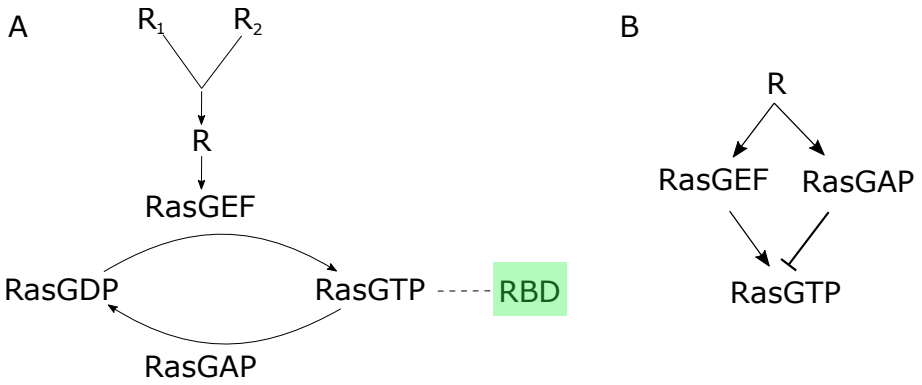

Figure 2.8: Network Motifs. (A) Network of protein variables as derived from the model ODEs (equation 2.8 to equation 2.14). (B) Network in Figure 2.8A simplified as an incoherent feedforward network.

and therefore RasGAP is considered as an inhibitor. On the other hand, RasGEF is responsible for binding RasGDP to GTP and therefore is considered an activator. Figure 2.8A therefore effectively functions as a incoherent feedforward network as illustrated in Figure 2.8B.

A variation of the incoherent feedforward network: The Sniffer model

In comparison with the simple motifs of Figure 2.7A,the incoherent feedforward network shown in Figure 2.8B seems to has four nodes but effectively functions as a three node network where receptor R can be considered as input node X activating GEF as Y and output RasGTP as Z. The activation of RasGTP by R is made through GEF. The incoherent feedforward network shown in Figure 2.7A is of type 1 where inhibition of Z is by Y.

However, the dynamics of the incoherent feedforward network in Figure 2.8B differs slightly where inhibitor GAP accelerates the degradation of output RasGTP instead of suppressing the production of RasGTP. Therefore the dynamics of such incoherent feedforward network is modelled as

$$\frac{dY}{dt} = k_1 X - k_{-1} Y \tag{2.5}$$

$$\frac{dZ}{dt} = k_2 X - k_{-2} Y Z \tag{2.6}$$

where the second term on the right hand side of equation 2.6 represents degradation of output Z. From equation 2.6 we can see that the dependency on X by Z is not being cancelled out and therefore no FCD. Such variation of the incoherent feedforward network is called a 'sniffer' (Tyson et al., 2003; Ma et al., 2009). The sniffer model is

shown to exhibit FCD only in a limited region when the dynamics of Z is significantly faster than Y (Goentoro et al., 2009) causing Z to be in a quasi steady-state Z_{ss}

$$Z_{\text{ss}} = \frac{k_2 X}{k_{-2} Y} \tag{2.7}$$

The independence of RasGTP in Figure 2.8B from its input cAMP via the R protein variable is further discussed in chapter 3.

2.5.3 Model ODEs of the incoherent feedforward network

The dynamics of the incoherent feedforward model suggested in Figure 2.8A is described by Takeda et al. (2012) through a set of Ordinary Differential Equations (ODEs) as

$$\begin{aligned}
\frac{dR_1}{dt} &= k_{R1}(cAMP + r_1)(R_1^{tot} - R_1) - k_{-R1}R_1 && (2.8)\\
\frac{dR_2}{dt} &= k_{R2}(cAMP + r_2)(R_2^{tot} - R_2) - k_{-R2}R_2 && (2.9)\\
R &= R_1 + R_2 && (2.10)\\
\frac{dGEF}{dt} &= k_{GEF}R - k_{-GEF}GEF && (2.11)\\
\frac{dGAP}{dt} &= k_{GAP}R - k_{-GAP}GAP && (2.12)\\
\frac{dRas^{GTP}}{dt} &= k_{Ras}GEF(Ras^{tot} - Ras^{GTP}) - k_{-Ras}GAPRas^{GTP} && (2.13)\\
\frac{dRBD^{cyt}}{dt} &= k^{off}_{RBD}(RBD^{tot} - RBD^{cyt}) - k^{on}_{RBD}Ras^{GTP}RBD^{cyt} && (2.14)
\end{aligned}$$

where k_x and k_{-x} are the activation and degradation constant for protein x of interest. We explicitly state here that the model ODEs of equation 2.8 to equation 2.10 forms the core model which we based our analysis upon.

We explain the meaning of each equation in the model above as below,

- In equation 2.8,2.9 and 2.10, the surface receptors cAR1(Figure 2.2) is denoted as R and is a sum result of two receptor populations of different affinity R_1 and R_2. The level of affinity is set through the dissociation constants of $K_d = k_{-Ri}/k_{Ri}$ where k_{-Ri} and k_{Ri} is the binding and unbinding kinetic rates respectively for receptor population R_i.
- r_1 and r_2 is the constitutive activation of receptor R_1 and R_2 respectively to indicate the minimum level of activation when the surrounding cAMP concentration is zero.

- The dynamics of RasGEF and RasGAP proteins are regulated by R and represented by equation 2.11 and equation 2.12, where RasGEF is denoted as GEF and RasGAP is denoted as GAP.
- Equation 2.13 represents the main protein of interest- RasGTP where Ras^{tot} denotes the total concentration of Ras.
- Equation 2.14 describes the dynamics of the RBD fluorescent reporter protein where RBD^{tot} denotes the total concentration of RBD.

Takeda et al. (2012) also introduced another model of ODEs structured as an integral feedback network in order to describe the observed behaviour in Figure 2.4A and Figure 2.4B. Model ODEs of both incoherent feedforward network and integral feedback network were fitted were fitted to the experimental results in Figure 2.4A and Figure 2.4B and their model parameters estimated using an optimisation method called simulated annealing. The result of solving the incoherent feedforward network model ODEs with the estimated paramer is shown in Figure 2.4 as squares with solid lines its corresponding linear interpolation. We refer the reader to the supplemental data provided by Takeda et al. (2012) for details of the optimisation data. Our focus here is only on the incoherent feed forward model as it is the only model that is able to produce compatible fitting results.

In order to understand the dynamics of each protein variable of the incoherent feedforward network, we numerically simulated the model ODEs of equation 2.8 to equation 2.14 and showed the result in Figure 2.9. The parameters and input cAMP values are described in detail in the caption of Figure 2.9. As can be seen in Figure 2.9A, each receptor populations reaches its steady states at a different rate due to the difference in affinity. Having two receptor populations is important as Takeda et al. (2012) reported that if the incoherent feedforward model ODEs has only one receptor population, it does not yield desirable fitting results. We have also confirmed this report when attempting to fit the model ODEs ourselves using a Bayesian method in chapter 3 similar to the optimisation method implemented by Takeda et al. (2012). However, the confirmed result is not presented in this thesis as it is irrelevant to our objectives. It is not yet clear how the delay between R_1 and R_2 observed in Figure 2.9A contributes to the increase in fitting accuracy and describing FCD observed. However the inclusion of two receptor populations is done in order to create a realistic model as it has been reported that *Dictyostelium* cell's receptors are made up of multiple populations with different cAMP binding rates (Van Haastert and De Wit, 1984).

Figure 2.9B shows that there is also a delay between the dynamics of GEF and GAP before eventually reaching the same steady state. The delay is due to the difference in dissociation constants for both protein variables. A transient response can be seen in the RasGTP dynamics, where the increase is sharp and almost linear like in the early

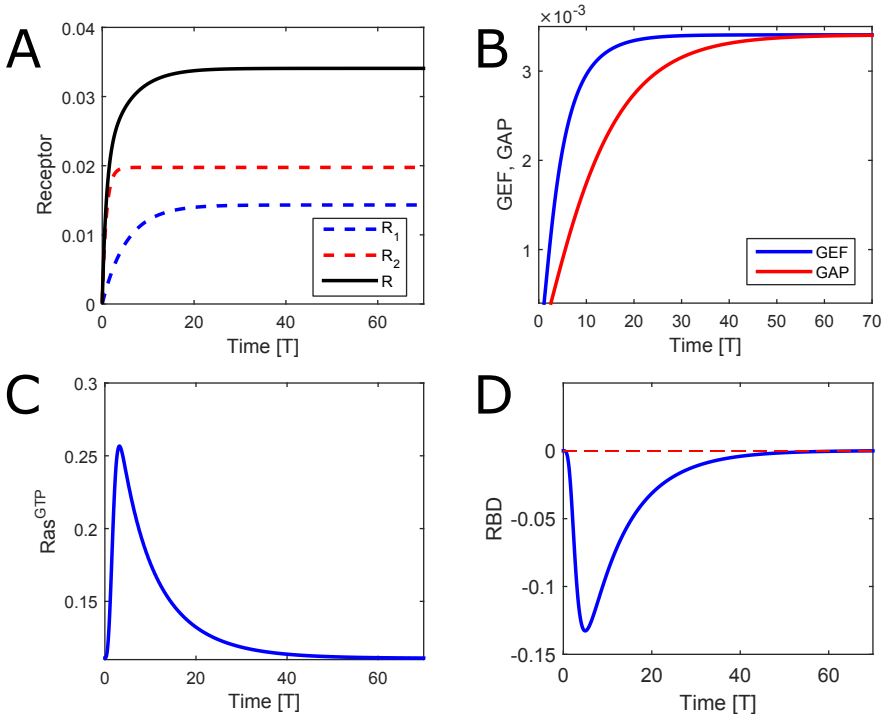

Figure 2.9: Dynamics of the incoherent feedforward model ODEs characterized by equation 2.8 to equation 2.14. cAMP step input is set as $x = 1$ and $x' = 10$. Parameters are set as the result of estimation by Takeda et al. (2012) using simulated annealing where $k_{R1} = 0.00267, k_{-R1} = 0.16, k_{R2} = 0.00244, k_{-R2} = 1.1, r_1 = 0.012, r_2 = 0.115, k_{GEF} = 0.04, k_{-GEF} = 0.4, k_{GAP} = 0.01, k_{-GAP} = 0.1, Ras^{tot} = 1, k_{Ras} = 390, k_{-Ras} = 3126, RBD^{tot} = 1, k_{off} = 0.53, k_{on} = 1$.

period followed by a gradual return (adaptation) to its basal level (Figure 2.9C). The dynamics of RasGTP is mimicked inversely by its reporter protein RBD, as can be seen in Figure 2.9D.

2.5.4 Incoherent feedforward network by Takeda et al. (2012) does not exhibit exact FCD

Here we show how the incoherent feedforward network by Takeda et al. (2012) does not exhibit exact FCD. In order for network motifs to exhibit exact FCD, the output of a network motif in response to fold change in input must satisfy the properties below as illustrated in Figure 2.10.

- The peak response must be proportional to the fold change in the input signal (Weber's Law).
- The output must demonstrate exact adaptation by gradually returning to its pre-stimulus level in the continuous presence of increased input signal.

- The response must exhibit temporal adaptation dynamics where its duration and amplitude must be the same when stimulated with inputs of the same fold change.

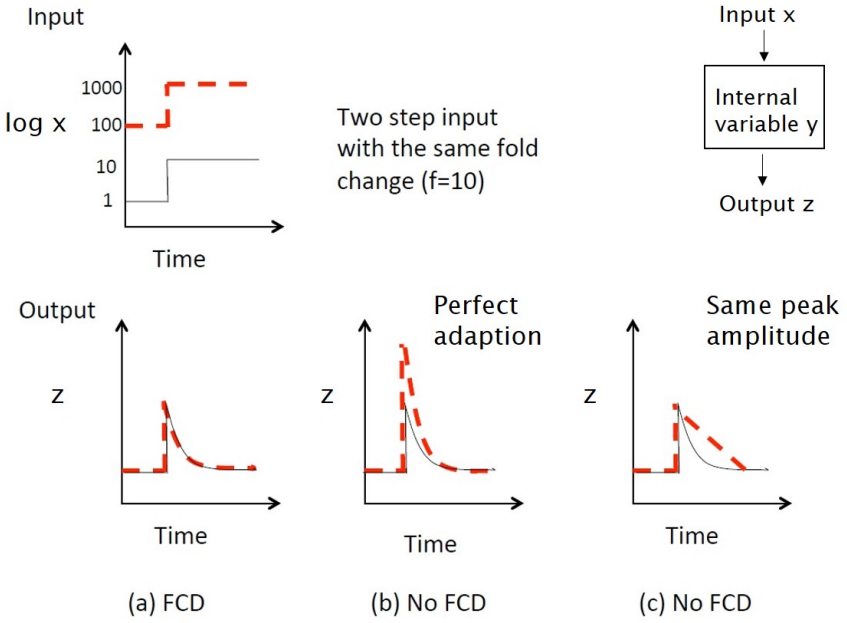

Figure 2.10: Characterization of exact FCD re-illustrated from Shoval et al. (2010) and Skataric et al. (2014) to show how a system with FCD responses to a two step input stimuli. (a) Output z is identical for both step inputs. (b) No FCD due to difference in peak amplitude. (c) No FCD due to the difference in the output shape.

All of the network motifs in Figure 2.7 are shown to have the properties listed above and therefore demonstrate exact FCD. However, as shown in Figure 2.11, the incoherent feedforward of the model ODEs (equation 2.8 to equation 2.13) does not exhibit exact FCD but an 'FCD-like' behaviour. As can be seen from Figure 2.11, when the model ODEs is stimulated with two step inputs of the same fold but of different absolute levels, the responses of RasGTP are not identical. However, exact adaptation and similar temporal dynamics are observed eventhough the peak amplitudes are different. We do not expect the model ODEs to exhibit exact FCD as it is a much more complex system of equations compared to the simplified three node incoherent feedforward network in Figure 2.7A. Furthermore, the parameter range that allows the model ODEs to exhibit FCD is also constrained by the relative dynamics of GEF and RasGTP. Hence, one the objectives of this thesis is to quantify how identical are responses of the model ODEs to the same fold inputs of different absolute levels.

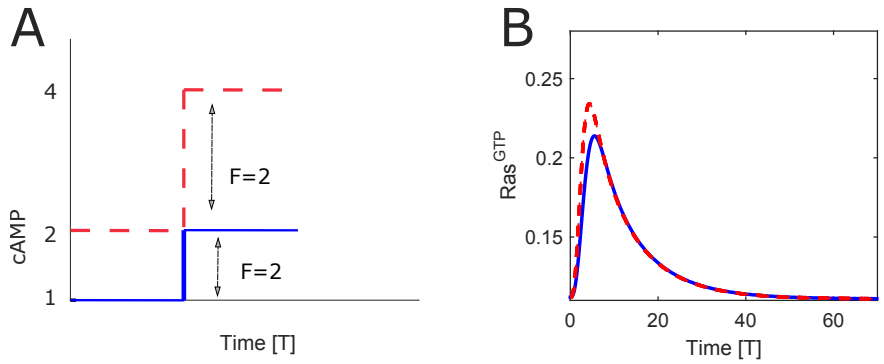

Figure 2.11: Incoherent feedforward loop model by Takeda et al. (2012) exhibit an 'FCD-like' behaviour instead of exact FCD to input cAMP of fold $F = 2$. (A) Two step inputs with different background level but the same fold (B) Solid blue line is the response to stimulus cAMP from 1 to 2. Dashed red lines indicate response to stimulus cAMP from 2 to 4. Parameter settings are the same as in Figure 2.9.

2.5.5 Paradoxical components

Aside from showing the same response characteristics as underlined in Figure 2.10, there is a recurring theme among the network motifs in Figure 2.7. In all network motifs of Figure 2.7, output Z is simultaneously activated by X and inhibited by Y. This antagonistic feature or 'paradoxical components' by different nodes on the same target node is also found in many biological systems as reviewed by Hart and Alon (2013). One explanation given is that opposing effectors yield desirable biological functions (Hart et al., 2012). In the context of the incoherent feedforward network, it has been suggested that the inhibitor Y in IFFL-1 acts as a reference memory, enabling comparison of current and previous level of inputs (Goentoro et al., 2009). Therefore, paradoxical components are vital for a system to exhibit FCD (Hart and Alon, 2013). However, although FCD requires paradoxical components, having paradoxical components in a network does not necessarily guarantee FCD. An example is the integral feedback network motif which also has paradoxical components but does not exhibit FCD.

2.5.6 Design principles of FCD

The idea that there exist a reccuring theme across organisms and systems such as the paradoxical components in the previous section leads to the study of design principles of biological systems. One prime example is the recurring network motifs found in the gene transciption network of *Escherichia coli* bacteria (Shen-Orr et al., 2002; Alon, 2007b). A more related example is the network motifs for adaptation where an exhaustive search of ~16,000 three node networks showed that only the incoherent feedforward and negative feedback loop with a buffer node motifs exibit adaptation (Ma et al., 2009). Although there are studies focused on mapping biological functions to network motifs (Mangan

and Alon, 2003; Mangan et al., 2003), it still remain a much disputed approach (Ingram et al., 2006; Macía et al., 2009).

Design principles of FCD is not limited to the inferrence of network motifs only. Another approach is to understand the generalizable biophysical laws as introduced in section 2.4.2. If the fold-intensity relation does follow the Weber's Fechner law, then it also implies the possibility that *Dictyostelium* chemotaxis is based upon logarithmic tracking of cAMP gradient concentration rather than counting the absolute number of cAMP molecules. This is not the first time that the chemotaxis of a single cell organism is suggested to be based upon logarithmic sensing. In an earlier study by Tu et al. (2008), it has been shown that the input-output relationship between ligand concentration and kinase activity rate in the *E.coli* chemotaxis is well described by the logarithmic law. The logarithmic sensing behaviour in the chemotaxis of *E.coli* bacteria was confirmed through fluorescent resonance energy transfer (FRET) measurement on the bacteria's adaptation time(Lazova et al., 2011). A noninvasive method was conducted by Masson et al. (2012) which reached the same conclusion.

2.6 Summary

In this chapter we have reviewed the biological context of FCD. By identifying exactly in which process FCD is observed, the role of FCD at the level of both single cells and population of cells can be understood and appreciated. The detailed review of the experiment of *Dictyostelium* cells to stimulus of cAMP by Takeda et al. (2012) reveals that the FCD responses said to be observed is poorly characterized. The responses of the mathematical model of *Dictyostelium* signalling pathway by Takeda et al. (2012) does not exhibit FCD as opposed to skeletal networks suggested by Goentoro et al. (2009) and Shoval et al. (2010). In the next chapter we ask whether it is possible to analyse the characteristics of FCD in a complex but biologically more realistic model that does not exhibit exact FCD.

Chapter 3

Model analysis and parameter estimation

3.1 Introduction

We begin our journey to characterize the accuracy of FCD found in *Dictyostelium* cells by first exploring the qualitative behaviour of the model ODEs by Takeda et al. (2012). As previously stated in section 1.2, the model ODEs by Takeda et al. (2012) was structured to study the adaptation behaviour of *Dictyostelium* cells instead of fold change detection. Hence we need to asses whether the model has the right properties required for its responses to exhibit FCD. Mathematical proofs provided by Shoval et al. (2010) underlined the necessary conditions for a system of ODEs to exhibit FCD - that the system must show exact adaptation and is stable. In order to confirm that the model ODEs has the stated necessary conditions, we first investigate the steady state of the model to check for exact adaptation. This is followed by a linear stability analysis to evaluate the stability of the model.

Once we have verified that the model is suitable for the research of FCD, the model ODEs parameters are estimated using the Approximate Bayes Computation-Sequential Monte Carlo (ABC-SMC) method (Toni et al., 2009). The aim here is to fully exploit the potential of the model ODEs in capturing the FCD behaviour by looking at parameter ranges that fits the experiment data by Takeda et al. (2012). The posterior distributions of parameters then serves as the basis on which we investigate the accuracy and limitation of the model in detecting fold change.

3.2 Model analysis

Adaptation, where transient changes in the output returns to a pre-stimulus basal level is an integral component of FCD. The model ODEs (equation 2.8 to equation 2.14) fitted by Takeda et al. (2012) to experiment data of *Dictyostelium* cells response to stimulus cAMP is not only sensitive to a wide range of stimulus cAMP but consistently returns to its pre-stimulus steady state. Therefore it is claimed that this is a clear indication the model describes the adaptation observed in the experiment well. Takeda et al. (2012) attributed the success of capturing adaptation behaviour by the model to two factors. First is the fact that the inclusion of activation of RasGTP by RasGEF and the degradation of RasGTP protein production by RasGAP are in line with the local excitation-global inhibition (LEGI) model (Xiong et al., 2010) for gradient sensing. Second is the delay observed between the activation and degradation kinetics of the two proteins with conflicting molecular functions. This delay is not only vital for adaptation but has also been shown to be an indispensable factor for systems based on activation-degradation rather than activation-inhibition element to yield FCD (Goentoro et al., 2009). Takeda et al. (2012) further showed that different versions of the model can also fit and show adaptation as long as the activator-inhibitor element remains at the centre of the incoherent feed forward loop network motif.

Here we explore the 'adaptability' of the model ODEs by Takeda et al. (2012). Specifically we ask, does the model also shows adaptation for continuously increasing stimulus? In the study of adaptation such as Takeda et al. (2012) and Ma et al. (2009), models are given step inputs whereby adaptation kicks in when the new level of input persists uniformly. However if the input changes such that it increases continuously with time, does the model remains sensitive or does adaptation prevails?. A stable steady state of RasGTP does not necessarily guarantee adaptation. Hence the goal here is to compound the stability of the model with adaptability.

3.2.1 Steady State analysis to verify exact adaptation property

The steady states for the variables in equation 2.5.3 are found by setting the derivatives of each variables to zero and derived as

$$R_{i_{ss}} = \frac{R_i^{tot}}{1 + \frac{k_{dR_i}}{cAMP + r_i}} \tag{3.1}$$

$$R_{ss} = R_{1ss} + R_{2ss} \tag{3.2}$$

$$GEF_{ss} = \frac{R_{ss}}{k_{dGEF}} \tag{3.3}$$

$$GAP_{ss} = \frac{R_{ss}}{k_{dGAP}} \tag{3.4}$$

$$Ras_{ss}^{GTP} = \frac{Ras^{tot}}{1 + k_{dRas}\frac{GAP_{ss}}{GEF_{ss}}} \tag{3.5}$$

where the $k_{dR_i} = k_{-R_i}/k_{R_i}, k_{dGEF} = k_{-GEF}/k_{GEF}, k_{dGAP} = k_{-GAP}/k_{GAP}, k_{dRas} = k_{-Ras}/k_{Ras}$ and $k_{dRBD} = k_{off}/k_{on}$ are the dissociation constants for receptor populations $R_i, i = 1, 2$ and proteins RasGAP, RasGEF, RasGTP, RBD respectively. The steady state for the total receptor is taken as a cumulative effect of each receptor populations as $R_{ss} = R_{1ss} + R_{2ss}$. We ignore the variable of protein RBD as it serves only as a reporter for the measurement of our protein of interest-RasGTP .

As more molecules cAMP bind to the membrane surface receptors such that $1 \gg k_{dR_i}/(cAMP + r_i)$ in equation 3.1, the steady state for each receptor population can be approximated as $R_{i_{ss}} \approx R_i^{tot}$. Hence, the level of R_{iss} is limited by the total number of the receptors R_i^{tot} in the population and increasing cAMP concentration beyond the capacity of R_i^{tot} will not increase the level of the steady state as all receptors are bound. Consequently R_{ss} is limited by both R_{1ss} and R_{2ss}.

Downstream of the receptors, the steady state of RasGEF and RasGAP proteins are effectively determined by R_{ss} and dissociation constants k_{dGEF} and k_{dGAP}. If the dissociation constants between both proteins are the same $k_dGEF = k_dGAP$ and if the kinetics rates of activator RasGEF always surpass RasGAP such that $k_{GEF} \gg k_{GAP}$ and $k_{-GEF} \gg k_{-GAP}$, RasGEF and RasGAP will eventually reach the same steady state level albeit at a different rate where RasGAP lags behind.

Because the dissociation constants $k_dGEF = k_dGAP$ are the same, the ratio between the steady states GEF_{ss} and GAP_{ss} is $GAP_{ss}/GEF_{ss} = 1$. Therefore the asymptotic behaviour of RasGTP in equation 3.5 will always reach the same steady state determined by k_{dRas}, Ras^{tot} independent of the increase in stimulant cAMP. In summary, the adaptation of the model ODEs is achieved by the physical limitation on the number of molecules that bind the membrane surface receptors and when the necessary conditions $k_{GEF} \gg k_{GAP}, k_{-GEF} \gg k_{-GAP}$ and $k_dGEF = k_dGAP$ are met.

3.2.2 Linear Stability analysis to verify the stability of model ODEs

Once we have established that the model's capacity to exhibit adaptation is sustainable if we compel the activator-degradation kinetics to a certain range, we ask whether the system is stable. Specifically we explore the eigenvalues of the system's Jacobian evaluated at steady states. We begin by simplifying the notation of equation 2.8 to equation 2.13 where the variables and constants are expressed as $x = cAMP, A = GEF, B = GAP, k_A = k_{GEF}, k_{-A} = k_{-GEF}, k_B = k_{GAP}, k_{-B} = k_{-GAP}, Y = Ras^{GTP}, Y^{tot} = Ras^{tot}, k_y = k_{Ras}, k_{-y} = k_{-Ras}$. $R = R1 + R2$ is substituted into equation 2.11 and 2.12 to make the role of the two receptors visible and explicit. The model ODEs can then be rewritten as

$$\frac{dR_1}{dt} = k_{R1}(x + r_1)(R_1^{tot} - R_1) - k_{-R1}R_1 \tag{3.6}$$

$$\frac{dR_2}{dt} = k_{R2}(x + r_2)(R_2^{tot} - R_2) - k_{-R2}R_2 \tag{3.7}$$

$$\frac{dA}{dt} = k_A(R1 + R2) - k_{-A}A \tag{3.8}$$

$$\frac{dB}{dt} = k_B(R1 - R2) - k_{-B}B \tag{3.9}$$

$$\frac{dY}{dt} = k_yA(Y^{tot} - Y) - k_{-y}BY \tag{3.10}$$

By deriving partial derivatives of each equation with respect to variables $R1, R2, A, B, Y$ the Jacobian matrix $\mathbf{J}$ is derived as

$$\mathbf{J} = \begin{bmatrix} -k_{R1}(x + r_1) - k_{-R1} & 0 & 0 & 0 & 0 \\ 0 & -k_{R2}(x + r_2) - k_{-R2} & 0 & 0 & 0 \\ k_A & k_A & -k_{-A} & 0 & 0 \\ k_B & k_B & 0 & -k_{-B} & 0 \\ 0 & 0 & k_yY^{tot} - k_yY & -k_{-y}Y & -k_yA - k_{-y}B \end{bmatrix} \tag{3.11}$$

Solving the eigenvalues by setting the determinant $det(\mathbf{J} - \lambda I) = 0$,

$$\begin{aligned}
\lambda_1 &= -k_{R1}(x + r_1) - k_{-R1} \\
\lambda_2 &= -k_{R2}(x + r_2) - k_{-R2} \\
\lambda_3 &= -k_{-A} \\
\lambda_4 &= -k_{-B} \\
\lambda_5 &= -k_y A - k_{-y} B
\end{aligned}$$

If all the eigenvalues are negative real numbers then the system is stable (Strogatz, 2018). Any eigenvalue with positive real number would lead to one of the solutions increasing exponentially. λ_3 and λ_4 are negative real numbers due to $k_{-A} \geq 0$ and $k_{-B} \geq 0$. The eigenvalues λ_1 and λ_2 are directly dependent on input x while λ_5 is indirectly influenced by x through A and B. Due to enzymatic constants and input x are always real positive values, λ_1, λ_2 and λ_5 are always real negative values. As input $x \to +\infty$, the eigenvalues $\lambda_{1,2,5} \to -\infty$, therefore the stronger the input, the system is more stable.

To illustrate how the dynamics of the model changes with respect to a continuously increasing input, we numerically solved the model ODEs for a linear and exponential cAMP input and show the result in Figure 3.1. Refer to the second column of table 3.1 for the set of parameter values. The same parameters are used for the computation of responses to linear and exponentially changing input. The result shows that the primary difference lies in the adaptation rate for protein RasGTP variable. The time for RasGTP protein to return back to its steady state level is significantly longer for when the input is exponential compared to linear input.

3.3 Bayesian parameter estimation

In the previous section, we have verified that the model ODEs by Takeda et al. (2012) satisfies the necessary conditions for a dynamical system to exhibit FCD as underlined by Shoval et al. (2010). In this section, we describe the Approximate Bayes Computation-Sequential Monte Carlo (ABC-SMC) algorithm used to estimate the distributions of posterior parameters of the model ODEs. We also describe the dataset used for fitting and constraints that we have imposed on the parameter space. The objective here is to derive the operating ranges of parameters of the model that is compatible with experimental data said to exhibit FCD and thus capturing the parameter ranges for the model to exhibit FCD.

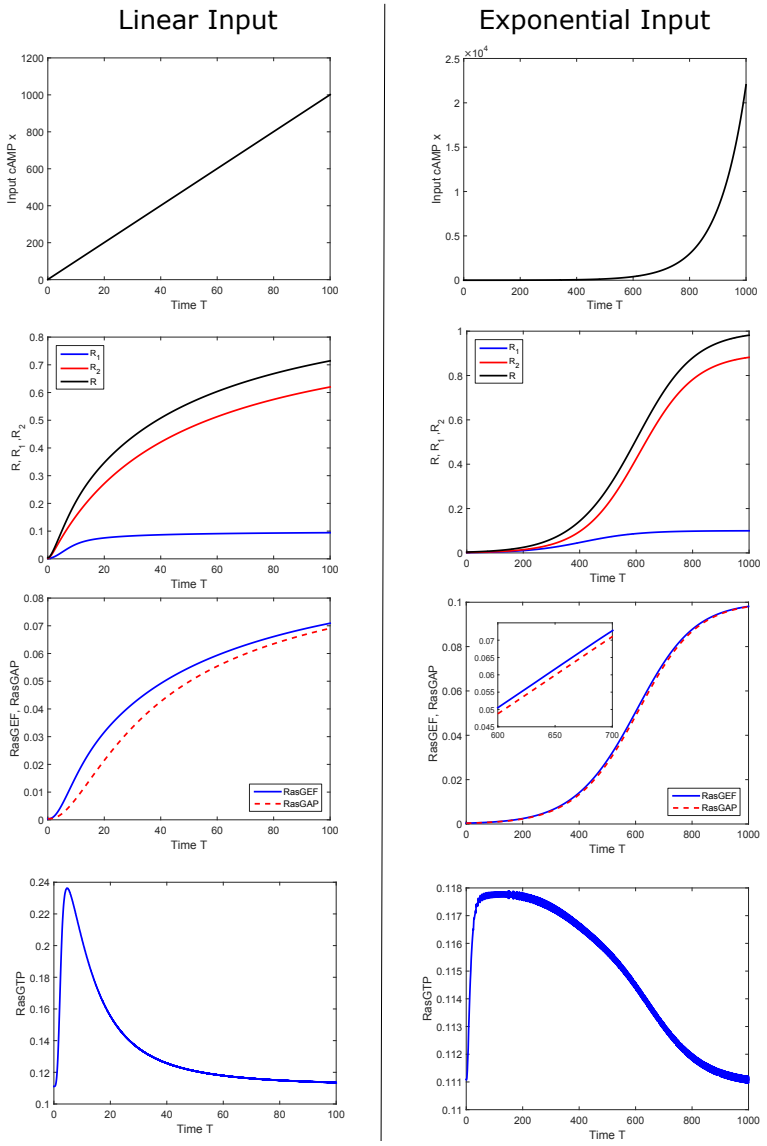

Figure 3.1: An example of the dynamics of protein variables in equation 2.8 to equation 2.13 when the input cAMP is a linear function $x(t) = 10t$(Left column) and exponential function $x(t) = e^{0.01t}$ (Right column). For the exponential function, the delay between the activator-degrader protein variable is visible when zoomed in as shown in inset figure. Bottom most panels shows the protein of interest, RasGTP where the transient response returns to basal level and shows adaptation.

3.3.1 Approximate Bayes Computation-Sequential Monte Carlo (ABC-SMC)

We take the view that a single set of parameters $\boldsymbol{\theta} = (\theta_1, \ldots, \theta_m)$ in the model ODEs does not reflect either the biological reality of natural variation in protein levels (Raj and van Oudenaarden, 2008) or of the mathematical equivalence of multiple parameter fits of ODE models to a set of empirical data (Gutenkunst et al., 2007). In order to quantify the uncertainties in estimating the parameters, we apply here the Approximate Bayesian Computation-Sequential Monte Carlo (ABC-SMC) method to derive posterior distributions of parameters rather than their point estimates. In this method, a simulated observation is derived from a generative model with the parameter values of the model sampled from a pre-defined prior distribution. The error between simulated and experimental data is then computed and the rejection or retainment of a sample parameter is based on whether the computed error is within a pre-determined threshold level or not. This process is then repeated for the number of samples that we want to estimate.

In this thesis we specifically estimated the posterior probability of the set of parameters $\boldsymbol{\theta} = (\theta_1, \ldots, \theta_{10})$ in table 3.1 given the set of fixed parameters and the selected 16 experimental data points $X_d \in D$ as

$$P_\epsilon(\boldsymbol{\theta}, X_s|X_d) = \frac{\mathbb{1}_{A_{\epsilon,X_d}}(X_s) f(X_s|\boldsymbol{\theta})\pi(\boldsymbol{\theta})}{\int_{X_s}\int_{\boldsymbol{\theta}} f(X_s|\boldsymbol{\theta})\pi(\boldsymbol{\theta})d\boldsymbol{\theta}dX_s} \tag{3.12}$$

where $\pi(\boldsymbol{\theta})$ is the prior probabilities from a uniform distribution characterized by the upper and lower bounds as listed in table 3.1. $\epsilon > 0$ indicates the tolerance threshold and $\mathbb{1}_A(.)$ is the indicator function of a given set A. A_{ϵ,X_d} is the set of simulated observations close to the true experiment data defined by the distance function as

$$A_{\epsilon,X_d} = \left\{ X_s \in D | \triangle(X_s, X_d) \leq \epsilon \right\} \tag{3.13}$$

where $\triangle(X_d, X_s)$ is the distance function between experiment data X_d and simulated data X_s. X_s is simulated from a generative model M_θ denoted as $X_s \sim M_\theta$ where in our case M_θ is the model ODEs. One of the advantages of the ABC-SMC method is that it removes the evaluation of likelihood of observing a data given parameter $f(X_d|\theta)$ by comparing the simulated observations X_s to X_d. If the sampled set of parameters $\boldsymbol{\theta}_k$ resulted in X_s such that $\triangle(X_s, X_d) \leq \epsilon$ then the sample $\boldsymbol{\theta}_k$ is retained. Hence the computational burden lies in the repetition of solving the model ODEs numerically for a particular step input of x, x' to obtain I_p and T_p close to the selected data points used for data fitting.

As ABC-SMC is a sample filtering algorithm, the goal is to find N samples of $\boldsymbol{\theta}$ filtered through $T = 1, \ldots, t_m$ levels where here we set $t_m = 30$ and $N = 1000$. The error by a sample parameter $\boldsymbol{\theta}$ is derived by computing the distance between simulated X_s and experimental X_d data as

$$\triangle(\boldsymbol{\theta}|X_d, X_s) = \frac{1}{K}\sum_{i=1}^{K}\left(\frac{X_{d_i} - X_{s_i}}{\sigma_{d_i}}\right)^2 \tag{3.14}$$

where the simulated observation at data point i is generated from the model ODEs with corresponding step input $X_{s_i} \sim M_\theta(x_i, x_i')$. $K = 16$ (further explained in the next subsection), is the total data fitted, σ_{d_i} is the standard deviation for X_{d_i}. The set of errors at a particular filter level $T = t$ is then denoted as a vector $\mathbf{E}_t = (\triangle_t(\boldsymbol{\theta}_1), \ldots, \triangle_t(\boldsymbol{\theta}_N))$ where the notation $\triangle_t(\boldsymbol{\theta}) = \triangle_t(\boldsymbol{\theta}|X_d, X_s)$ is introduced for brevity. The tolerance level at filter level $T = t+1$ is denoted as ϵ_{t+1} and is set as $\epsilon_{t+1} = 0.8\mathbf{E}_t$. A generated sample $\boldsymbol{\theta}_k$ at filter level $t+1$ is accepted if $\triangle_{t+1}(\boldsymbol{\theta}_k) \leq \epsilon_{t+1}$. The generation of samples stops when the difference between tolerance level is $\epsilon_t - \epsilon_{t-1} < \alpha$ or when $T = 30$ population level is reached.

The result of population of N samples evaluated at the last filtered level $T = t_m$ is a $N \times m$ matrix denoted as $\boldsymbol{\Theta} = (\boldsymbol{\theta}^1, \ldots, \boldsymbol{\theta}^N)^\intercal, \boldsymbol{\Theta} \in \mathbb{R}^{N \times m}$. Here $m = 10$ represents the ten different parameters estimated as listed in table 3.1. The i^{th} row is a vector representing the i^{th} set of estimated parameters $\boldsymbol{\theta}^i = (\theta_1^i, \ldots, \theta_{10}^i), i \in N$. The j^{th} column is a vector representing the posterior density for the j^{th} estimated parameter $\boldsymbol{\theta}_j = (\theta_j^1, \ldots, \theta_j^N)^\intercal, j \in m$. Therefore instead of deriving a point estimate for parameter θ_j, we have a population of estimates denoted as $\boldsymbol{\theta}_j$. Hence, this population of estimates is our approximation to the posterior density of parameter θ_j.

3.3.2 Data fitting

In estimating the model ODEs parameters, we compare our estimates with those of Takeda et al. (2012) and specifically the dose-peak response of Figure 2C and dose-time to peak response of Figure 2D of the same paper. Thus wherever possible we adopted the same approach as implemented by Takeda et al. (2012). We chose to stimulate the model ODEs also with a step input and in fitting the data, we selected 16 of 21 discrete experimental data points chosen by the Takeda et al. (2012). 8 data points are of the peak responses (I_p) and 8 others are of their corresponding time to peak responses (T_p) of when cells were stimulated with various level of cAMP but with background concentrations of 0nM and 100nM. The data points of stimulation by 1μM in background cAMP of 0nM are not selected as they are used for normalization. The remaining 5 data points as chosen by Takeda et al. (2012) are not selected here as the magnitude of the inputs

have already been represented by the 16 data points and therefore the inclusion would only contribute to overfitting and an added burden to the computational resource.

The estimated and fixed parameters are explicitly listed in table 3.1. The fixed parameters are set with values derived by Takeda et al. (2012). As can be seen from table 3.1, there are two type of receptors denoted by R_1 and R_2. This is to reflect two population of receptors with different affinities of 60nM and 450nM for R_1 and R_2 as derived from their respective dissociation constant $k_{di} = k_{-Ri}/k_{Ri}$. Individual parameters to be estimated is denoted here as θ where θ_i indicates the i^{th} parameter and is randomly generated in an optimisation procedure (further described in the next section) from a uniform distribution with an upper and lower bound based on values derived by Takeda et al. (2012). For example, if the value estimated by Takeda et al. (2012) for parameter θ_i is x then the bounds are set as $x \pm (0.95 \times x)$. As can be seen from table 3.1, the degradation rates of RasGEF and RasGAP protein are estimated such that the relation of $k_{dGEF} = k_{dGAP}$ is maintained. Hence, there will always be a delay between the dynamics of RasGAP and RasGEF and further ensuring that the FCD behaviour is captured. We have also set the condition such that $R_2^{tot} + R_1^{tot} = 1$.

Table 3.1: Fixed and estimated parameters of the model ODEs. R_2^{tot} is estimated as $R_2^{tot} = 1 - R_1^{tot}$, hence there is no upper and lower bound set.

Parameter	Derived by Takeda et al. (2012)	Upper Bound	Lower Bound	Unit
Fixed				
k_{R1}	0.00267			$\text{nM}^{-1}sec^{-1}$
k_{R2}	0.00244			$\text{nM}^{-1}sec^{-1}$
k_{-R1}	0.16			sec^{-1}
k_{-R2}	1.1			sec^{-1}
k_{GEF}	$0.1 * k_{-GEF}$			sec^{-1}
k_{GAP}	$0.1 * k_{-GAP}$			sec^{-1}
Ras^{tot}	1			
RBD^{tot}	1			
Estimated θ				
$\theta_1 : r_1$	0.012	0.023	6×10^{-4}	nM
$\theta_2 : r_2$	0.115	0.224	0.005	nM
$\theta_3 : R_1^{tot}$	0.1	1	0	
$\theta_4 : R_2^{tot}$	0.9			
$\theta_5 : k_{-GEF}$	0.4	0.78	0.02	sec^{-1}
$\theta_6 : k_{-GAP}$	0.1	0.195	0.005	sec^{-1}
$\theta_7 : k_{Ras}$	390	760.5	19.5	sec^{-1}
$\theta_8 : k_{-Ras}$	3126	6095.7	156.3	sec^{-1}
$\theta_9 : k_{off}$	0.53	1.034	0.027	sec^{-1}
$\theta_{10} : k_{on}$	1.0	1.95	0.05	sec^{-1}

3.4 Posterior parameter distribution

The correct way to think about the distributions

The result of estimating 1000 samples for all parameter $\boldsymbol{\theta}_j, \forall j \in m$, using the described ABC-SMC method is shown as histogram plots in Figure 3.2 where the histograms are the last filtered sample populations. We consider Figure 3.2 as an approximation of the posterior distributions of parameters conditioned on the fixed parameters. Here we denote the set of fixed parameters in table 3.1 as $\boldsymbol{\theta}_{\text{fix}}$. Each parameter $\theta_j^i, i \in N, j \in m$ have been chosen randomly from a uniform prior. However, one randomly chosen prior parameter requires the right combination of other randomly chosen priors in order to achieve an acceptable solution of the model ODEs as required by the distance function. This is an indicator that elements of dependency exists. Therefore it is more accurate to view the whole of Figure 3.2 as a posterior of joint distribution of a 10 dimensional parameters conditioned on the fixed parameters denoted as $p(\theta_1, \ldots, \theta_{10}|\boldsymbol{\theta}_{\text{fix}})$, with each individual distributions the marginal posterior $p(\theta_j|\boldsymbol{\theta}_{\text{fix}}) = \int p(\theta_1, \ldots, \theta_j, \ldots, \theta_{10}|\boldsymbol{\theta}_{\text{fix}})$. The mean, standard deviation, coefficient of variance and median statistics of each distribution in Figure 3.2 are summarised in table 3.2.

Table 3.2: Statistics of the estimated marginal posterior distribution of parameters in Figure 3.2.

Parameter θ	Mean μ	Std Dev σ	Coefficient of Var c_v	Median
$\theta_1 : r_1$	0.0121	0.0060	0.4990	0.0122
$\theta_2 : r_2$	0.1248	0.0472	0.3781	0.1220
$\theta_3 : R_1^{tot}$	0.1387	0.0686	0.4944	0.1333
$\theta_4 : R_2^{tot}$	0.8613	0.0686	0.0796	0.8667
$\theta_5 : k_{-GEF}$	0.5200	0.1269	0.2440	0.5201
$\theta_6 : k_{-GAP}$	0.1036	0.0178	0.1715	0.1041
$\theta_7 : k_{Ras}$	537.18	125.74	0.2341	544.22
$\theta_8 : k_{-Ras}$	2786.04	878.19	0.3152	2655.98
$\theta_9 : k_{off}$	0.2264	0.0920	0.4065	0.2095
$\theta_{10} : k_{on}$	1.2248	0.3888	0.3175	1.2180

Distributions of parameters in sensing defined and undefined fold change in input.

What does the distribution indicate in the context of the cell? Note that we also fitted the parameters to measurements of cells response when stimulated with initial cAMP $x = 0$nM. Stimulation in no background cAMP $x = 0$nM entails an undefined fold change in input- the cell has no information on the previous cAMP to compare to. Hence Figure 3.2 indicates the range of possible parameter values the modelled upstream process of

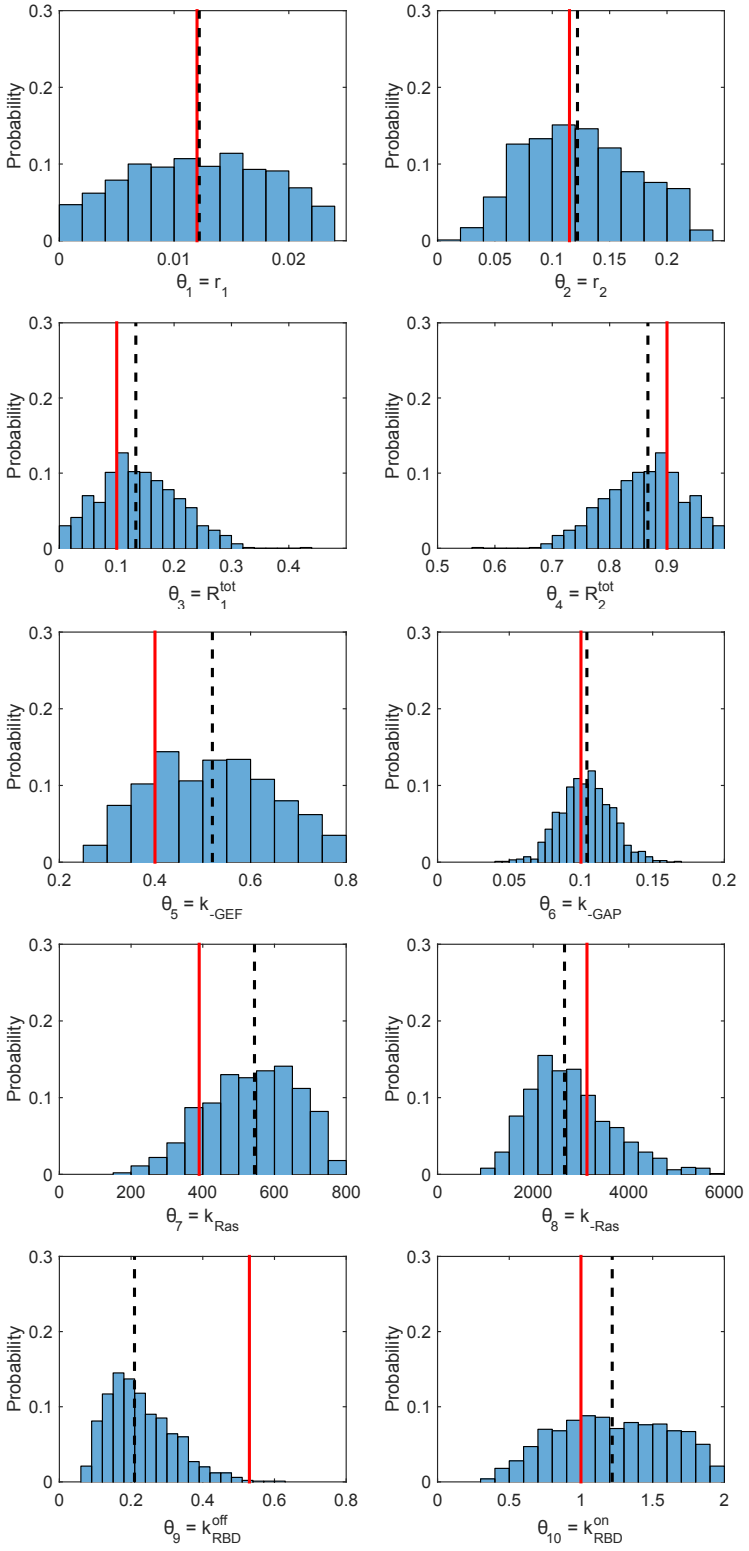

Figure 3.2: Posterior parameter distributions derived using the ABC-SMC estimation method and shown as histogram plots. Each distribution consists of 1000 samples. Distribution of θ_3 mirrors θ_4 due to the ratio of receptors population $R^{tot} + R_2^{tot} = 1$. Vertical red lines indicate parameter as estimated by Takeda et al. (2012). Black dashed lines indicates the median of each posterior distributions.

Dictyostelium operates in order to sense both defined and undefined fold change in input. Fitting to only experiment data that has a defined fold change in cAMP would not be a fair representation of the cells parameter because in natural environment they are likely to encounter both scenarios.

Inferring from variability the significance of parameters in the FCD mechanism

What information does the marginal posteriors and its statistics tells us about FCD in *Dictyostelium*? It is found that in sensing both defined and undefined fold change, certain parameters have lesser variability than others (stiff). An example is the deactivation of GAP by k_{-GAP} constant indicated by the 17% coefficient of variance(table 3.2). (Note that coefficient of variance is used to compare variability because the parameters are of different units of measurements.) On the contrary, certain parameters has a more flexible range. Two examples are the receptor activation constant r_1 and protein RBD degradation constant k_{off} as indicated by their 49 % and 40% coefficient of variances respectively. Large variability may imply that it does not really matter what values these parameters take in order for the cell to sense fold change. Thus, the variability in parameters is an initial indicator of the significance of each parameter and as an extension, the role of each protein itself in the fold-change input sensing mechanism.

Characteristics of the underlying distributions

Figure 3.2 also reveal characteristics that may hint to what each underlying distributions are. For example a Gaussian might describe k_{-GAP} distribution well due to the symetricness of the posterior. The marginal posterior for k_{RBD}^{off} is a right tailed distribution and positive and negative skewness is observed in the distribution of k_{Ras} and k_{-Ras}. R_2^{tot} may be symmetric if the estimation was not limited by its upper bound. A quick inspection of Figure 3.2 also suggests that there is no clear bimodality that can be observed in all parameter distribution.

Distributions are not necessarily centred around Takeda's estimates

In the ABC-SMC parameter estimation process we have centred the uniform priors based on the estimates by Takeda. Let's assume that there exist a true value θ_j^{true} for each parameter θ_j where a set of $\boldsymbol{\theta}^{\text{true}} = (\theta_1^{\text{true}}, \ldots, \theta_{10}^{\text{true}})$ results in an optimal fitting of the model ODEs to the experiment data. If our estimation is also optimal, the set of true parameters $\boldsymbol{\theta}^{\text{true}}$ would then lie within the estimated posterior distribution. Furthermore if we consider Takeda estimates to be the true parameters and assume that our ABC-SMC method is optimal, then Takeda estimates should lie within our posterior

distribution. However, as can be seen from Figure 3.2, this is not the case. Figure 3.2 reveals that while parameters such as r_1, r_2 and k_{-GAP} are distributed around Takeda's estimates, some such as the k^{off}_{RBD} distribution has centres that deviate far from what Takeda had estimated. For comparison purposes we took the median of each distribution and plotted as black dashed-lines in Figure 3.2 where else Takeda's estimates are shown as red lines. The degree of deviation in percentage from what Takeda estimated for each parameter is shown in table 3.3. As expected the median of k^{off}_{RBD} distribution has the highest degree of deviation at 60.46%. Therefore if the assumption that the ABC-SMC is optimal holds, then Figure 3.2 shows that Takeda estimates for parameter such as k^{off}_{RBD} does not approximate well to the true parameters.

Table 3.3: Degree of deviation of the median of the distributions in Figure 3.2 from Takeda's estimates.

Parameter, θ	Median θ^*	Diff (%)
$\theta_1 : r_1$	0.0156	1.63
$\theta_2 : r_2$	0.0779	6.06
$\theta_3 : R^{tot}_1$	0.0852	33.3
$\theta_4 : R^{tot}_2$	1.2015	3.70
$\theta_5 : k_{-GEF}$	0.421	30.02
$\theta_6 : k_{-GAP}$	0.1018	4.14
$\theta_7 : k_{Ras}$	564.37	39.54
$\theta_8 : k_{-Ras}$	2178.9	15.04
$\theta_9 : k_{off}$	0.1815	60.46
$\theta_{10} : k_{on}$	1.0674	21.80

Median of posteriors as the new estimate

Working on the assumption that $\boldsymbol{\theta}^{\text{true}}$ lies within the posteriors, let us consider the set of median values for each parameter as stated in table 3.3 as our estimate $\boldsymbol{\theta}^* = (\tilde{\theta}_1, \ldots, \tilde{\theta}_{10})$ where $\tilde{\theta}_j$ is the median of parameter θ_j. $\boldsymbol{\theta}^*$ approximates $\boldsymbol{\theta}^{\text{true}}$. How well does I_p and T_p responses generated by $\boldsymbol{\theta}^*$ fits the experiment data in comparison to I_p and T_p derived using Takeda estimates? To answer this we solve model ODEs using $\boldsymbol{\theta}^*$ and Takeda estimates for each pair of inputs measured in Figure 2.4A and Figure 2.4B. From the solution of model ODEs, we derived the normalised I_p and T_p with respect to the set of parameters used and plot alongside the experiment data in Figure 3.3. Crosses are the values generated using $\boldsymbol{\theta}^*$ and squares indicates values by Takeda's estimates. Solid and dashed lines are the interpolated values between each data points. The various background cAMP are indicated by different colors(Refer Figure 3.3 for details).

Figure 3.3 shows that I_p derived by $\boldsymbol{\theta}^*$ and Takeda estimates have different projections for all background concentration. In contrast the projections of T_p by both estimator are similar. The deviation of derived I_p, T_p of each estimator from I_p, T_p of the experiment

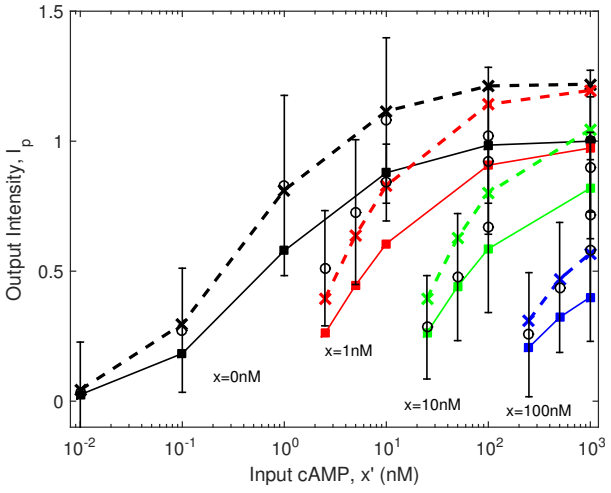

(a)

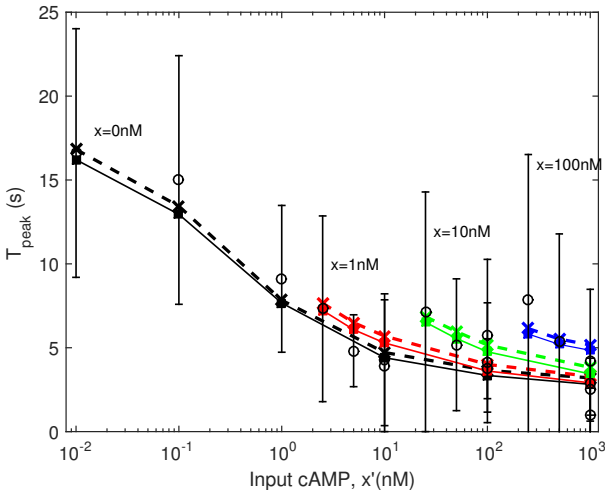

(b)

Figure 3.3: Model responses solved using Takeda's estimates (solid lines and solid squares) and median of posterior $\boldsymbol{\theta}^*$ (dashed lines and crosses). Experiment data is also indicated (black circles with error bars as standard deviations) for comparison. The background concentrations of cAMP are indicated by different colours where black: 0nM, red: 1nM, green: 10nM, blue: 100nM.

data is quantified using the distance function of equation 3.14 and shown in table 3.4. It can be observed that Takeda estimates is closer to the I_p experiment data indicated by the lower error. Both estimates approximates the T_p data similarly although $\boldsymbol{\theta}^*$ perform slightly better.

3.5 Principal Component Analysis

Now that we have estimated 1000 values for each parameter $\theta_j, j \in m$ as in Figure 3.2, we investigated the variance components of the parameters using Principal Component

Table 3.4: Errors.

Estimator	I_p	T_p
Takeda	2.88	37.05
$\boldsymbol{\theta}^*$	5.81	36.34

Analysis (PCA). We ignore the estimated values for $\theta_3 = R_1^{tot}$ because it is already know that its variance is dependent of $\theta_4 = R_2^{tot}$. Let us consider $N \times p$ data matrix $\mathbf{X}$, where in our case $N = 1000$ are the rows of estimated parameter values and $p = 9$ are the columns of the reassigned parameters $\theta_1 = r1, \theta_2 = r2, \theta_3 = R_2^{tot}, \theta_4 = k_{GEF}, \theta_5 = k_{GAP}, \theta_6 = k_{Ras}, \theta_7 = k_{-Ras}, \theta_8 = k_{off}, \theta_9 = k_{on}$. The data matrix $\mathbf{X}$ where $\mathbf{X} \subset \boldsymbol{\Theta}, \mathbf{X} \in \mathbb{R}^{N \times p}$ can be transformed as

$$\mathbf{Q} = \mathbf{P}^\intercal \mathbf{X}^\intercal \tag{3.15}$$

where $\mathbf{P}$ is the $p \times p$ matrix of column eigenvectors $\mathbf{v}_1, \mathbf{v}_2, \ldots, \mathbf{v}_p$ representing the principal components of $\mathbf{X}$ and $\mathbf{Q}$ is a linear combinations of its basis (eigen) vectors. If matrix of parameters $\mathbf{X}$ is denoted as $\mathbf{X} = [\mathbf{x}_1 \ldots \mathbf{x}_p]$ where $\mathbf{x}_j$ is the j^{th} column vector of estimated parameter θ_j, the covariance between parameter θ_j and θ_k is computed as

$$C_{j,k} = \frac{1}{N-1}(\mathbf{x}_j - \mu_j)^\intercal (\mathbf{x}_k - \mu_k) \tag{3.16}$$

where μ_j and μ_k are both the mean for $\mathbf{x}_j$ and $\mathbf{x}_k$. The variance-covariance matrix of $\mathbf{X}$ is then a $p \times p$ matrix denoted as $\mathbf{C}_\mathbf{x}$,

$$\mathbf{C}_\mathbf{x} = \begin{bmatrix} C_{1,1} & \cdots & C_{1,p} \\ \vdots & \ddots & \vdots \\ C_{p,1} & \cdots & C_{p,p} \end{bmatrix} \tag{3.17}$$

where the diagonal $C_{j,j}$ is the variance of parameter θ_j. $\mathbf{C}_\mathbf{x}$ can be computed in matrix notation as $\mathbf{C}_\mathbf{x} = 1/(N-1)\mathbf{X}^\intercal \mathbf{X}$. However, the parameters $\theta_1, \ldots, \theta_9$ are of different units of measurement where θ_1, θ_2 are activation constants r_1, r_2, θ_3 is the proportion of the receptors population R_2^{tot}, while $\theta_4 \sim \theta_9$ are a group of protein activation and degradation constants. To ensure equal weights in the analysis of principal components, the matrix of parameters $\mathbf{X}$ is standardized as $\mathbf{X} = [\mathbf{x}'_1 \ldots \mathbf{x}'_p]$ where $\mathbf{x}'_j$ is the standardized column vector of estimated parameter θ_j computed as

$$\mathbf{x}'_j = \alpha_j(\mathbf{x}_j - \mu_j) \tag{3.18}$$

Table 3.5: All principal components with corresponding parameters and eigenvalues. As shown in Figure 3.4, the first five components consist of 80% variance.

	Components								
Parameter	1	2	3	4	5	6	7	8	9
r_1	-0.005	0.009	-0.009	0.317	0.914	-0.041	0.228	0.099	-0.006
r_2	0.494	0.138	-0.218	-0.355	-0.053	0.230	0.551	0.452	0.004
R_2^{tot}	-0.379	-0.367	0.306	0.005	0.003	0.675	-0.058	0.406	-0.055
k_{-GEF}	-0.083	0.644	0.238	-0.105	0.085	0.058	-0.300	0.266	0.583
k_{-GAP}	-0.457	0.333	-0.144	0.314	-0.232	-0.315	0.190	0.481	-0.374
k_{Ras}	0.257	-0.181	0.624	-0.271	0.089	-0.468	-0.175	0.326	-0.272
k_{-Ras}	-0.479	-0.257	0.108	-0.353	-0.006	-0.324	0.510	-0.085	0.443
k_{off}	0.303	-0.356	0.031	0.615	-0.252	-0.164	0.041	0.274	0.484
k_{on}	-0.096	-0.307	-0.616	-0.295	0.170	-0.189	-0.472	0.361	0.110
eigvalues	2.031	1.785	1.309	1.127	1.021	0.645	0.559	0.291	0.231

Here the mean of $\mathbf{x}'_j$ is shifted to zero and scaled with factor $\alpha_j = 1/\sigma_j$ where σ_j is the standard deviation of estimated parameter θ_j. The corresponding covariance matrix $\mathbf{C_x}$ is a real symmetric matrix where $\mathbf{C_x} = \mathbf{C_x}^\intercal$ due to only real positive numbers are used to estimate the parameters. Therefore covariance matrix $\mathbf{C_x}$ is diagonalizable such that

$$\mathbf{C_x} = \mathbf{P\Sigma P}^\intercal \tag{3.19}$$

where $\mathbf{P}$ is a matrix of orthonormal eigenvectors (eigenvectors are linearly independent with $\mathbf{v}_j \bullet \mathbf{v}_k = 0$ and $|\mathbf{v}| = 1$).$\mathbf{\Sigma}$ is a diagonal matrix of distinct eigenvalues in descending order such that $\lambda_1 > \lambda_1 > \cdots > \lambda_p, \lambda_j \neq \lambda_k$. One desirable property of the transformed matrix $\mathbf{Q}$ is that the covariance matrix of $\mathbf{Q}$, $\mathbf{C_q} = 1/N{-}1(\mathbf{QQ}^\intercal)$ is a diagonal matrix. It has been shown that this can be achieved by using the eigenvectors of covariance matrix $\mathbf{P}$(Shlens, 2014). Hence the eigenvectors of $\mathbf{P}$ represent the principal components of $\mathbf{X}$. The result of computing the eigenvectors for our matrix of parameter $\mathbf{X}$ is shown in table 3.5 alongside with the corresponding eigenvalues. The computed explained variance and cumulative variance for each principal components are shown in Figure 3.4. The result shows that the variance of the posterior parameters can not be represented by any single principal components although 80% of the variance is captured by the first five principal components. Therefore at least five components are needed to preserve 80% variance of the parameters.

3.6 Summary

We have evaluated the suitability of the model ODEs by Takeda et al. (2012) in capturing the FCD behaviour by means of dynamical system analysis. We showed that the model

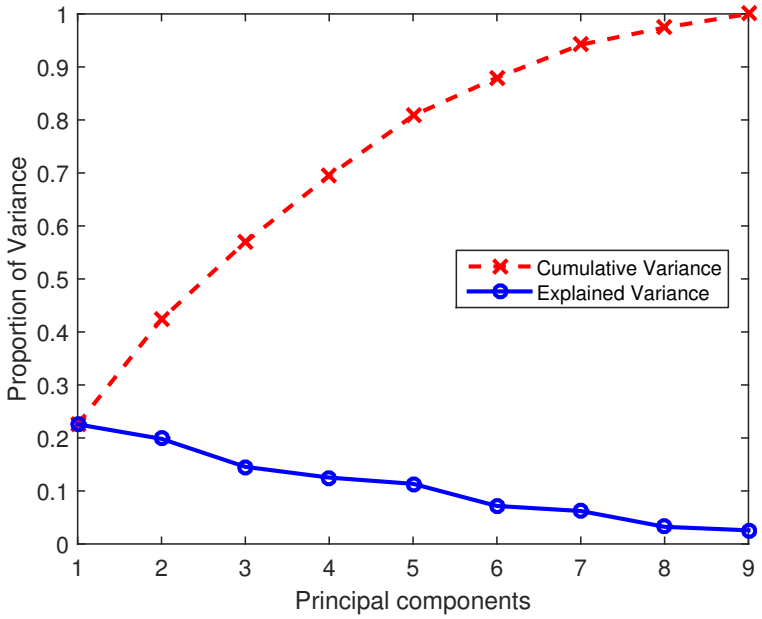

Figure 3.4: Variance of the data contributed by each principal components.The first five principal components captures 80% of the posterior parameters variability.

will always achieve adaptation (one of the necessary components of FCD) even though stimulant increases continuously as opposed to step inputs due to the constraints imposed by the receptor protein population and RasGEF-RasGAP protein on the model. We have also inferred the posterior density of parameters of the model ODEs and provided several interpretations of the result. The population of parameters revealed that the most invariant (stiff) parameter is the k_{-GAP} kinetics of protein RasGAP and distributions are not necessarily centred around estimates by Takeda et al. (2012). The PCA analysis showed that no single principal components dominates the variance of the posterior parameters.

Chapter 4

The accuracy of Fold Change Detection

4.1 Introduction

In an ideal setting, the accuracy of FCD is quantified by measuring individual response of every single *Dictyostelium* cell on earth to various fold changes in the concentration of cAMP. This way we could find the true I_p response of a single cell to a certain fold change F by looking at the consistency of I_p to F of various background cAMP x. However as seen in Figure 2.5, the responses of *Dictyostelium* cells to the same fold change in concentration of cAMP are heterogeneous even when the initial cAMP concentration is identical due to cell-cell variability. It has been shown that although single *Dictyostelium* cells produce consistent responses to the same pulses of cAMP concentration, there is a large variability in responses when a population of cells is stimulated in the same manner (Samadani et al., 2006). The difference in responses by different cells to the same concentration of cAMP is found to be true even if the cells are genetically identical (Wang et al., 2012). It is hard for a population of cells to reach an absolute consensus on the level of I_p it should produce in response to a particular fold stimulus. In this chapter we quantify the accuracy of FCD by looking at the variability of responses derived by the model ODEs based on the estimated posterior parameters. The principle is simple, the population response provides a better view of how confident a particular fold is being sensed.

4.2 Methods of emulating heterogeneity in responses

In the previous chapter, we have inferred posterior distributions $P(\boldsymbol{\theta}|X)$ on the parameter set that is compatible with the observed data X. We take the view that a single set of

parameters $\boldsymbol{\theta} = (\theta_1, \ldots, \theta_m)$ in the system of ODEs does not reflect either the biological reality of natural variation in protein levels Raj and van Oudenaarden (2008). We shall label by i each sample drawn from this distribution $\boldsymbol{\theta}_i \sim P(\boldsymbol{\theta}|X)$. We view every such sample $\boldsymbol{\theta}_i = (\theta_{i,1}, \ldots, \theta_{i,m})$ as an emulation of the cell-cell variability (Samadani et al., 2006; Wang et al., 2012) in the sensing mechanism of *Dictyostelium* . The adaptation displayed by *Dictyostelium* to sustained stimulation by externally applied cAMP (Dinauer et al., 1980b,c) makes the characteristics of the transient response – the magnitude of the peak response I_p and the time taken to reach this peak t_p as visualized in Figure 4.1A – the main empirical quantities of interest.

We stimulate each such virtual cell in the same way as the experimental setup: for a specific background level of cAMP x we introduce a step change of input cAMP concentration $(x' - x)$ with $x' = Fx$ where F is the fold change. We follow the time course of the response in the system of ODEs with parameters $\boldsymbol{\theta}_j$ and measure $I_{p,j}$ and $t_{p,j}$. Hereafter, except for right panel of Figure 4.1A , all I_p values are normalized by I_p derived from stimulating model ODEs parameterised in Takeda et al. (2012) with step input $x = 0, x' = 1000$. The results of simulating 1000 heterogeneous virtual cells $\boldsymbol{\theta}_j$, for all $j = 1, \ldots, 1000$ with $x = 1$ and $F = 2$ is shown in Figure 4.1B as histogram by taking only the I_p value of each time series data of each virtual cells. By simulating a distribution of responses rather than point estimates to a particular step input cAMP x, x' with fold F, we are able to further emulate variability in cell responses within our model constraints. This is important as the experiment results reported in Takeda et al. (2012) (replotted again as Fig 4.1C) shows how cells response to the same fold input varies even in the same background cAMP x, indicating that although responses to stimulant are influenced by fold changes in input cAMP, it does not necessarily follow the exact FCD notion as introduced previously in chapter 2

To further capture the heterogeneity properties for different background x and fold change F, we generalise as follows. Given two vectors of input background cAMP $\mathbf{x} = (x_i, x_2, \ldots, x_m)$ and corresponding fold change $\mathbf{F} = (F_1, F_2, \ldots, F_n)$ with x_i and F_j denoting the elements of each input vector, the set of all possible combination of input x_i and F_j is denoted as

$$S = \{(x_i, F_j) : i = 1, \ldots, m \quad j = 1, \ldots, n\} \tag{4.1}$$

where we set the background cAMP x to take positive integer values $x_i \in \mathbb{Z}^+$ and $F_j \geq 2$. We denote the distribution of I_p responses resulted from stimulating 1000 virtual cells to a specific pair of input (x_i, F_j) as $I_p^{x_i, F_j}$. The input range of interest is $\mathbf{x} = (1, 2, \ldots, 100)$ and $\mathbf{F} = (2, 2.1, \ldots, 100)$ encompassing the range of experiment data in Fig 4.1C and we denote the resulting set of interest as S_0. However, to derive I_p responses for all pair of input intervals within this range by numerically solving model ODEs as described previously is computationally expensive. Hence we adapt an approximation method, generally described as first modelling the distribution of I_p responses to a sparse range of

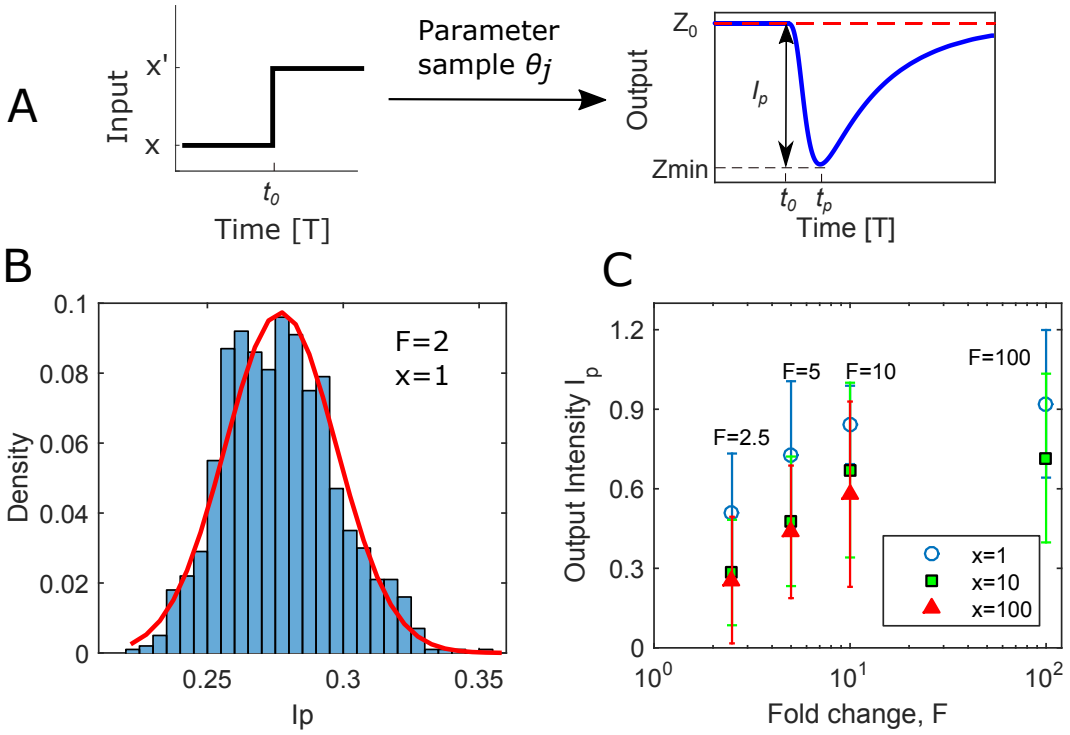

Figure 4.1: Emulation of cell-cell variability. (A) Response to step input x, x' derived by numerically solving model ODEs with parameter θ_i. I_p and t_p are the values of interest. (B) Histogram of I_p from 1000 θ stimulated with step input $x = 1, x' = 2$. Red curves is the result of fitting lognormal distribution. (C) I_p response to different background cAMP as in the experiment by Takeda et al. (2012) replotted as function of fold change. Error bars in this paper represent standard deviation

inputs and then use the model parameters to estimate $I_p^{x_i,F_j}$ for any (x_i, F_j) of interest. Here we choose the sparse range of inputs to be $\mathbf{x} = (1, 2, \ldots, 10, 20, \ldots, 100)$ and $\mathbf{F} = (2, 3, \ldots, 10, 20, \ldots, 100)$. The length of input vectors then becomes $m = 19$ and $n = 18$ for $\mathbf{x}$ and $\mathbf{F}$ and the resulting set is denoted as S_1. We derive numerically $I_p^{x_i,F_j}$ for each input pair (x_i, F_j) in our new set $S_1 : S_1 \subseteq S_0$. We model all responses $I_p^{x_i,F_j}$ from stimulating inputs in set S_1 with the lognormal distribution where the probability density function given as

$$f(I_p^{x_i,F_j}) = \frac{1}{I_p^{x_i,F_j}\sigma_{x_i,F_j}\sqrt{2\pi}} \exp\left(-\frac{(\ln I_p^{x_i,F_j} - \widetilde{I}_p^{\,x_i,F_j})^2}{2\sigma_{x_i,F_j}^2}\right) \tag{4.2}$$

is then fitted to each histogram of $I_p^{x_i,F_j}$ and we estimate the mean $\widetilde{I}_p^{\,x_i,F_j}$ and standard deviation σ_{x_i,F_j}. The results of fitting a distribution to histogram of $I_p^{x_1,F_1}$ where $x_1 = 1$ and $F_1 = 2$ is shown in Fig 4.1B as a red curve. To illustrate how background cAMP affects the mean and standard deviation of the responses, we plotted $\widetilde{I}_p^{\,x_i,F_j}$ and σ_{x_i,F_j} as coloured dots for all $x_i, i = 1, \ldots, m$ with a subrange fold $F = (2, 5, 10, 30, 100)$ in the left most panels of Fig 4.2A,B . Initial inspection suggests that in the presence of high

background cAMP, the average cell response to stimulant cAMP is weaker and that the responses are more varied. We further fit curves of $\widetilde{I}_p^{F_j}$ and σ_{F_j} for all $j = 1, \ldots, n$ with a quadratic function as

$$\widetilde{I}_p^{F_j} = a_1^{F_j} x^2 + b_1^{F_j} x + c_1^{F_j} \tag{4.3}$$

$$\sigma_{F_j} = a_2^{F_j} x^2 + b_2^{F_j} x + c_2^{F_j} \tag{4.4}$$

and estimated function parameters $a_k^{F_j}, b_k^{F_j}, c_k^{F_j}$ where $k = 1, 2$. The result of the estimated parameters are plotted as black dots in the three right most panels of Figure 4.2A,B. Coloured curves of left most panels in Figure 4.2A,B represent quadratic functions fitted to the estimated parameters of the lognormal distribution. The curves of quadratic parameters a_1, b_1, c_1, c_2 are then fitted using a hyperbolic, logarithmic or exponential function where the results of the estimated coefficients are summarised in table 4.1 while points of a_2 and b_2 were linearly interpolated.

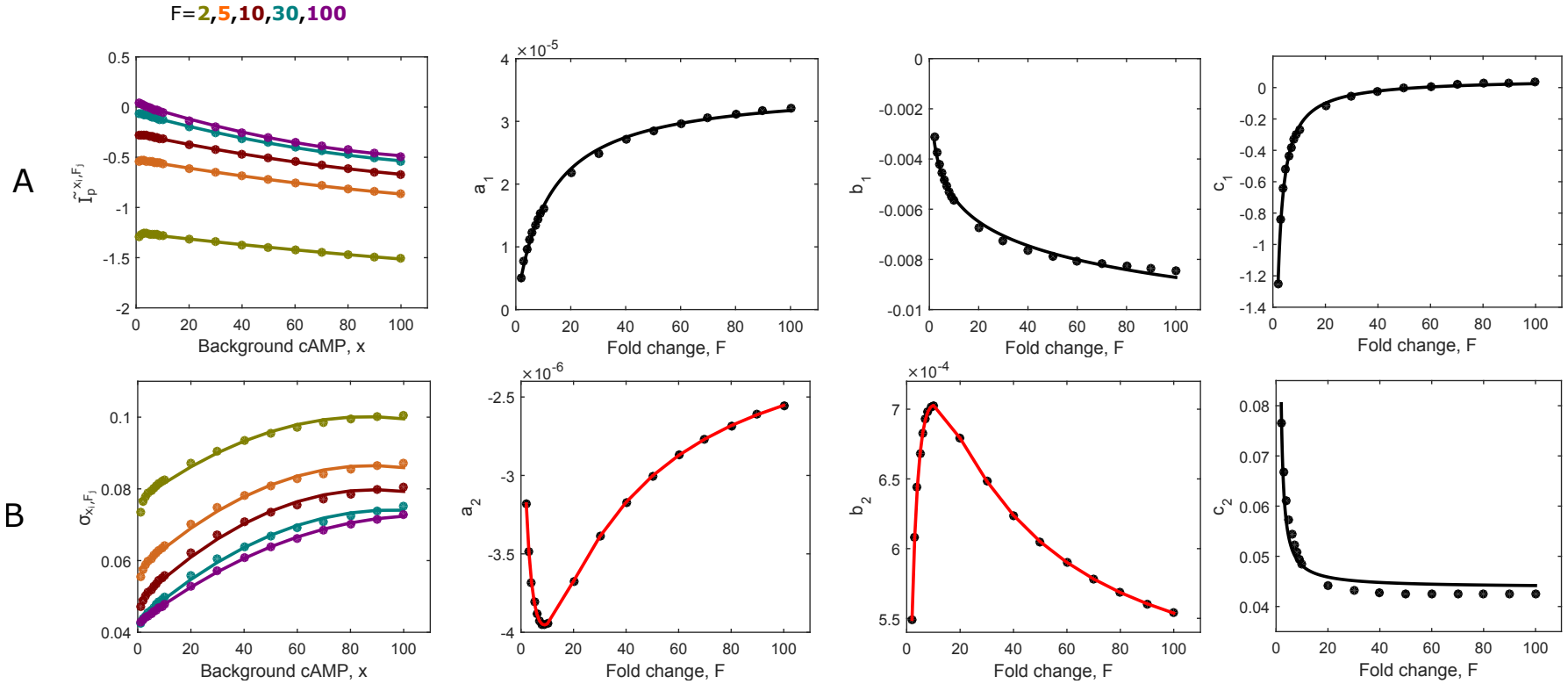

Figure 4.2: Estimated parameters and coefficients. (A,B Most Left Panel) The estimated parameters of lognormal distributions fitted to histogram of responses shown for fold $F = 2, 5, 10, 30, 100$ as coloured dots. Coloured curves are quadratic functions fitted to the estimated parameters. (A, Right Panels) Estimated parameters of the quadratic functions fitted to the lognormal parameter $\widetilde{I}_p$ curve shown as black dots. Black lines are results of functions in table 4.1 fitted to the estimated parameters. (B, Right Panels) Estimated parameters of the quadratic functions fitted to the lognormal parameter σ curve shown as black dots. Black lines are results of function in table 4.1 fitted to the estimated parameter. Red lines are linearly interpolated points.

Table 4.1: Quadratic parameter curves fitted with various functions

Parameter	Functional form	Estimated Coefficients
a_1	$a_1 = \frac{\alpha F}{\beta + F}$	$\alpha = 3.54 \times 10^{-5}, \beta = 11.591$
b_1	$b_1 = \alpha + \beta \log(F)$	$\alpha = -2.4 \times 10^{-3}, \beta = -1.4 \times 10^{-3}$
c_1	$c_1 = \frac{\alpha}{\beta + \gamma e^{\tau F}} + \epsilon$	$\alpha = 3.28 \times 10^{-4}, \beta, \gamma = 0.109$
		$\tau = 9.424 \times 10^{-4}, \epsilon = 0.0556$
c_2	$c_2 = \frac{\alpha F}{\beta + F}$	$\alpha = 0.044, \beta = -0.911$

Hence with the estimated coefficients and quadratic parameters we can inversely approximate the parameters of the lognormal distribution $\widetilde{I_p}^{x_i,F_j}$ and σ_{x_i,F_j} for any pair of (x_i, F_j) within our set of interest S_0 by solving the quadratic equation

$$\widetilde{I_p}^{x_i,F_j} = a_1^{F_j} x_i^2 + b_1^{F_j} x_i + c_1^{F_j} \tag{4.5}$$

$$\sigma_{x_i,F_j} = a_2^{F_j} x_i^2 + b_2^{F_j} x_i + c_2^{F_j} \tag{4.6}$$

Additionally, we can now sample a single cell response to stimulant cAMP with background x_i and fold change F_j denoted as R_{x_i,F_j} drawn from the lognormal distribution as $R_{x_i,F_j} \sim \ln\mathcal{N}(\widetilde{I_p}^{x_i,F_j}, \sigma_{x_i,F_j})$ without the need to solve model ODEs.

4.3 Effect of background cAMP on FCD accuracy

Among the criteria for exact FCD is the sameness of output to the same fold input regardless of the background input. One logical way to asses the accuracy of the fold change detected is by benchmarking responses to a known true value. However, we do not know what is the true response value a cell should produce when stimulated with a specific step input. Therefore we can only estimate the accuracy of FCD by looking at the variance of response. The assumption here is that the less varied the responses are, the more the cells agrees to the value of FCD each of them are sensing. Hence, the variability in responses tells us how consistently cells sense the fold change in stimulant cAMP (FCD).

In this section we analyse the effect of background cAMP on response I_p. We ask what are the average responses to different background camp x and fold change F and more importantly how do responses vary? We introduce a new range of input vectors $\mathbf{x} = (1, \ldots, 100)$ and $\mathbf{F} = (2, 2.1, \ldots, 10)$ with resulting set $S_2 : S_2 \subseteq S_0$. This is in line with results by Kamino et al. (2017) where FCD behaviour is observed when *Dictyostelium* cells in background cAMP $x = 0.1 \sim 10$ nM were stimulated with cAMP of fold change $F = 10$. Furthermore experiment results by Takeda et al. (2012) as

in Figure 4.1C shows that responses are linear between $F = 2 \sim 10$ but saturate for $F \geq 10$ suggesting that FCD mechanism is more likely to occur in the linear regime. We compute $\widetilde{I}_p^{x_i,F_j}$ and σ_{x_i,F_j} for $(x_i, F_j) \in S_2$ using equation 4.5,4.6 and the results are shown in Figure 4.3. Cross sections of Figure 4.3A and Figure 4.3C for fold change $F = 2$ and $F = 10$ are shown as Figure 4.3B and Figure 4.3D. Figure 4.3A,B shows that in a higher background concentration of cAMP x, we can expect that cells on average have weaker responses as indicated by the linearly decreasing response $\widetilde{I}_p^{x_i,F_j}$ with background x. There is also more variability in the responses produced, as shown by the linear increase in the standard deviation σ_{x_i,F_j} at first followed by its saturation around x =50 nM. Therefore in high background cAMP, the population of cells is less confident on the fold change that is being detected indicated by the high variability in responses produced.

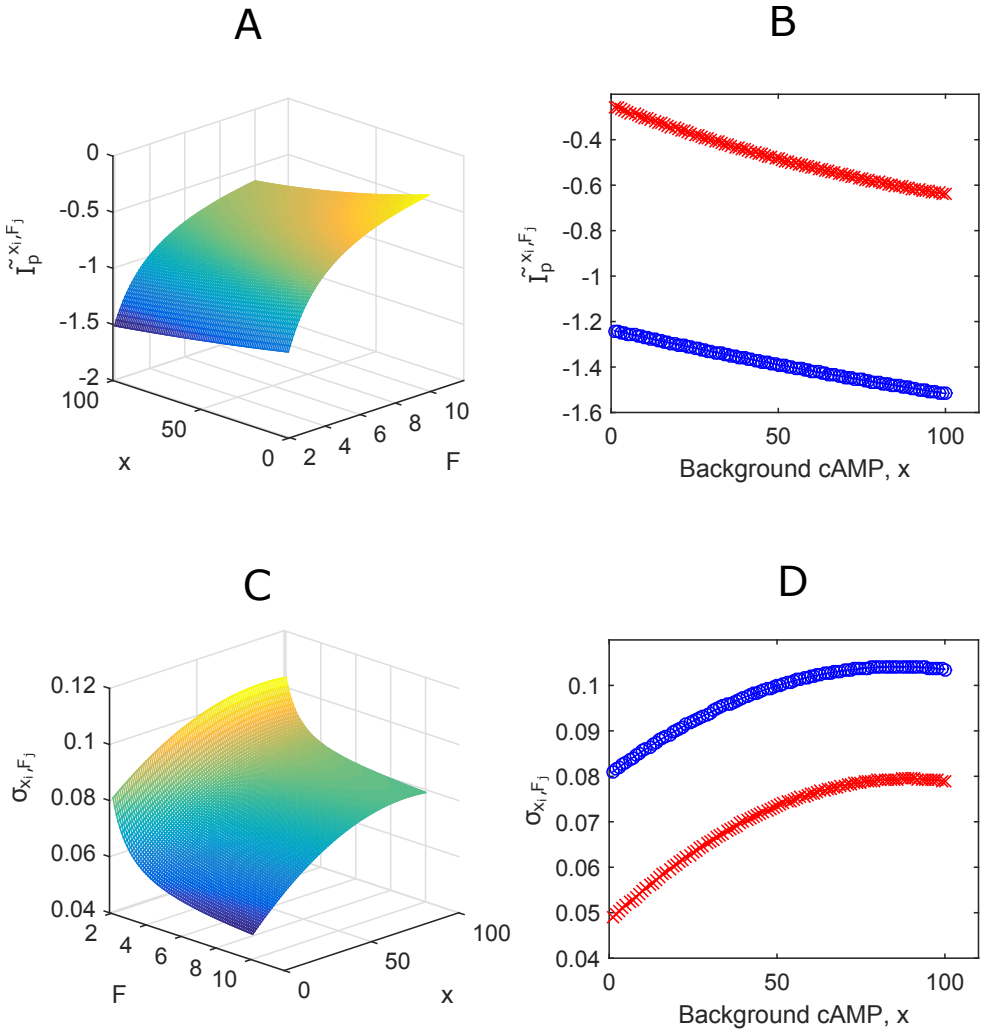

Figure 4.3: Responses for background cAMP $\mathbf{x} = (1, 2, \ldots, 100)$ and fold change $\mathbf{F} = (2, 2.1, \ldots, 10)$. (A) Mean of responses $\widetilde{I}_p^{x_i,F_j}$ in log space. (B) Cross section sample of mean of $\widetilde{I}_p$ for fold $F = 2$ (blue circles) and $F = 10$ (red crosses). (C) Standard deviation of responses σ_{x_i,F_j} . (D) Cross section sample of standard deviation for fold $F = 2$ (blue circles) and $F = 10$ (red crosses).

4.3.1 Responses are more consistent for lower fold change

We have seen how for responses to a fixed fold change in input, the modelled lognormal distribution shape and scale changes with different background cAMP. How can we model responses without the stratification by background input? In order to do this we first derive a distribution that comprises of responses from multiple background cAMP to the same fold change in input. Focussing only on responses from our range of background cAMP $\mathbf{x} = (1, 2, \ldots, 100)$, it is assumed that any background within this range is equally likely.

Algorithm 1 Generating responses across background x

Initialize $\mathbf{F}$
for all $F_j \in \mathbf{F}$ **do**
    Initialize background sample $\bar{\mathbf{x}}_{\mathbf{F_j}} = (x_1, \ldots, x_M)$
    for $i = 1$ to M **do**
        Sample background $x_i \sim U(1, 100)$
        Compute lognormal parameters for x_i,
        $\widetilde{I_p}^{x_i,F_j} = a_1^{F_j} x^2 + b_1^{F_j} x + c_1^{F_j}$
        $\sigma_{x_i,F_j} = a_2^{F_j} x_i^2 + b_2^{F_j} x_i + c_2^{F_j}$
        Sample response $R_{x_i,F_j} \sim \ln N(\widetilde{I_p}^{x_i,F_j}, \sigma_{x_i,F_j})$
    end for
end for

To derive responses to fold change F_j in stimulant cAMP across all background x, we first create samples of background cAMP $\bar{\mathbf{x}}_{F_j} = (x_1, \ldots, x_M)$ with size $M = 10,000$ where each x_i is drawn randomly from a discrete uniform distribution $x_i \sim U(1, 100), x_i \in \bar{\mathbf{x}}_{F_j}$. From these samples, we generate responses using the lognormal distribution properties described by Algorithm 1. The result is such that for each fold F_j there are M responses R_{x_i,F_j} denoted as $I_p^{F_j}$.

The results of generating responses $I_p^{F_1}$ for fold change $(F_1 = 2)$ and $I_p^{F_{81}}, (F_{81} = 10)$ are visualized as histograms normalized as probability in Figure 4.4A. We plotted the probability values of the bin which contains histogram mean $\mu_p^{F_j}$ for each fold F_j as Figure 4.4B. To get a full view of how distribution characteristics changes, each histogram's mean, $< I_p^{F_j} >$ and standard deviation, s_{F_j} are plotted as Figure 4.4C,D. We found that the average responses are less likely to be seen when cells are stimulated with larger fold change in cAMP (Figure 4.4B). It is also observed in Figure 4.4C,D that as fold change in input becomes larger, both mean response μ_{F_j} and standard deviation increases, signalling on average a stronger response is expected but the responses themselves being less similar. The shape of the distribution changes such that in Figure 4.4A as the fold change F_j increases, the response R_{x_i,F_j} increases and shifts to the right while the distribution becomes wider. As there is reduced variability in responses to large fold change in input it can be concluded that cells stimulated with smaller fold change in cAMP are likelier to be more consistent in their responses.

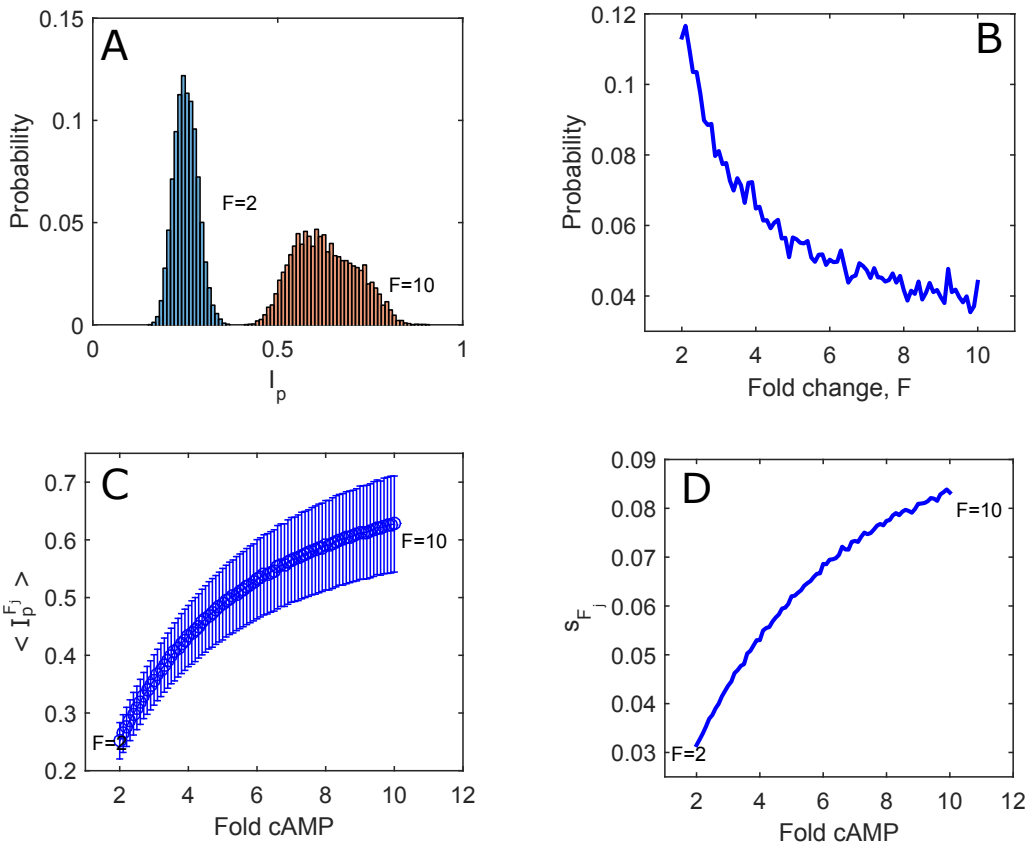

Figure 4.4: Response I_p distribution statistics with background cAMP $x = 1, .., 100$ and input cAMP x' corresponding to fold $F = 2, 2.1.., 10$ (interval 0.1) considered. (A) A sample of output distribution for $F = 2$ and $F = 10$ plotted as histogram and normalized as probability. Each bin represents a range of response values and is assigned a probability value based on the sample size. (B) The relation between mean of each output distribution and their probability. (C) Mean of distributions $< I_p^{F_j} >$ with standard deviations s_{F_j} represented as error bars. (D) Standard deviation is larger as fold cAMP increases.

4.4 Fold Change Distinguishability

The distribution of responses and their properties derived previously in Figure 4.4 provides further information that there are overlapping distributions. Recall from chapter 2 that one condition required for exact FCD is to have distinct responses to different fold change in input. Distributions that overlap indicate that some cells are 'confused' and unable distinguish sensing between two different fold changes in input. As illustrated by the green shaded area in Figure 4.5, some responses to fold change in stimulant $F = 2$ can be misclassified as responses derived from $F = 3$. The overlapping area represents the amount of fold change misclassification (either false positive or false negative) between responses of two different fold inputs.

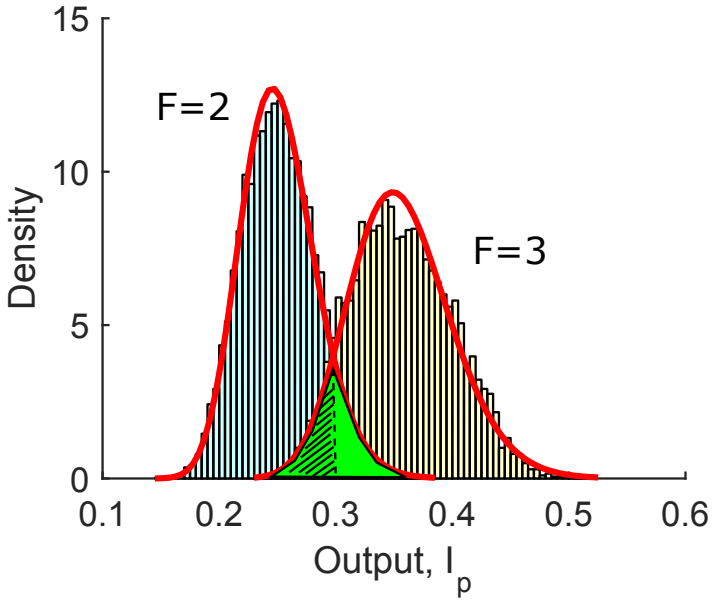

Figure 4.5: Two distributions of responses for $F = 2$ and $F = 3$ fitted with log-normal distributions with overlap areas in green. Shaded area in green indicates responses for fold change $F = 3$ misclassified as responses to $F = 2$

We investigate this 'fold distinguishability' property where we ask what is the fold-distance limit two fold change in stimulant denoted as F_x and F_y must have so that cell responses are minimally distinguishable? It is assumed the responses $I_p^{F_j}$ for fold $F_j \in \mathbf{F}$ derived in the previous section are also distributed log-normally with mean μ_{F_j} and variance $\sigma_{F_j}^2$ denoted as $I_p^{F_j} \sim \ln\mathcal{N}(\mu_{F_j}, \sigma_{F_j}^2)$. The probability density function of the log-normal distribution is then fitted to histogram of $I_p^{F_j}$ for all $F_j \in \mathbf{F}$ derived previously such that

$$f(I_p^{F_j}) = \frac{1}{I_p^{F_j}\sigma_{F_j}\sqrt{2\pi}} \exp\left(-\frac{(\ln I_p^{F_j} - \mu_{F_j})^2}{2\sigma_{F_j}^2}\right) \tag{4.7}$$

The overlapping area $A^{F[x,y]}$ between two fold F_x and F_y is then computed by integration as

$$A^{F[x,y]} = \int_a^b f(I_p^{F_y}) dI_p^{F_y} + \int_b^c f(I_p^{F_x}) dI_p^{F_x} \tag{4.8}$$

where b is the intersection of the two lognormal distributions, a, c are the minimum and maximum horizontal values of the overlapped area. Here mean μ_{F_j} of one lognormal distribution is assumed greater such that $\mu_{F_y} > \mu_{F_x}$. We compared and calculated the overlapping area for fold $F[x, y]$ where $x, y = 2.0, 2.1, \ldots, 10$. The result is a matrix of overlapped areas $\mathbf{A}$ such that

$$\mathbf{A} = \begin{bmatrix} A^{F[2,2]} & A^{F[2,2.1]} & \dots & A^{F[2,10]} \\ A^{F[2.1,2]} & A^{F[2.1,2.1]} & \dots & A^{F[2.1,10]} \\ \vdots & \vdots & \ddots & \vdots \\ A^{F[10,2]} & A^{F[10,2.1]} & \dots & A^{F[10,10]} \end{bmatrix} \tag{4.9}$$

where the diagonal elements are identical distributions completely overlapping each other. The computed result of matrix $\mathbf{A}$ is visualized in Figure 4.6. Fold changes in cAMP F_x and F_y are only considered distinguishable if the overlapping area of their response distributions is less than or equal to some threshold or decision boundary r. Here r is arbitrarily selected as 40% of the overlapping area and shown as red curves in Figure 4.6. This means that if the overlapping area between two response distributions of fold changes F_x and F_y is more than 40% then the changes in input concentrations of cAMP are perceived as indistinguishable. Therefore the two red curves divides between the region of distinguishability and indistinguishability.

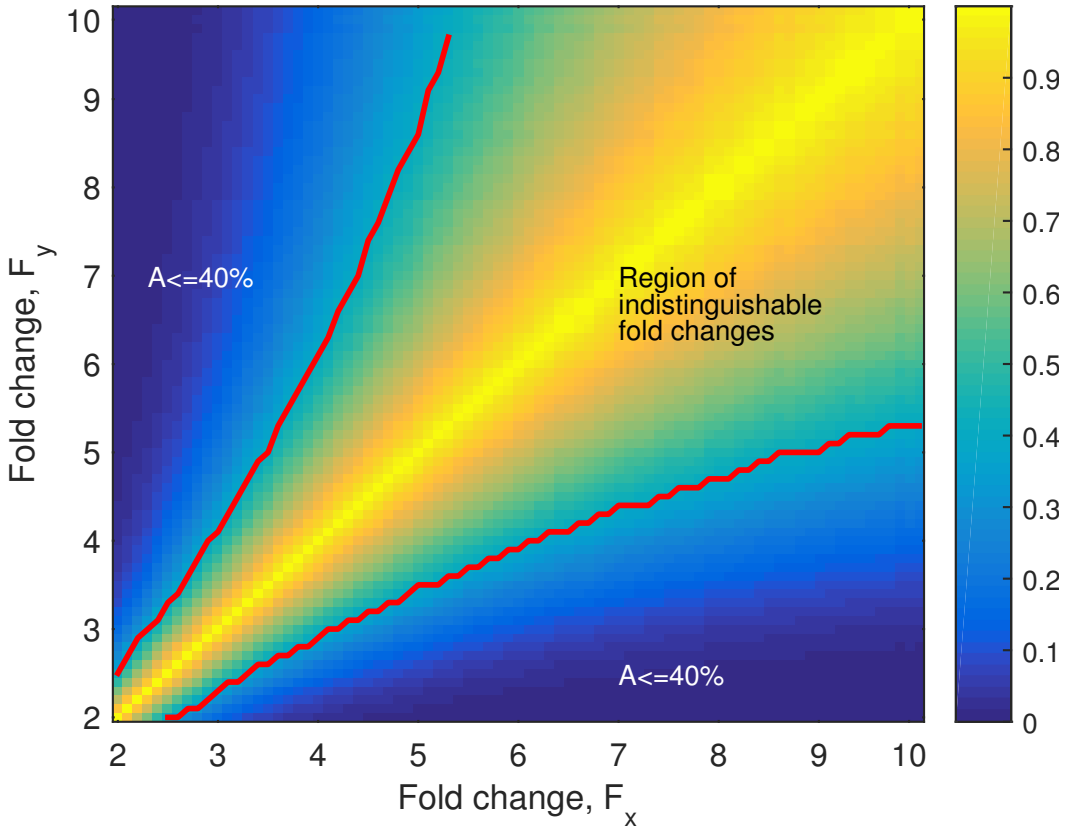

Figure 4.6: Overlapped area A for two fold F_x and F_y compared with $x, y = 2, 2.1, .., 10$. The overlapped area $A = 1$ for two distributions completely overlapping each other and $A = 0$ for the two distribution are completely separated (no-overlap). Red curves divides between distinguishable and indistinguishable region.

From Figure 4.6, it can be said that for example, that a fold change of magnitude F_3 is only considered distinguishable from fold $F_{4.1}$ and larger or with $F_{2.2}$ and smaller. Therefore the region of indistinguishability for fold F_3 is $F_{2.2} < F_3 < F_{4.1}$. If distance of distinguishability d_f is calculated, then it can be seen that F_3 needs only fold distance $d_f = 0.8$ with smaller input fold changes compared to $d_f = 1.5$ with larger F. This trend is evident across all fold changes in input and therefore it can be concluded that a lower input fold change is more distinguishable than a larger one.

4.5 Hyperbolic model of input-output relation

As stated before, the architecture of the mathematical model used to describe the interaction of proteins in the signalling pathway of *Dictyostelium* analysed in this thesis is an instantiation of the incoherent feed forward loop (IFFL) network (Takeda et al., 2012). Theoretical analysis have shown that the input-output relation that arises from a system incorporated with IFFL in its design in some limiting condition is best described by a logarithmic function (Adler et al., 2014). The logarithmic law is commonly found in many sensory systems, from discriminating visuals to how monkeys or native humans count (Dehaene, 2003; Dehaene et al., 2008). The relationship between ligand concentration and kinase activity in the *E.coli* chemotaxis is also found to obey by the same law (Tu et al., 2008). The logarithmic function used to describe the relation between *Dictyostelium* cell responses I_p to fold change in stimulant cAMP F introduced in Adler et al. (2014) is given as $I_p = \alpha \log(F) + b$ and yielded a better Mean Squared Weighted Deviation (MSWD) score than variation of power functions (Adler et al., 2014). This implies that as the intensity of the fold input increases, the difference in peak response must be higher for responses to be distinguishable, a key element of the Weber-Fechner law. The functions evaluated was fitted to eleven experiment data points in Figure 4.1C.

Here we revisit the input-output relation by approximating extra data points to yield a more accurate and confident estimation of the non-linear relationship. We generate previously unseen distribution of responses $I_p^{F_j}$ for all fold change of F_j in the range $\mathbf{F} = (2, 3, \ldots, 10, 20, \ldots, 100)$ by utilising the process described in Algorithm 1. Intervals of the simulated responses was taken such that the data spreads well across two magnitudes of fold change to avoid over-fitting in certain regimes. The results are shown in Figure 4.7 as blue boxplots plotted together with experiment data by Takeda et al. (2012) replotted as black circles and black lines. The trajectory of our simulated data displays saturation as distribution of responses to fold change within the range $F = 20 \sim F = 100$ becomes more similar. To capture the saturation behaviour we fitted to the mean of the simulated data a hyperbolic expression of the Michaelis-Menten type used to model enzyme kinetics given as

$$I_p = I_{max}\frac{F}{K_m + F} \tag{4.10}$$

where I_{max} is the system's maximum response rate and constant K_m is the saturating concentration. When fold change in input F is small such that $F \ll K_m$, the system displays a linear response where $I_p \approx I_{max}F/K_m$. When fold input is large enough such that $F \gg K_m$, the response saturates to $I_p \approx I_{max}$.

For comparison purposes, the logarithmic function of $I_p = \alpha \log(F) + b$ is re-fitted to the experimental data as done by Adler et al. (2014). Both function fitting of the hyperbolic and logarithmic function were done using the 'nlinfit' function of MATLAB. The results of fitting both hyperbolic and logarithmic functions are shown as blue and green lines respectively in Figure 4.7 with estimated coefficients I_{max}, K_m, α, d described in the figure caption.

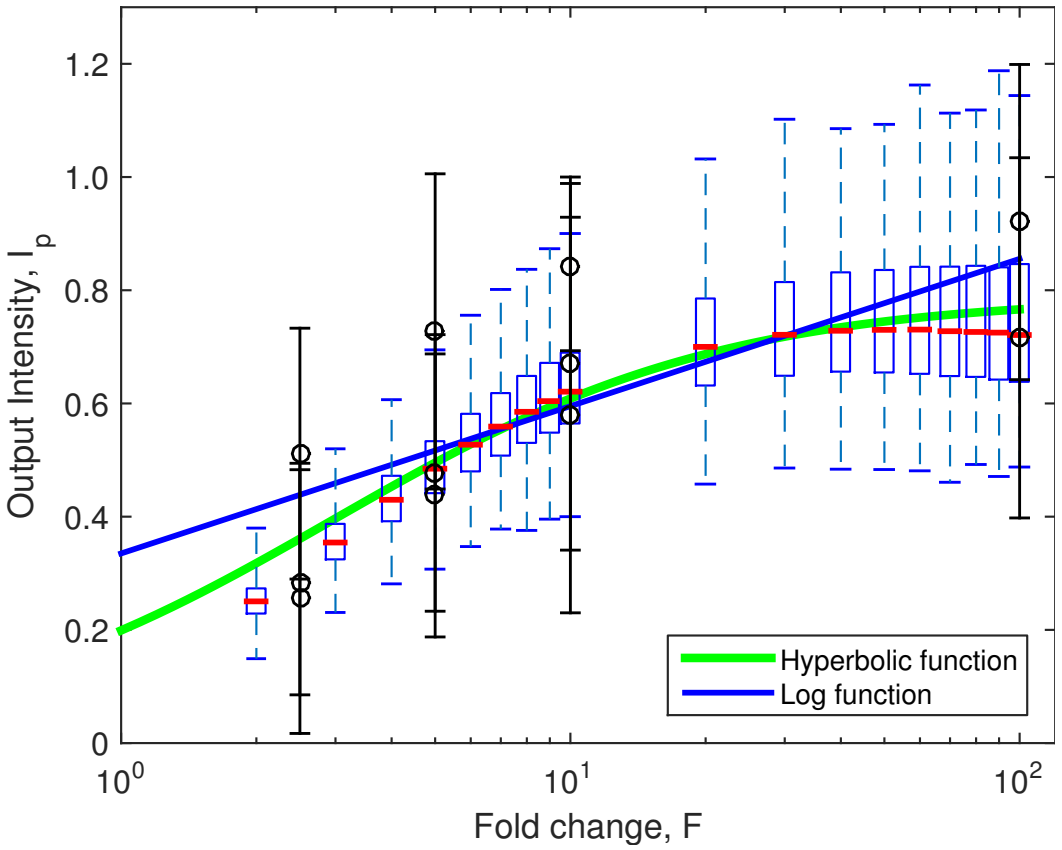

Figure 4.7: Describing Input-Output relation with simulated data. Black circles and vertical lines indicates the experiment and standard deviation data derived from Takeda et al. Blue boxplots is the simulated data used for non-linear fitting. For Adler's $I(x) = \alpha \log(x) + b$ equation, the nonlinear fit resulted in $\alpha = 0.0956$ and $d = 0.3571$. For Michaelis-Menten equation, the fit to the mean of the simulated data resulted in $I_{max} = 0.7889$ and exponent $K_m = 2.9638$. Functions fitted to experiment data is not plotted. Refer to table 4.2 for goodness of fit.

Table 4.2: Mean square weighted deviation (MSWD) for Logarithmic and Hyperbolic functions fitted to simulated (train) and experiment (test) data. A smaller value indicates a better fit.

Equation	Simulated	Experiment
$I_p(F) = I_{max}F/(K_m + F)$	0.0119	0.0889
$I_p(F) = \alpha log(F) + b$		0.0996

If our simulated data derived from model ODEs approximate the experiment data well, then we would expect that the hyperbolic function (where its coefficients are derived by fitting to the simulated data) when evaluated with the experiment data to perform as well if not better than the logarithmic function suggested by Adler et al. (2014). Thus in this setting, the hyperbolic function is 'trained' with our simulated data but 'tested' with the experiment data by Takeda et al. (2012). We evaluated the goodness of fit by computing the Mean Square Weighted Deviation (MSWD) score given below for both functions. The MSWD equation is given as

$$MSWD = \frac{1}{n-1}\sum_{i=1}^{n}\left(\frac{\hat{y}_i - y_i}{\sigma_i}\right)^2 \tag{4.11}$$

where n is the number of data points, $\hat{y}_i$ and y_i are the estimated response of the hyperbolic function and experiment data at fold F_i respectively, $(\hat{y}_i - y_i)^2$ is the residual for ith data and σ_i is the standard deviation of the simulated data or error bar of the experiment data. The results are summarised in table 4.2 and shows that the hyperbolic function helped by its saturating nature for increase input has a better fit than logarithmic function when evaluated against experiment data even though it is trained with the simulated data. This result underlines two important conclusions. First is that the hyperbolic function is a better description of the experiment data by Takeda et al. (2012) than the logarithmic function. In fact, the hyperbolic function also describes the simulated data better where the logarithmic function yielded $MSWD = 0.0810$ when evaluated against the simulated data. This result is intentionally not shown in table 4.2 for clarity purposes. Second this implies that the prediction given by the simulated data to unobserved inputs is sensible and provides additional evidence that the model ODEs suggested by Takeda et al. (2012) describes the dynamics of the experiment well.

4.6 Log-Normal model of the distribution of responses

4.6.1 Motivation

A major assumption in our approximation is that responses generated by the model ODEs using the estimated 1000 sets of parameters is distributed log-normally. This assumption applies to the distribution of responses generated with or without background dependencies. There are many density functions other than the log-normal that can characterize the positive skewness observed in the distribution of responses. However, the choice of the log-normal is based on the numerosity encoding hypothesis suggested by studies from the field of cognitive neuroscience. Such studies examine how humans and nonhumans primate encode numerosity such as how well can subjects identify and distinguish the same or different number of dots. Two main encoding hypotheses, a linear and non linear has been suggested although whether the encoding is instantiated linearly or non-linearly remains a disputed subject. Examples are the studies by Dehaene (2001); Brannon et al. (2001) and Nieder and Miller (2003) where numerosity encoding by pigeons and monkeys is investigated through sets of tasks that each subject has to complete. While Dehaene (2001) and Brannon et al. (2001) suggested a linear encoding scheme for pigeons, Nieder and Miller (2003) argued that the logarithmic compression hypothesis better describes the neural representation of numerosity in monkeys.

In the context of this thesis, the sensing of the abundancy of molecules cAMP by *Dictyostelium* cells is similar to the identification of numerosity of dots by monkeys as observed in the experiment by Nieder and Miller (2003). We noticed that FCD shares the same properties with the logarithmic encoding hypothesis. It is important to note the difference between logarithmic response to stimulus in the previous section and the logarithmic encoding hypothesis in this section which looks at the underlying distribution of (logarithmic) responses. Detection of fold, represented through sensory variable I_p, is much more certain in the region of lower fold. This is similar to the certainty in identifying lower number of dots by monkeys in the experiment by Nieder and Miller (2003). However, as the number of dots increases, monkeys tend to make more mistakes in identifying the exact numerosity and the distribution of uncertainties is more asymmetric with a shallower slope towards higher numerosity. These characteristics are also observed in the distribution of responses generated from our model ODEs and estimated parameters, hence suggesting that the FCD sensed is also logarithmically encoded in the sensory representations.

4.6.2 Logarithmic vs Linear Encoding Hypothesis

To evaluate which coding scheme better describes the distribution of responses, we fitted the probability density function of the Log-Normal and Normal distribution to

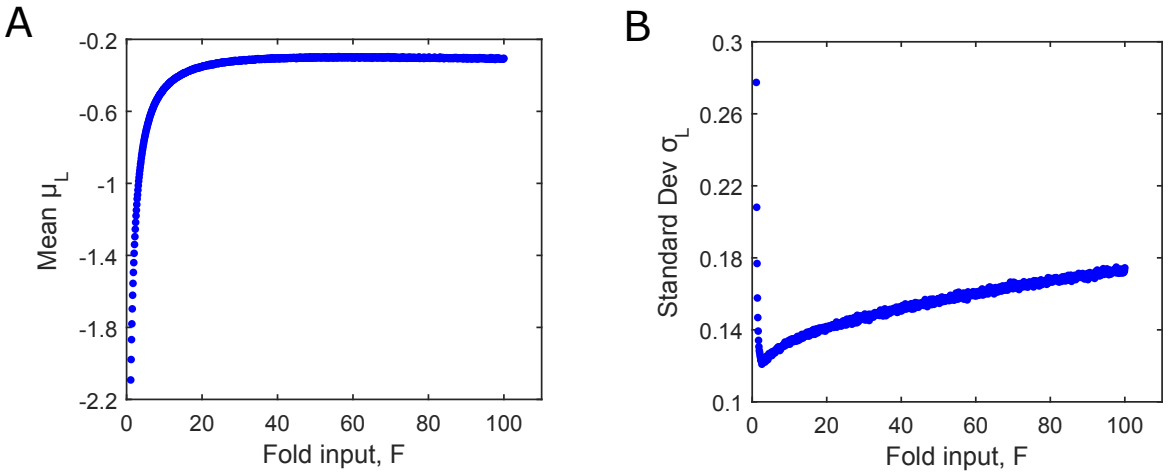

Figure 4.8: Estimated parameters of the fitted log-normal to distribution of I_p responses.

the distributions of I_p responses stimulated by fold inputs $F_j \in \mathbf{F} = (1.1, 1.2, , \ldots, 100)$ independent of background cAMP. The log-normal density function is given by equation 4.7 and the density function for the normal distribution is defined as

$$f_N(I_p^{F_j}) = \frac{1}{\sqrt{2\pi\sigma_N^2}} \exp\left(-\frac{1}{2\sigma_N^2}(I_p^{F_j} - \mu_N^{F_j})^2\right) \tag{4.12}$$

The estimated means and standard deviations for the normal and log-normal distributions are denoted as μ_N, σ_N and μ_L, σ_L respectively. The estimated μ_L, σ_L as a result of the data fitting for the log-normal density function is shown in figure 4.8A,B. A sample result of the distribution fitting for fold $F = 2, 4, 10$ is shown in Figure 4.9. The distribution of responses for a particular fold $F_j \in \mathbf{F}$ consists of 10,000 samples generated using algorithm 1 and are divided into K bins. The goodness of fit for both log-normal or normal density functions to a distribution of responses stimulated by $F_j \in \mathbf{F}$ is then evaluated using the Sum of Squared Residuals (SSR)

$$SSR_{F_j} = \sum_{i=1}^{K} (O_i^{F_j} - f_*(i^{F_j}))^2 \tag{4.13}$$

where $O_i^{F_j}$ is the observed density for bin i and $f_*(i^{F_j})$ is the expected density for bin i computed from the log-normal (equation 4.7) or normal density functions (equation 4.12). The computed result of equation 4.13 for all $F_j \in \mathbf{F}$ is shown in Figure 4.9B. Figure 4.9B shows that for every distribution of responses stimulated by input fold $F_j \in \mathbf{F}$, the log-normal fits better compared to the normal density function. An interesting observation is that the normal density function fits worse for distribution of responses stimulated by lower fold inputs especially in the range of $F_j \leq 2$. Therefore there is a possibility that the right tailness property can also be found in distribution of responses

stimulated even with lower folds. This contrasts with results of Nieder and Miller (2003) where the distribution of uncertainties in numerosity judgement is more symmetric and gaussian like when the monkeys were identifying lower number of dots.

4.6.3 Does *Dictyostelium* cells count as humans or primates count?

Based on the goodness of fit result in Figure 4.9B alone, it is preferable to conclude that the logarithmic compression hypothesis better describes the encoding of FCD by *Dictyostelium* cells. Therefore if we map the uncertainties of *Dictyostelium* cells in sensing fold changes in cAMP concentration, it follows a log-normal model where there is a greater tendency to mis-identify when sensing higher fold change in stimulus. If this conclusion is true, then *Dictyostelium* cells can also be included in the group of species which includes humans and primates that uses the logarithmic encoding scheme or the Approximate Number System (ANS) in counting or sensing physical or abstract representation of numbers. Contrary to other species in the group, the structure of *Dictyostelium* cells are much more primitive governed only by mechanistic bio-chemical reactions and certainly without any central nervous system. Therefore, the conclusion above also implies that in order to achieve ANS, a living organism does not need to be made up of many complex and complicated systems. It is quite likely that there is a simple explanation of this from the appearance of log-normal distributions from geometric means and multiplicative random processes (Mitzenmacher, 2004). However, we do not discuss this further in this thesis.

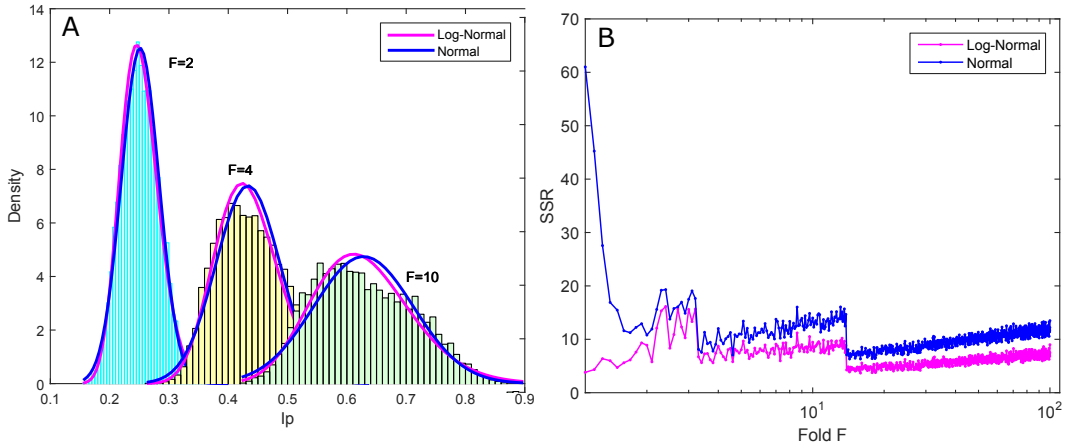

Figure 4.9: (A) I_p distributions of fold $F = 2, 4, 10$ fitted with Normal,and Log Normal distribution. For $F = 2$ the estimated function parameters are $\mu_N = 0.2671, \sigma_N = 0.0367, \mu_L = -1.3291, \sigma_L = 0.1333$. For $F = 4$ the estimated function parameters are $\mu_N = 0.4713, \sigma_N = 0.0653, \mu_L = -0.7614, \sigma_L = 0.1344$. For $F = 10$ the estimated function parameters are $\mu_N = 0.6484, \sigma_N = 0.0953, \mu_L = -0.4437, \sigma_L = 0.1432$. (B) Result of goodness of fit represented as Sum Squared of Residuals (SSR) for each I_p distribution fitted.

4.7 Summary

This chapter mainly provides evidence of the accuracy of FCD in modelled *Dictyostelium* cells examined through the consistency of sensory responses I_p. We introduce quadratic approximations to generate responses given any input in the range of background cAMP $x = 1, \ldots, 100$ and corresponding fold $F = 2, 2.1, \ldots, 100$. The approximation emulates heterogeneity in responses through the estimated posterior parameters. We found that if cells −represented by instantiation of the model ODEs− are stimulated with fold inputs of higher background cAMP, the average responses are weaker but with less variability mostly due to saturation effects. We further generalise the approximation to allow the generation of responses free from background cAMP dependencies. By doing so, we found that responses are more consistent in lower fold change. This implies that the detection of lower fold change is more accurate. We also quantified another measure of FCD which has received little attention in the studies of FCD, the fold distinguishability property. Our analysis revealed that responses to fold changes of lower values are not only more consistent but are also more distinguishable than higher fold changes.

We also proposed a hyperbolic equation to represent the law that governs the input-output relation between sensed fold change and its corresponding sensory responses of I_p. The proposed model further constricts *Dictyostelium* cells responses to increases stimulus as compared to the logarithmic based Weber-Fechner's law as suggested by Adler et al. (2014). Therefore the rate where *Dictyostelium* cells reach the 'feeling of indifferent' when sensing large stimulus is faster than expected. Finally we presented arguments and demonstrated numerically to why the logarithmic compression hypothesis better describes the distribution of responses by the *Dictyostelium* cells to sensed fold changes.

Chapter 5

Inferring posterior probability of fold change

5.1 Introduction

In the previous chapter, the variability of responses is captured by generating I_p values from the 1000 sets of estimated parameters of the model ODEs. The response distribution is then modelled using a log-normal density function which enables us to approximate responses given stimulus without the need to solve the model ODEs. The approach so far has allowed us to quantify the accuracy of FCD indirectly by inspecting the variability of the I_p responses. The primary goal of this chapter is to characterize the posterior probability of fold given observed I_p by using the derived log-normal density function. The modelling of the posterior probability of fold is vital in providing us a direct approach of measuring FCD instead of using an intermediate sensory representation. The inference of posterior probability is executed using Bayes' theorem and therefore an inclusion of a prior knowledge regarding the uncertainty of fold change is necessary. In modelling the posterior we also ask how the prior influences the properties of the posterior. We begin by describing Bayes' theorem and its respective components. We demonstrate how the prior knowledge of fold is modelled from experiments. Lastly we look at how the fold change based on weak and strong background cAMP influences the posterior probability of fold change.

5.2 Bayes' theorem

As shown in the previous chapter, the distribution of responses I_p for a given fold change F independent of background stimulus is modelled using the probability density function (pdf) of the log-normal distribution denoted as

$$f(I_p|F;\mu_L^F,\sigma_L^F) = \frac{1}{I_p\sigma_L^F\sqrt{2\pi}}\exp\left(\frac{-(\ln I_p - \mu_L^F)^2}{2(\sigma_L^F)^2}\right)$$

The pdf is parameterised by the estimated mean μ_L^F and standard deviation σ_L^F shown in Figure 4.8. From here we derive the conditional probability distribution of observing response I_p given that the model is stimulated with input fold F by integration of the pdf as

$$P(I_p|F) = \int f(I_p|F;\mu_L^F,\sigma_L^F)dI_p \tag{5.1}$$

The probability distribution $P(I_p|F)$ represents the conditional probability and is our approximation of the probability of the fluorescent intensity I_p level we would expect to observe when the *Dictyostelium* cells in microfluidic chambers are stimulated with fold change F in input cAMP. This conditional probability $P(I_p|F)$ incorporates the uncertainties in the experiment data through the estimated 1000 sets of ODEs model parameters. We can compute the probability of observing I_p between any intervals α and β given fold change F as $P(\alpha < I_p < \beta|F) = \int_\alpha^\beta f(I_p|F;\mu_L^F,\sigma_L^F)dF$.

Supposed that we have conducted a microfluidic experiment and measured the fluorescent intensity I_p for *Dictyostelium* cells stimulated with an unknown fold change in cAMP. What is the probability that the unknown fold change in cAMP is F given the observed I_p, $P(F|I_p)$? This problem of inferring the state of the environment when we have data from an experiment is solved using Bayes' theorem. The theorem states that the inverse conditional probability or more known as the posterior probability $P(F|I_p)$ is derived as

$$P(F|I_p) = \frac{P(I_p|F)P(F)}{P(I_p)} \tag{5.2}$$

where $P(I_p|F)$ is the already introduced conditional probability and $P(F)$ is the probability of fold change where it represents the *Dictyostelium* cells' own prior knowledge or 'internal belief' on the distribution of fold before sensing molecules of cAMP. Intuitively we would expect that a certain range of fold change is more likely to be encountered in the environment than others. $P(I_p)$ is the marginalized probability defined as

$$P(I_p) = \int_F P(I_p|F)P(F)dF \tag{5.3}$$

and acts as a normalization constant so that integral of the posterior equal one $\int_F P(F|Ip)dF = 1$. As we already have the density function to compute the conditional probability, the key in solving the posterior lies with the modelling of the prior. The rest of this chapter

describes our approach in modelling the prior probability based on existing experiment data and computing the conditional probability. This is followed by computing the marginal $P(I_p)$ and how we put them all together to infer the posterior probability $P(F|I_p)$.

5.3 Modelling the conditional probability

The conditional probability $P(I_p|F)$ is numerically computed as solving it analytically requires the difficult task of finding non-linear functions that best describe the curves of the estimated log-normal distribution parameters in Figure 4.8. We predetermined pairs of discrete values of I_p and F and denote as two vectors $\mathbf{I_p} = (0.1, 0.11, 0.12, \ldots, I_{p,i}, \ldots, 1)$ and $\mathbf{F} = (1.1, 1.2, \ldots, F_j, \ldots, 100)$. The elements of each vector are denoted as $I_{p,i}$ and F_j. The probability of observing $I_{p,i}$ given that the stimulus is F_j is then computed by integration of the density function

$$P(I_{p,i} \in I_{p,i} \pm \delta|F_j) = \int_{I_{p,i}-\delta}^{I_{p,i}+\delta} \frac{1}{I_{p,i}\sigma_L^{Fj}\sqrt{2\pi}} \exp\left(\frac{-(\ln I_{p,i} - \mu_L^{F_j})^2}{2(\sigma_L^{Fj})^2}\right) dI_p \tag{5.4}$$

where $P(I_{p,i} \in I_{p,i} \pm \delta|F_j)$ indicates the probability of observing $I_{p,i}$ in the range of $I_{p,i} - \delta$ and $I_{p,i} + \delta$. Hereafter $P(I_{p,i} \in I_{p,i} \pm \delta|F_j)$ is referred as $P(I_{p,i}|F_j)$ for brevity. The interval δ is chosen such that the sum of the computed conditional probability equal one, $\sum_{I_p=0.1}^{1} P(I_{p,i}|F_j) = 1, \forall F_j \in \mathbf{F}$. We then solve for the conditional probability for all possible combinations of $I_{p,i}$ and F_j. The result of the computation for selected I_p and F is shown in Figure 5.1. For the purpose of analysis we define $F \leq 10$ as low fold region and $F > 10$ as high fold region. From Figure 5.1 it is more likely that we observe low I_p when the *Dictyostelium* cells are stimulated with low fold than observing high I_p caused by higher F [1] . The conditional probability of observing a low I_p given low fold is significant only for a small range of I_p. For example, $P(I_p|F = 2)$ is only significant for I_p in the range of $I_p = 0.15 \sim 0.36$.

Due to saturation, stimulating cells beyond $F = 20$ does not increase the chances of observing a higher I_p. A positive skewness can be seen for distributions of observed I_p stimulated with large F. The saturation of estimated mean μ_L for fold $F > 20$ as in Figure 4.8 ensures that within this range, the $P(I_p|F)$ does not have significant support along the I_p axis.

[1] Note that I_p responses are normalized as described in chapter 4. Therefore observing low I_p translates into observing a high fluorescent intensity distributed uniformly across the cell.

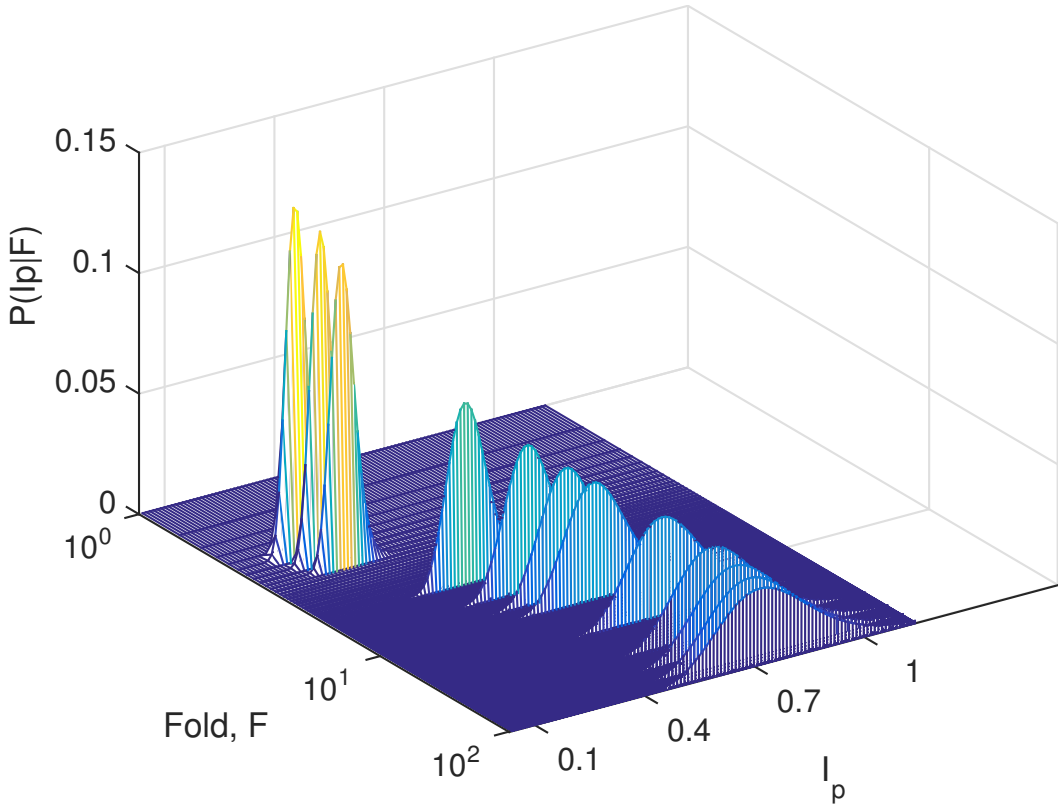

Figure 5.1: The conditional probability; the probability of observing I_p values given measured fold change in cAMP F, $P(I_p|F)$. Results are shown for $F = 1.6, 1.8, 2, 4, 6, 8, 10, 20, 40, 60, 80, 100$. The Fold F axis is set in log scale for readability purposes.

5.4 Modelling prior fold based on experiment

In this section our goal is to extract what the internal belief of fold change is by looking at the response of the cells to artificial gradients. We model the prior $P(F)$ by using information on cell movements measured experimentally by Amselem et al. (2012) in the study of *Dictyostelium* chemotaxis. *Dictyostelium* cells' directional responses to a gradient of chemoattractant is quantified by the chemotactic index which is the distance travelled in the direction of gradient divided by the total distance travelled by a population of cells (Skoge et al., 2010). Alternatively one might also track their motility in terms of velocity and angle in microfluidic devices (Song et al., 2006; Meier et al., 2011).

Amselem et al. (2012) generated a stable linear gradient in a microfluidic chamber containing a population of *Dictyostelium* cells. The direction of the gradient is one dimensional as illustrated in Figure 5.2A. Concentration is strongest at one end of the chamber at location $x = x_0$ while cAMP is zero at the opposite end at $x = L$. Figure 5.2B illustrates the cAMP concentration profile in the microfluidic chamber. Each cells were then tracked by microscopic imaging and the velocity and angle of movements were recorded. The distribution of velocity v and angle φ recorded by Amselem et al. (2012)

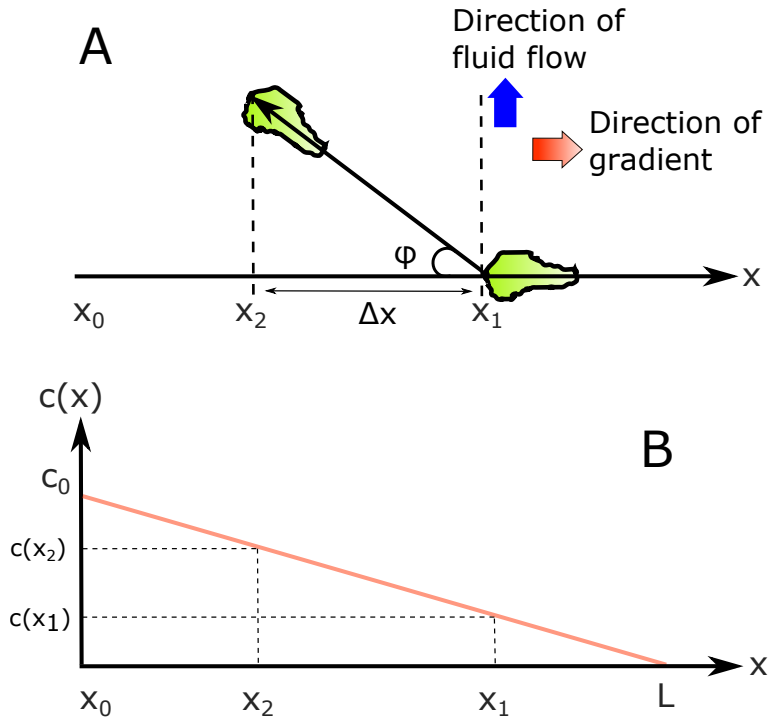

Figure 5.2: (A)Illustration of a single cell chemotaxis in the stable gradient microfluidic chamber as reported in the experiment by Amselem et al. (2012). The corresponding coordinate system is also defined. cAMP concentration is strongest at x_0. (B) cAMP concentration in the microfluidic chamber is modelled as linear function of location x.

are reproduced in Figure 5.3A and B. We found that the distribution of velocity v can be characterized using a modified one dimensional Maxwell-Boltzman distribution. The fitting of probability density function $f_V(.)$

$$f_V(v|\gamma,\beta,\alpha) = \gamma v^{\beta} e^{\frac{-v^2}{\alpha}} \tag{5.5}$$

to data points indicated by the black crosses in Figure 5.3A resulted in a good fit with $SSR = 0.0003$. The fitted parameters are $\gamma = 0.0469, \beta = 0.5647$, and $\alpha = 97.4319$. The result of fitting $f_V(.)$ with stated parameter values is shown as a red dashed line in Figure 5.3A. The integration $\int_0^{+\infty} f(v)dv = 1$ applies as v can only take non negative values and subsequently solving the probability is done by $P(v) = \int f_V(v|\gamma,\beta,\alpha)dv$.

Figure 5.3B shows that although a large portion of cells show chemotactic behaviour indicated by frequency data in the range of $-\pi/2 < \varphi < \pi/2$, there exist a portion of cells that moved in the opposite direction of the gradient cAMP. We have tried fitting data points in Figure 5.3B with pdf from known family of distributions in order to derive a functional form for the angle variable φ. But we did not manage to find any density function that fit nor describe Figure 5.3B well. Hence the probability of angle $P(\varphi)$ is computed directly from Figure 5.3B.

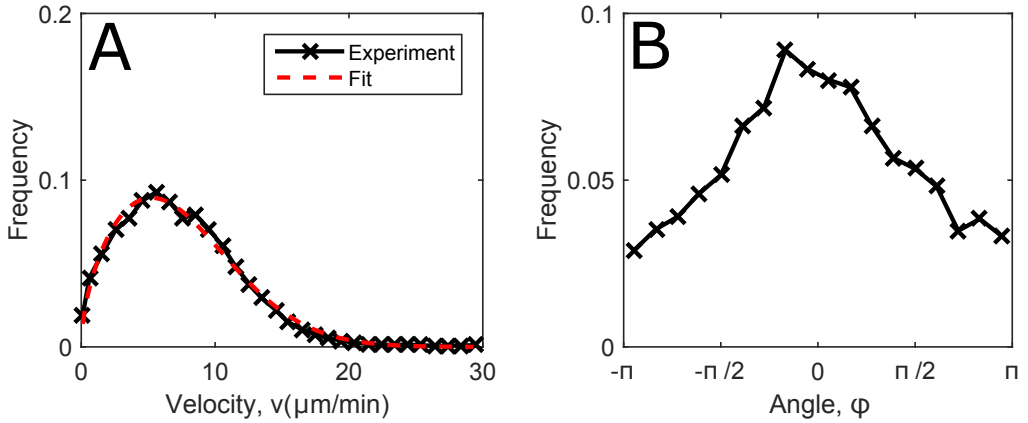

Figure 5.3: Distribution of velocity and angle of cells reproduced from Amselem et al. (2012). Data points in black crosses and lines were extracted by using ginput function in MATLAB. Each points represent the center of one histogram bin in Figure 2C and 2D of Amselem et al. (2012). (A) Distribution of velocity. Red dashed lines indicates fitted results. Refer text for details on the probability density function (pdf) equation and its parameter. (B) Distribution of angle where $-\pi/2 < \varphi < \pi/2$ indicate the gradient direction, $(\pi/2 < \varphi \leq \pi)$ or $(\pi/2 < \varphi \leq \pi)$ are cells that swim away from the direction of gradient. Cells swim perpendicular to the gradient when $\varphi = \pi/2, -\pi/2$.

5.4.1 Modelling fold change inside a chamber with linear gradient

In order to derive the prior $P(F)$, we first model the fold change experienced by the cell when moving from x_1 to x_2 in the microfluidic chamber as illustrated in Figure 5.2A where $\mathrm{x}_i, i = 1, 2$ is the distance i from the gradient source. Unlike many studies on *Dictyostelium* gradient sensing where fold is often defined as the ratio of concentration sensed across the length of the cell (Mato et al., 1975), here we define FCD as what the cell senses when moving between two locations. A single cell at x_1 will experience a concentration of $c(\mathrm{x}_1)$. When the cell swims with velocity v and at an angle φ with respect to the applied gradient, the distance travelled $\Delta\mathrm{x}$ along the gradient is obtained by

$$\Delta\mathrm{x} = v\tau\cos\varphi \tag{5.6}$$

where τ is the duration of the migration time. The new horizontal location of x_2 is derived as

$$\mathrm{x}_2 = \mathrm{x}_1 - v\tau\cos\varphi \tag{5.7}$$

Due to the fact that the gradient is the same everywhere in vertical direction, it is only necessary to consider the concentration of cAMP at its new horizontal location $c(\mathrm{x}_2)$. The fold change experienced by the cell is then defined as ratio of concentrations as

$$F = \frac{c(x_2)}{c(x_1)} \tag{5.8}$$

In order to describe the model of cAMP concentration $c(x)$ here we refer to how a linear gradient was generated in the experiment by Amselem et al. (2012). Both Song et al. (2006) and Amselem et al. (2012) generated a linear and stable gradient of cAMP using modified versions of pyramidal microfluidial network, a technique previously established by Jeon et al. (2000). Different concentration of cAMPs were mixed through networks of microfluidic channel where cAMP fluid flows parallel into the microfluidic chamber containing *Dictyostelium* cells. The analytical solution for a linear gradient of cAMP was previously derived by Postma and van Haastert (2009). They modelled the one dimensional diffusion of cAMP in a concentration gradient generated in a Zigmond chamber[2] given as

$$\frac{\partial c(x,t)}{\partial t} = D\frac{\partial^2}{\partial x^2}c(x,t) \tag{5.9}$$

where $D(\mu m^2/s)$ is the diffusion coefficient of cAMP and $c(x,t)$ is the cAMP concentration at distance x from the source at time t. Given that the concentration is maximal at x_0 and zero at $x = L$ where L is the length of the chamber, the solution at equilibrium yields

$$c(x) = c_0(1 - \frac{x}{L}) \tag{5.10}$$

where c_0 denotes the maximal concentration at x_0 (Refer Figure 5.2B for illustration of the concentration profile of the linear gradient). Substituting equation 5.10 in equation 5.8, we obtain the fold change F

$$F = \frac{(1 - \frac{x_2}{L})}{(1 - \frac{x_1}{L})} \tag{5.11}$$

where the term c_0 cancels. The location variable x_2 is as defined earlier in equation 5.10. Therefore the fold change can be expressed as

[2]In a Zigmond chamber, cells were placed under a glass bridge supported by two glass strips. Two blocks of agar as chemoattractors are then placed at each side of the glass bridge. The linear gradient is created by the two blocks of agar(Postma and van Haastert, 2009).

$$\begin{aligned} F &= \frac{L-(x_1-v\tau\cos\varphi)}{L-x_1} \\ &= 1+\frac{\tau}{\lambda}v\cos\varphi \end{aligned} \tag{5.12}$$

where $\lambda = L-x_1$ and $\tau \geq 0$. The condition $\lambda \geq 0$ applies, constraining location x_1 which can not be further than the length of the chamber($x_1 \ll L$). Here we treat τ and λ as constants. The derived fold change is then $F = g(v, \varphi; \tau, \lambda)$, a function of two variables; velocity v and angle φ parameterised by two constants τ and λ where $g : \mathbb{R}^+ \to \mathbb{R}^+$. The range of φ considered is consistent with the range of data in Figure 5.3B where $-\pi \leq \varphi \leq \pi$. Figure 5.4 is the result of equation 5.12 plotted for the considered range of φ and $0 \leq v \leq 30$. Fold F is either an increasing or decreasing function determined by angle φ and has a slope of τ/λ. It can be easily seen from equation 5.12 and Figure 5.4 that $F = 1$ when $\varphi = -\pi/2, \pi/2$. It is also observed from Figure 5.4 that fold F increases maximal when the cell swims directly up the gradient at $\varphi = 0$.

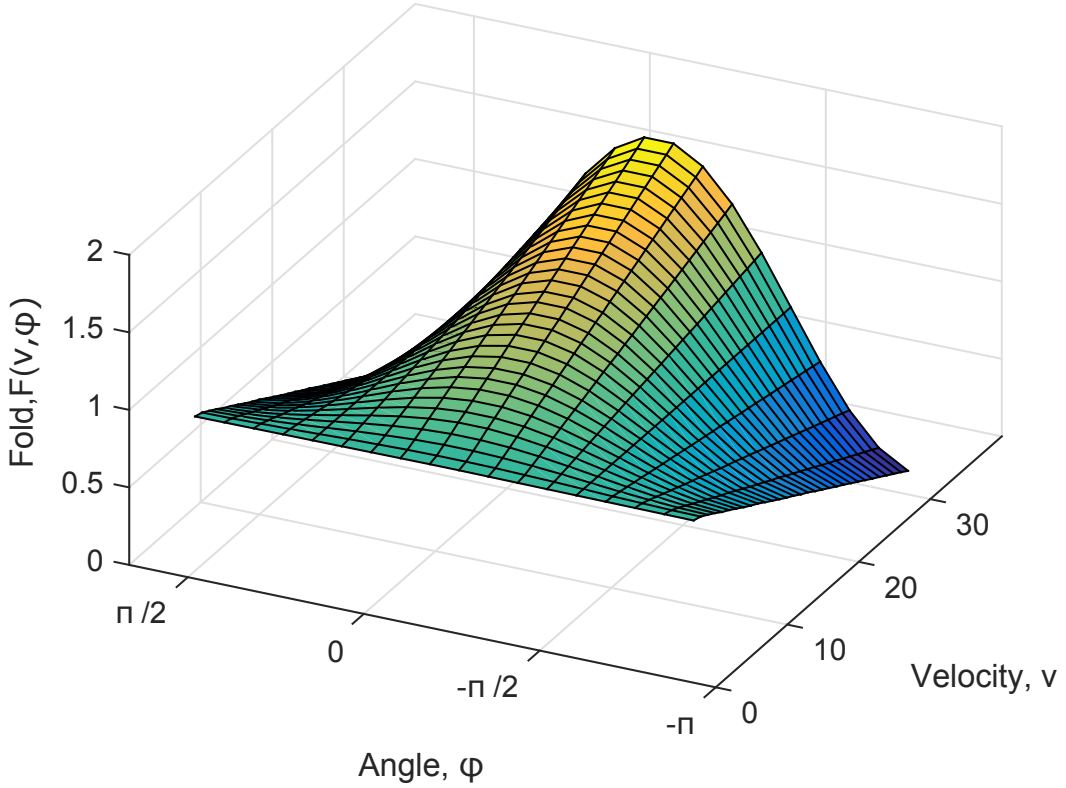

Figure 5.4: Fold change $F = g(v, \varphi; \tau, \lambda)$ as a function of velocity v and angle φ computed from equation 5.12. Parameters are fixed as $\tau = 0.015, \lambda = 1$.

We introduce here the constraints imposed to ensure a logical definition of equation 5.12. When the cell swims in the direction of the gradient ($\cos(\varphi) > 0$), the maximum distance that it can travel is limited to x_1 where this constraint is expressed as

$$v\tau\cos(\varphi) \leq x_1 \tag{5.13}$$

Equation 5.12 is then upper bounded as

$$F \leq 1 + \frac{x_1}{L - x_1} \tag{5.14}$$

If the length of the chamber is hypothetically long $L \to +\infty$, and the distance x_1 at which the cell is located is close to L ($x_1 = L + \delta$, where δ is small distance between L and x_1), then the maximum fold change that can be sensed by the cell is $F \to +\infty$. The possible range of fold change is then $F = (1, +\infty]$.

When the cell swims in the opposite direction of the gradient ($\cos(\varphi) < 0$), the cell can travel no further than $L - x_1$, and the constraint is expressed as

$$|v\tau\cos(\varphi)| \leq L - x_1 \tag{5.15}$$

Similar as before, equation 5.12 is lower bounded as

$$F \geq 1 - \frac{L - x_1}{L - x1} \tag{5.16}$$

where the minus sign is due to $\cos(\varphi) < 0$. The minimum 'reduced' fold change sensed is $F = 0$, and the range of fold change is $F = [0, 1)$. This is in line with the definition of fold change where $F < 0$ is not possible. No fold change $F = 1$ is sensed when the cell is static ($v = 0$) or when it swims perpendicular to the direction of the gradient ($\cos(\varphi) = 0$).

5.4.2 Conditional density by transformation of random variable

Now that we have a model of fold F defined by equation 5.12 and characterized the pdf of velocity v in equation 5.5, we proceed to derive the pdf of fold F conditioned on angle φ,$f(F|\varphi)$ using the transformation of random variable technique. We have established the relation between fold F and v through $F = g(v, \varphi; \omega)$. For a fixed angle φ, the function $g(v|\varphi; \omega)$ is differentiable and monotonic where $g(\cdot)$ is a strictly increasing or decreasing function. Let V be a random variable representing any possible value of velocity v described by density function $f_V(v)$. Since V is a continuous random variable, $F^* = g(V)$ is also a continuous random variable. The density of F^* is then derived using the transformation of random variables as

$$f_{F^*}(F) = f_V(g^{-1}(F)) \left| \frac{d}{dF} g^{-1}(F) \right| \tag{5.17}$$

where $f_V(\cdot)$ is the density function for velocity derived earlier in equation 5.5. $g^{-1}(F)$ is the inverse function and is obtained by rearranging equation 5.12 as

$$g^{-1}(F) = \frac{\lambda}{\tau \cos\varphi}(F-1) \tag{5.18}$$

$$= \omega \frac{(F-1)}{\cos\varphi} \tag{5.19}$$

where $\omega = \lambda/\tau$ is introduced for brevity. The derivative of the inverse function is computed as

$$\frac{d}{dF} g^{-1}(F) = \frac{\omega}{\cos\varphi} \tag{5.20}$$

Putting it all together, the density function of fold F given angle φ, $f(F|\varphi)$ is derived as

$$f_{F^*}(F|\varphi) = \gamma \left(\omega \frac{(F-1)}{\cos\varphi} \right)^{\beta} \exp\left(\frac{-(\omega(F-1)/\cos\varphi)^2}{\alpha} \right) \left| \frac{\omega}{\cos\varphi} \right| \tag{5.21}$$

Since the fitted parameter $\beta \approx 0.5$, the conditional density function can be rewritten as

$$f(F|\varphi) = \gamma \left| \frac{\omega}{\cos\varphi} \right| \sqrt{\omega \frac{(F-1)}{\cos\varphi}} \exp\left(\frac{-(\omega(F-1)/\cos\varphi)^2}{\alpha} \right) \tag{5.22}$$

Previously, we introduced restrictions to the range F with respect to φ to maintain a logical definition of equation 5.12. Similarly here we consider restrictions imposed by φ on the density function. In order to avoid solutions with complex numbers due to $\sqrt{\omega \frac{(F-1)}{\cos\varphi}}$, the range of F is $F \geq 1$ for φ that results in $\cos\varphi > 0$ and F is $0 \leq F \leq 1$ for φ where $\cos\varphi < 0$. In the case of $\varphi = \pi/2, \pi/2$, the density function is undefined for $\omega > 0$ and zero for $\omega = 0$ due to $|\omega/\cos\theta|$.

The result of plotting equation 5.22 for different angles φ is shown in Figure 5.5. When a *Dictyostelium* cell moves in the opposite direction of the gradient, it is more likely to sense a much reduced fold change as the angle of deviation widens as indicated in Figure 5.5A. In contrast Figure 5.5B shows that the cell is likelier to experience a wider and higher range of fold change when swimming closer to the gradient direction. Both Figure 5.5A and B shows that the probability of sensing fold change close to 1 is the

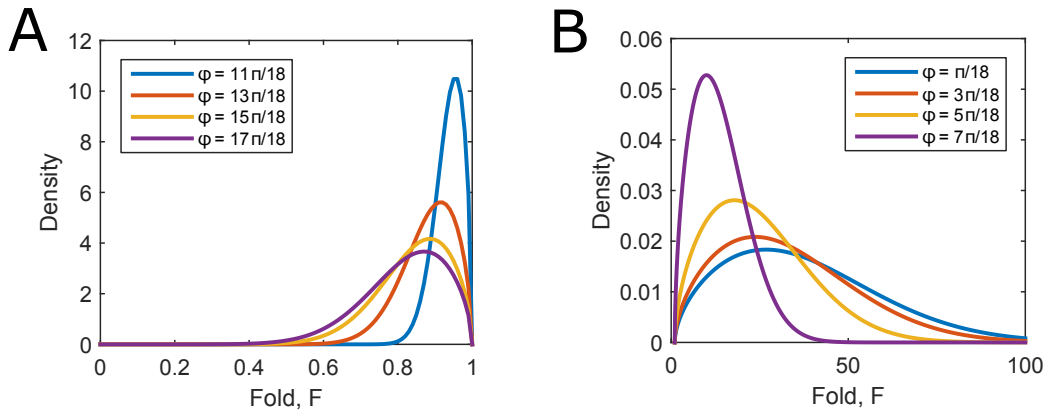

Figure 5.5: Conditional probability density function $f(F|\varphi)$ from equation 5.21 plotted for various range of φ. Different values of ω are used for readability and contrasting purposes. Areas under all curves are equal to 1. (A) When $\cos\varphi < 0$ with $\omega = 30$. (B) When $\cos\varphi > 0$ with $\omega = 0.2$

highest with the width of the density narrowing as the cell swims perpendicular to the gradient indicated by curves of $f(F|\varphi = \pi/8)$ and $f(F|\varphi = 11\pi/8)$.

5.4.3 The constraint on ω

Throughout our derivation is based on available experimental data and we have treated the term $\omega = \lambda/\tau$ or equivalently $\omega = L - x_1/\tau$ as a constant. As a result we have observed in Figure 5.5 how different values of ω leads to different density function curves. If ω can be arbitrarily chosen, then for certain values of ω the density function of equation 5.21 with fixed parameters γ, β, α would not integrate to 1. We derive here the restrictions on ω in order to ensure the density function integrates to 1. Equation 5.15 can be rearranged in terms of the components of ω as

$$\begin{aligned} v\tau|\cos\varphi| &\leq L - x_1 \\ \frac{\tau}{L - x_1} v|\cos\varphi| &\leq 1 \\ \frac{L - x_1}{\tau} &\geq v|\cos\varphi| \end{aligned} \tag{5.23}$$

τ is previously defined as the duration of time that the cell moves. When a change in concentration is detected, the time that it takes for the response of intracellular RasGTP to return to its steady state after stimulation is denoted as T_{adapt} as illustrated in Figure 5.6. Introducing external stimulus during this refractory period will not yield any response from the cell. It is known that the cell moves in steps where the steps are either caused by the sensing of fold change or just a random walk. Therefore duration of cell movement τ can be further defined as

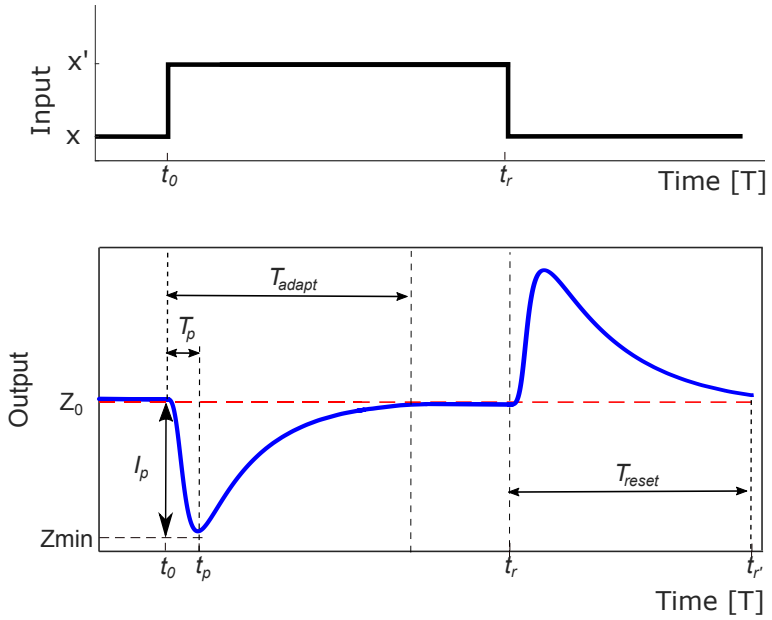

Figure 5.6: Illustration of Figure 2E experiment result by Takeda et al. (2012)). Upper panel shows the step up and step down cyclic AMP input where x = 100 nM and x'=1μM. Lower panel is the average response of RasGTP in *Dictyostelium* cells to the step input of the upper panel. Also indicated in the lower panel are the time durations for various response behaviour where $T_p = 19\text{s}, T_{adapt} = 50\text{s}, T_{reset} = 60\text{s}$.

$$\tau = t_{\text{FCD}} + t_{\text{random}}$$

where t_{FCD} is time of movement caused by fold change detection and t_{random} is time of movement caused by random walk. During the period T_{adapt} the cell has moved between two location x_1 and x_2 regardless of the number of steps. These movements during T_{adapt} are considered as movements caused by fold change and therefore τ is lower bounded by T_{adapt} such that

$$\tau \geq T_{adapt} \tag{5.24}$$

where the duration of a movements must be at least the length of time of the refractory period. Like I_p and T_p that has been mainly the subject of our discussions so far, the duration of cellular property T_{adapt} varies between cells and is determined by the internal parameters(deterministic approach). The value of T_{adapt} is extracted from Takeda et al. (2012) Figure 2F experiment result. The result shows the average response and variability of *Dictyostelium* cells to a step change of cyclic AMP input up from 100nM to 1μM and down from 1μM to 100nM. From the figure, the duration of T_{adapt} is $\approx$ 1min. The maximum velocity recorded in the experiment by Amselem et al. (2012) is $v = 30\mu$m min^{-}1. Therefore the minimum length of the microfluidic chamber $L - x_1$ is

$$\begin{aligned} L - x_1 &\geq v\tau|\cos\varphi| \\ &\geq (30\mu\text{m/min})(1\text{min})|\cos\varphi| \\ &\geq 30\mu\text{m} \end{aligned}$$

where $|\cos\varphi|$ is maximum at $\varphi = \pi, -\pi$ and consecutively $\omega \geq 30\mu$m/min.

5.4.4 Chemotaxis experiment based prior

Now that we have an analytical expression for the conditional density function, the conditional probability of fold F given angle φ is then solved by

$$P(F \in F \pm \delta_F|\varphi) = \int_{F-\delta_F}^{F+\delta_F} f(F|\varphi)dF \tag{5.25}$$

Due to restrictions imposed on the density function by angle variable φ as discussed earlier the value of ω must be chosen such that the integration $\int_1^{+\infty} f(F| - \pi/2 < \varphi < \pi/2)dF = 1$ and $\int_0^1 f(F| - \pi \leq \varphi < -\pi/2, \pi/2 < \varphi \leq \pi)dF = 1$ applies. Thus the prior $P(F)$ representing the probability of a *Dictyostelium* cell sensing fold F regardless of angle is derived as

$$P(F) = \sum_{\varphi} P(F|\varphi)P(\varphi) \tag{5.26}$$

The probability of angle $P(\varphi)$ is solved directly from Figure 5.3B. Each points in Figure 5.3B represents a center of the histogram bin in Figure 2D of Amselem et al. (2012). The width of each histogram bin is $\pi/9$ and therefore the probability of angle $P(\varphi = x)$ is the result of the height of the histogram represented by the frequency multiplied by the width. Equation 5.26 is then solved numerically for discrete values of angle φ indicated in Figure 5.5B.

In the case of $P(F = 1)$, the probability of $P(F = 1|\varphi = -\pi/2, \pi/2)$ is solved separately because the conditional density function is non-integrable since we have defined the equation 5.12 such that $F = 1$ is only possible when $\varphi = -\pi/2, \pi/2$. However it is not accurate to assume $P(F = 1) = 0$ as Figure 5.5B clearly shows that there are cell movements perpendicular to the direction of gradient at $\varphi = \pi/2, -\pi/2$. Therefore for $P(F = 1)$

$$
\begin{aligned}
P(F=1) &= \sum_{\varphi} P(F=1|\varphi)P(\varphi) \\
&= P(F=1|\varphi=-\pi/2)P(\varphi=-\pi/2) + P(F=1|\varphi=\pi/2)P(\varphi=\pi/2) \\
&= (1)(0.0515) + (1)(0.0534) \\
&= 0.1049
\end{aligned}
$$

If a cell is observed to move at angle $\varphi = -\pi/2, \pi/2$ the probability $P(F = 1|\varphi = -\pi/2, \pi/2) = 1$ regardless of velocity because the gradient is one dimensional. Probability $P(\varphi = -\pi/2)$ and $P(\varphi = \pi/2)$ are both obtained by computing the area under the density curve of Figure 5.5B resulting in $P(F = 1) = 0.1049$. The result above is combined with numerical solution to equation 5.26 where conditional probability $P(F|\varphi) = \int f(F|\varphi; \omega, \gamma, \beta, \alpha)dF$ and the density function parameters set as $\omega = 30, \gamma = 0.0469, \beta = 0.5647, \alpha = 97.4319$. The computation result for prior $P(F)$ distribution modelled based on chemotaxis experiment is shown in Figure 5.7.

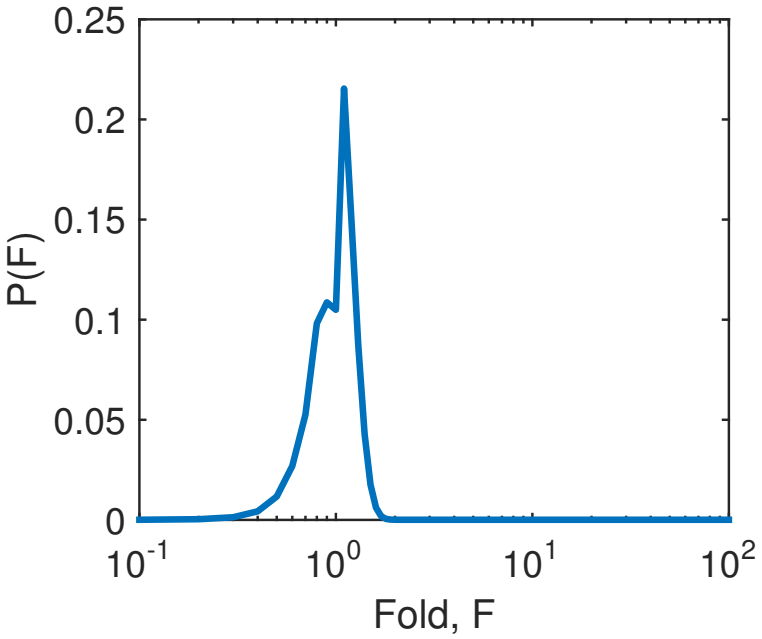

Figure 5.7: Prior Probability of Fold $P(F)$ averaged over all angles and modelled based on chemotaxis experiment data. The parameters are fixed as $\omega = 30, \gamma = 0.0469, \beta = 0.5647$ and $\alpha = 97.4319$.

It can be observed from Figure 5.7 that the prior is significant for only a narrow range of approximately $F = 0.2 \sim 2$. As a short summary, we can infer the probability of cell sensing increased fold change as $P(F > 1) = 0.5910$ where this is also the probability of cell swimming up the gradient $P(F > 1) = P_{forward}$. Likewise the probability of cell sensing reduced fold change is $P(0 < F < 1) = 0.3040$ and similarly this is also the probability cell moving in the opposite direction of gradient $P(0 < F < 1) = P_{backward}$.

Lastly the probability of the cell sensing no changes in fold is $P(F = 1) = 0.1049$ which indicates the cell swimming perpendicular to the gradient $P(F = 1) = P_{perpendicular}$. Therefore our model here indicates that there is a probability of 60% that a *Dictyostelium* cell senses an increase in fold change. The prior probability of fold derived here is referred hereafter as the 'chemotaxis prior'.

5.5 Uniform, exponential and Weibull Distribution as alternative priors

Although we have modelled prior $P(F)$ based on chemotaxis experiment as Figure 5.7, it is interesting to compare with other alternative priors modelled differently. Among the limitations posed by the experiment based prior is that the one dimensional linear gradient setting does not approximate the gradient found in a natural environment. Considering that extracellular cAMP is not only diffused but is also degraded by cyclic nucleotide phosphodiesterase (PDE) secreted by *Dictyostelium* cells themselves (Sucgang et al., 1997), the cAMP gradient is more likely to be exponentially decreasing in time and space. The exponentially decreasing gradient of concentration cAMP is modelled in chapter 6. In this section we assume that the alternative priors are drawn from established families of distribution. How does different priors affect both the distribution of marginal and posterior probability?

We chose the uniform, exponential and Weibull distribution as three alternative model priors. The uniform distribution as a non-informative prior is a sensible choice in the absence of information on gradient[3]. This would remove preferences to any fold change considered and in general allow information from the experiment data to contribute more to the posterior. Whereas the uniform prior assigns equal weights to each fold change, the exponential prior is selected to reflect a strong bias towards low fold and the Weibull prior to represent bias in a specific range of fold. Given fold range $\mathbf{F} = (1.1, 1.2, \ldots, F_j, \ldots, 100)$, the uniform prior is computed as

$$P(F_j \in F_j \pm \delta_F) = \int_{F_j-\delta_F}^{F+\delta_F} \frac{1}{F_{max} - F_{min}} dF$$

where in our case $F_{min} = 1.1, F_{max} = 100$. The exponential prior is computed as

$$P(F_j \in F_j \pm \delta_F) = \int_{F_j-\delta_F}^{F_j+\delta_F} \lambda e^{-\lambda F_j - 1} dF$$

[3]We acknowledge that the non-informative property of the uniform distribution is subject to debate. One example of this disputation is given by Zwickl and Holder (2004) where the uniform prior leads to a biased estimate of the posterior in the general time-reversible model. A more suitable candidate for a non-informative prior is the Jefrey's prior (Jeffreys, 1946).

where the degradation rate parameter $\lambda = 1/20$. The Weibull prior is computed as

$$P(F_j \in F_j \pm \delta_F) = \int_{F_j-\delta_F}^{F_j+\delta_F} \frac{k}{\gamma}(\frac{F_j-1}{\gamma})^{k-1} e^{(F_j-1/\gamma)^k} dF \tag{5.27}$$

where the shape parameter is $k = 1.5, k < 0$ and the scale $\gamma = 23, \gamma > 0$. We solved the prior probability for $\forall F_j \in \mathbf{F}$ and showed the results as panels in the top row of Figure 5.8 The exponential and Weibull functions are shifted along the horizontal by 1 as the we only calculate from $F = 1.1$. The integral width δ is chosen such that $\sum_{F=1.1}^{F=100} P(F) = 1$.

5.6 Marginal and posterior

Now that we have computed the conditional probability $P(I_p|F)$ and prior distribution $P(F)$, we proceed to compute the marginal and subsequently solve the posterior probability of a cell sensing fold F_j when we have observed a certain $I_{p,i}$ value. The marginal probability of observing $I_{p,i}$ is obtained by integration over all probabilities of fold change given by the prior

$$P(I_{p,i}) = \sum_{F_j \in \mathbf{F}} P(I_{p,i}|F_j)P(F_j)$$

where $P(I_{p,i}|F_j)$ is the conditional probability (Figure 5.1) and $P(F_j)$ is the prior. The results of computing the marginal distribution by considering all values of $I_{p,i} \in \mathbf{I_p}$ with different priors modelled earlier are shown as panels in the second row from the top of Figure 5.8. The chemotaxis based prior distribution is normalized in the range of $\mathbf{F} = (1.1, 1.2 \ldots, 100)$ to match the discrete range computed by the conditional probability.

5.6.1 Conditional probability and the bias of priors is reflected in different region of the marginal

Figure 5.8 indicates that it is more probable to observe I_p in the range of $I_p > 0.5$ when the marginals are computed by the alternative priors. The marginals of alternative priors also demonstrate unimodal characteristics where a large portion of the total probability is made up by $I_p > 0.5$ with maximal at $I_p \approx 0.74$. The comparatively high probability in the region of $0.5 \leq I_p \leq 1$ is caused by saturation of the mean μ_L^F given fold $F > 20$ at $I_p \approx 0.74$ (Refer Figure 4.8). The marginal distributions are affected only sightly by the alternative priors in the region of $I_p < 0.5$. In contrast, the marginal by the chemotaxis based prior shows that most of the chances of observing I_p lies within the range of $I_p < 0.2$. The distribution is bimodal and has peaks at $I_p = 0.1$ and $I_p = 0.7$ where the probability of the former is significantly higher than the latter. The marginal

is affected by the strong bias concentrated in region of lower F of the chemotaxis based prior.

5.6.2 Posterior reveals that detection of high fold change is highly unlikely

Having computed the marginal distributions with different types of priors, we proceed to solve the posterior probability that the fold detected is F_j given observed response of $I_{p,i}$ as

$$P(F_j|I_{p,i}) = \frac{P(I_{p,i}|F_j)P(F_j)}{P(I_{p,i})}$$

The numerator part is also the joint distribution between $I_{p,i}$ and F_j denoted as $P(I_{p,i}, F_j) = P(I_{p,i}|F_j)P(F_j)$. The equation above is solved for all $\forall I_{p,i} \in \mathbf{I_p}$ and $\forall F_j \in \mathbf{F}$ to yield a distribution of posterior. The results are shown over two rows in the bottom half of Figure 5.8 where only results for selected $I_{p,i} \in \mathbf{I_p}$ are displayed for readability purposes. In the same way that we analysed the marginals, the posteriors computed from different priors are also shown in separate columns. The second row from the bottom indicates posterior of fold given observed $I_p = 0.1, 0.2, \ldots, 0.5$ (low I_p) and the bottom row for $I_p = 0.6, 0.7, \ldots, 1$ (high I_p).

Two stark contrasts can be seen from Figure 5.8. Firstly, the posterior probability of fold detected for $I_p \leq 0.5$ and $I_p > 0.5$ is of a different magnitude. This can be seen from the difference in scale of the vertical axis between the two bottom rows. Secondly, given that we observed $I_p < 0.5$, the probability of detecting fold is only in the range of $F \leq 10$ and it is highly unlikely that $F > 10$ is being detected. Likewise the chances of detecting $F \leq 10$ is almost non existent if I_p observed is $I_p > 0.6$. In this range, although the chances are comparatively small, it is more likely that the fold detected is of $F > 10$. Regardless of the priors, the posterior distributions indicates that the probability of detecting fold $F \leq 10$ decreases almost exponential-like as the observed I_p is higher. Thus it can be concluded that the range of fold that is significantly enough to be detected is within $F \leq 10$ and it is highly unlikely for the population cells to detect fold change beyond $F = 10$.

5.6.3 Posterior is strongly influenced by the conditional probability regardless of prior bias

In order to understand the effect of priors on the posteriors, we first study the posterior based on the uniform prior shown in the second column of Figure 5.8. As each prior fold is equally likely, any occurring bias in the posterior is a result of the conditional

probability. The uniform prior based posterior serves as a benchmark when studying the effects of other priors. The effect of bias in the exponent and Weibull prior is only evident on the posteriors conditioned on high I_p at $I_p > 0.5$. It is only when the bias is concentrated in the region of small fold as provided by the chemotaxis based prior that the shape of the posterior distribution conditioned on low I_p is affected. The distribution shape for $P(F|I_p = 0.3)$ has two peaks with high probability assigned to fold $F = 1.1$. Because the chemotaxis based prior assigns almost zero probability to $F > 2$, the posteriors derived in the region where $I_p > 0.5$ is of the same dynamics as the uniform based posterior.

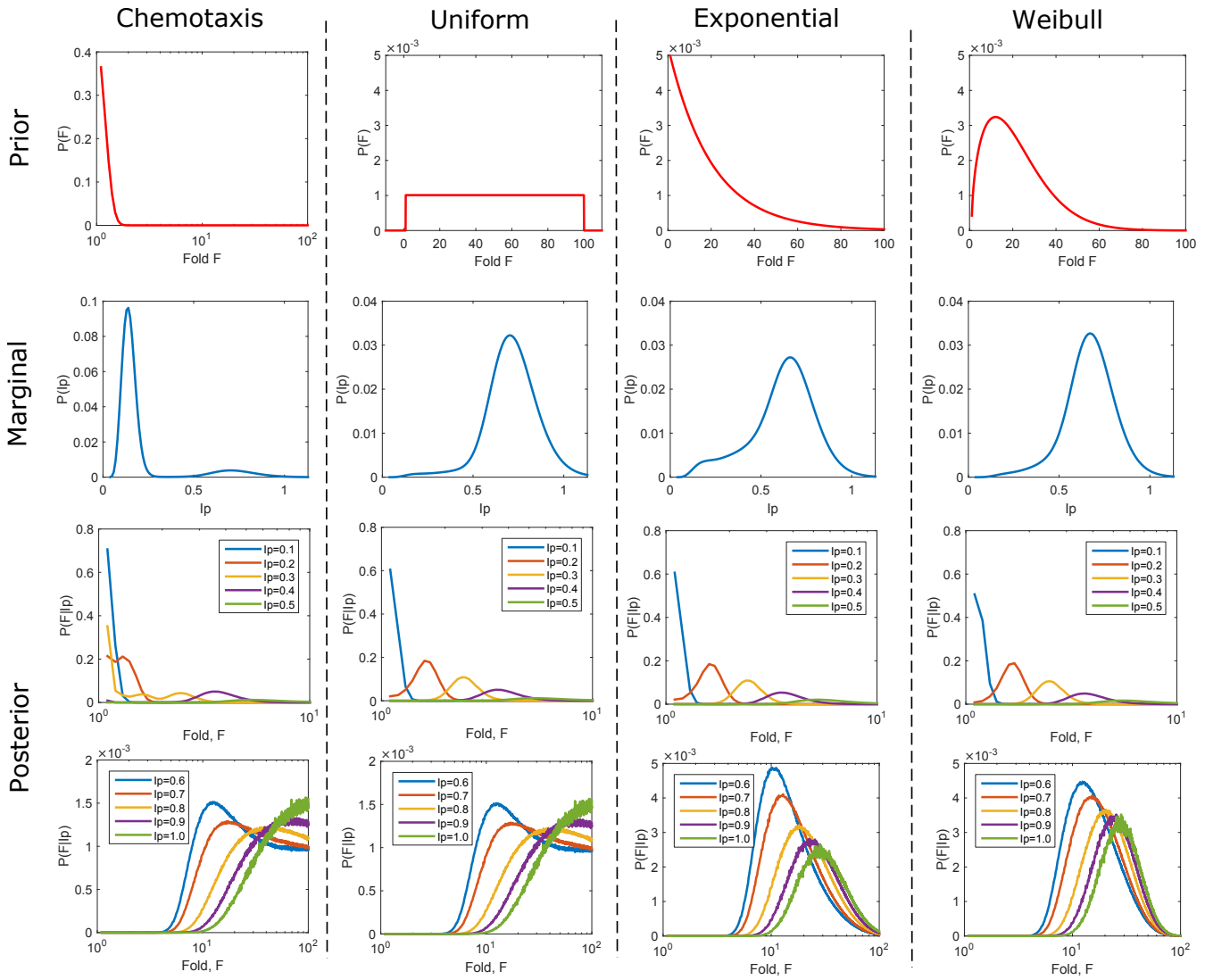

Figure 5.8: Results of inferring the posterior probability of the fold sensed by a cell is F given an observed Ip $P(F|I_p)$ using Bayes' theorem. Each column represent results from using different priors. The results for the posterior distributions are divided into two parts with different scale. Only sample results are shown for the posterior. Axes are scaled identically except where doing so would significantly reduce the readability of the plot.

5.7 Background dependencies

In this section we investigate how different background concentration of cAMP influence the conditional probability and subsequently the posterior of $P(F|I_p, x)$ where x denotes the background cAMP. The comparison will be between background $x = 1$nM and $x = 100$nM. The procedure of solving the posterior is the same as when we solve for the conditional probability and marginal for different priors. The difference lies in the density function used to solve for the conditional probability where it is dependant on both fold F and background cAMP x.

5.7.1 Conditional probability

To solve for the conditional probability of $I_{p,i}$ given stimulus fold F_j and background cAMP x, we integrate the density function of equation

$$P(I_{p,i} \in I_{p,i} \pm \delta|F_j, x) = \int_{I_{p,i}-\delta}^{I_{p,i}+\delta} \frac{1}{I_{p,i}\sigma_{x_i,F_j}\sqrt{2\pi}} \exp\left(\frac{-(\ln I_{p,i} - \widetilde{I}_p^{\,x_i,F_j})^2}{2\sigma^2_{x_i,F_j}}\right) dI_{p,i}$$

Each of the mean $\widetilde{I}_p^{\,x_i,F_j}$ and standard deviation σ_{x_i,F_j} of the density function is approximated by a quadratic function respectively as previously derived in equation 4.5 and equation 4.6

$$\begin{aligned} \widetilde{I}_p^{\,x_i,F_j} &= a_1^{F_j} x_i^2 + b_1^{F_j} x_i + c_1^{F_j} \\ \sigma_{x_i,F_j} &= a_2^{F_j} x_i^2 + b_2^{F_j} x_i + c_2^{F_j} \end{aligned}$$

where the quadratic parameters $a_k, b_k, c_k, k = 1, 2$ are functions of fold F itself as summarised in table 4.1. The result of computing $P(I_{p,i}|F_j, x)$ for all $I_{p,i} \in \mathbf{I_p}, F_j \in \mathbf{F}$ and $x = (1, 100)$ is shown in Figure 5.9. The result shows that the distributions of $P(I_p|F, x)$ for both background cAMP becomes more and more similar as the conditioned F increases, indicating saturations. However, the uncertainties do not increase in the manner where $P(I_p|F, x)$ distributions become more right tailed as we have clearly observed in Figure 5.1. Compared with Figure 5.1, there is a higher confidence about the level of I_p that can be observed given a particular fold change in stimulus in both background. Figure 5.9B shows that when the fold change in stimulus is based upon a stronger background, the saturation of $P(I_p|F, x)$ happens at a faster rate. Interestingly enough, stimulating cells with fold of stronger background does not increase the probability of observing higher I_p. In fact with background cAMP $x = 100$nM, the highest I_p that is likely to be observed is limited in the range of $I_p = 0.5 \sim 0.71$. If we want

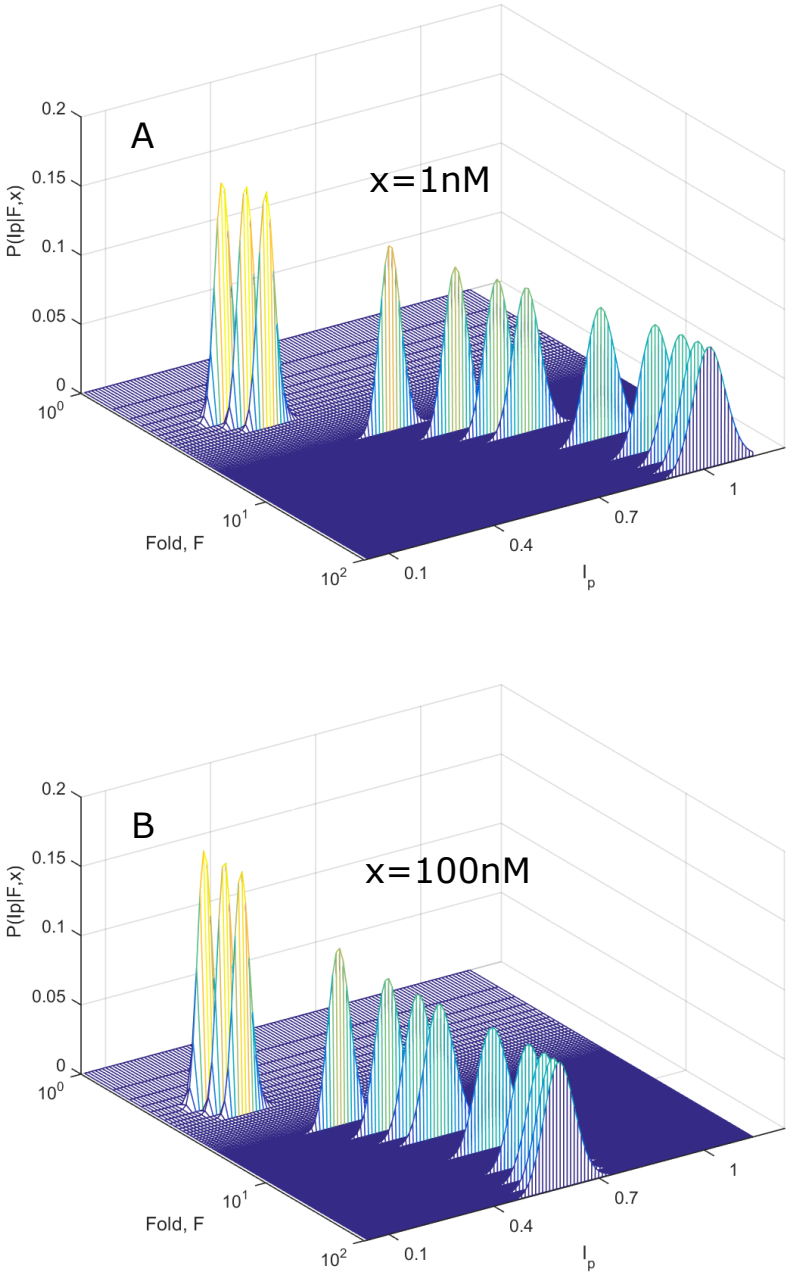

Figure 5.9: Conditional probability distribution $P(I_p|F,x)$ with background cAMP dependencies

to increase the chances of observing higher I_p then we should stimulate cells with high fold of lower background such as fold $F = 10$ with $x = 1$nM that yields observable I_p in the range of $I_p = 0.93 \sim 1.14$ (Figure 5.9A). The $P(I_p|F, x = 100)$ distributions given $F > 20$ overlapped more compared to $P(I_p|F, x = 1)$ conditioned upon the same fold range. Therefore, we can expect that $P(I_p|F, x)$ distributions are also more distinguishable when conditioned upon stimulus fold in the range of $F > 20$ of weaker background cAMP. Using the overlapped areas as a measure of establishing distinguishable folds as

what we have done in chapter 4, we can also expect that the stimulus folds are easier to distinguished when the background concentration is weak.

5.7.2 Marginal and posterior

The marginal with background dependencies $P(I_{p,i}|x)$ is solved as

$$P(I_{p,i}|x) = \sum_{F_j \in \mathbf{F}} P(I_{p,i}|F_j, x)P(F_j)$$

where $P(F_j)$ is the different types of priors modelled earlier. The result of computing the marginal for all $I_{p,i} \in \mathbf{I_p}, F_j \in \mathbf{F}, x = (1, 100)$ and for the different types of priors is shown in Figure 5.10. The result shows that in general when the background cAMP is strong the marginal distributions yielded is denser with a narrower significant range that shifts to the left. Figure 5.10 indicates that with the exception of the marginal based on the chemotaxis prior, we are likely to observe lower I_p in the vicinity of $I_p = 0.5$ when there is a strong background concentration regardless of the amount of fold change itself. The chemotaxis based prior marginal maintains its bias towards observing very low I_p in the range of $I_p = 0.11 \sim 0.2$ although with stronger background cAMP, the chances of observing around $I_p = 0.5$ slightly increases.

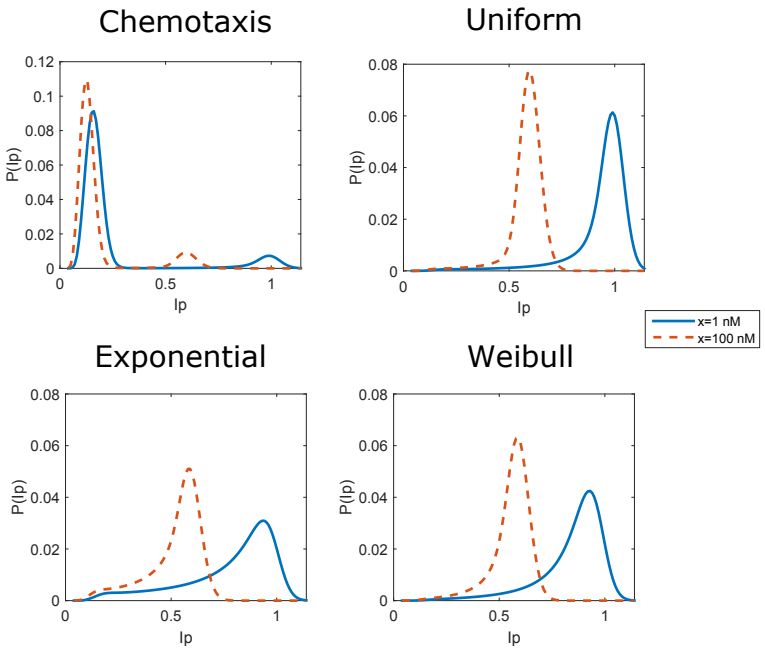

Figure 5.10: Marginal probability distribution $P(I_p)$ with background cAMP dependencies.

Finally the posterior with background dependencies is solved as

$$P(F_j|I_{p,i},x) = \frac{P(I_{p,i}|F_j,x)P(F_j)}{P(I_{p,i}|x)}$$

where as before it is solved for $I_{p,i} \in \mathbf{I_p}, F_j \in \mathbf{F}, x = (1, 100)$. The result is shown in Figure 5.11. As expected, the effect of background cAMP emerges when the posterior is conditioned upon $I_p > 0.5$ (indicated in panels of second and fourth row from top) as this is the region where the saturation of the conditional probability occurs. For example, $P(F|I_p)$ conditioned on $I_p = 0.6$ has high probability values in the range of $F = 4 \sim F = 10$ when derived from conditional probability based on weaker background cAMP. In contrast, the same posterior has lower probability values in the range of $F = 10 \sim F = 100$ when the background cAMP of fold change used to stimulate the conditional probability is stronger. As can be seen from panels of the second and fourth row, this trend is evident across all priors. Therefore conditional probabilities with a slower saturation rate results in a more separable posteriors.

With the exception of the chemotaxis prior based posterior, the influence of priors bias on the posterior is only visible for when the conditioned I_p is in the range of $I_p > 0.5$. Like the priors, the effects of background cAMP on the posterior is also noticeable when the posterior is conditioned upon the region of $I_p > 0.5$. Only with a strong bias towards lower fold as shown by the chemotaxis prior can we see the changes in the posterior of fold distribution conditioned upon $I_p < 0.5$.

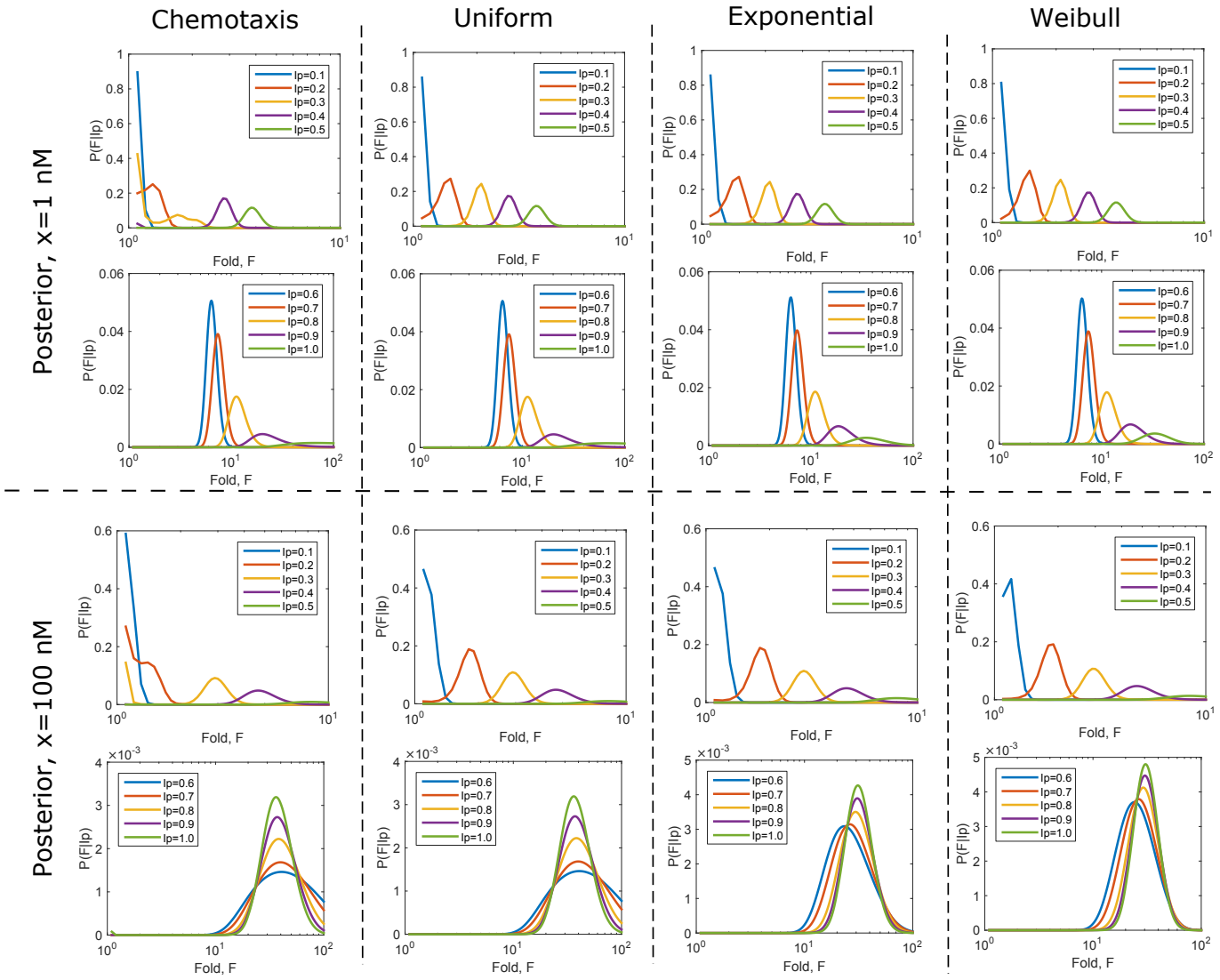

Figure 5.11: The results for the posterior distributions with background dependencies. Results are separated according to the prior type (column) and background cAMP(row). Only sample results are shown. Axes are scaled identically except where doing so would significantly reduce the readability of the plot.

5.8 Summary

This chapter is devoted to model for fold change F and response peak I_p the conditional probability $P(I_p|F)$, prior $P(F)$, marginal $P(I_p)$ and finally derive the posterior probability distribution $P(F|I_p)$. We modelled the prior based on chemotaxis and also included priors chosen from some family of distribution for comparison. The conditional probability shows that the probability of observing lower I_p given small fold would always surpass the conditional probability of observing higher I_p no matter how strong the stimulus fold is. The chemotaxis prior shows that small fold changes have higher chances of being sensed and that the conditional probability drops almost exponentially for larger folds.

The biggest take-away message however, lies with the derived posterior probability of fold $P(F|I_p)$. We can see a slight 'anti-bayesian' effect [4] where the posterior is primarily determined by the conditional probability and where only a very strong bias in the prior will swing the posterior towards the prior. This suggest that the chances of sensing a particular small fold although is obviously very high, but more importantly is also primarily determined by the conditional probability where its behaviour in turn is dependent on the characteristics of the population of virtual cells and constrained by the limitation of the model ODEs. The stimulus statistics computed and as seen in the chemotaxis prior does not pose much influence and therefore regardless of what the cell's internal beliefs are, what is more important is what does the population has to say. The effects of background cAMP is similar to the priors where it is apparent in posteriors conditioned upon high I_p. Again, only the chemotaxis prior which biases strongly towards lower fold, changes the posterior conditioned upon lower I_p in both weak and strong background cAMP. The probability components derived in this chapter will be used to model the cell's internal perception in the next chapter.

[4] Anti-Bayesian effect is when the estimated posterior is repulsed away from the prior mean by the likelihood. We will discuss this further in chapter 6, specifically in section 6.2.

Chapter 6

Relation with the external world

6.1 Introduction

The stimulus-perception-response mechanism of a biological organism is often studied at a coarse level, where the signalling pathway is viewed as a 'communication channel' rather than analysing the complicated intracellular bio-chemical reactions that constitute it. The objective is then to maximise the propagation of information along the pathway for the organism to make decisions as accurate as possible (Sims, 2016; Marzen and DeDeo, 2017). This information theory approach has also been applied to the study of *Dictyostelium* cells where the rate of information that must not be corrupted in order for cells to make decisions on motility was derived (Iglesias, 2016). In this chapter instead of analysing the full stimulus-perception-response mechanism, we introduce the 'Bayesian Observer Model' (referred hereafter as the 'Observer Model') from the field of theoretical neuroscience in order to characterize the stimulus-perception of FCD of *Dictyostelium* cells. Some parts of the model's components have already been characterized in chapter 4 and 5 as described in the next section.

We begin by introducing some background literature and key concepts on how stimulus information is encoded by sensory systems modelled by the Bayesian hypothesis. We also describe the motivation of applying the Bayesian approach in the context of FCD. We then describe a formal definition of the Observer Model and its components. We present a novel characterization of extracellular fold change as required by the model. We evaluate in detail the perception of FCD by *Dictyostelium* cells as derived from the Observer Model against the extracellular fold change model. We also quantify the prediction of the fold change in stimulus by the Observer model. Finally we compute the fold change perceptual bias and fold change distinguishability threshold as characterized by the Observer model and examine whether a relation between these two properties exist.

6.2 The Bayesian Observer model

6.2.1 Motivation

Before we introduce the Bayesian Observer model and its components, we present here some background and key principles of the model that motivate us to apply the Bayesian approach to the sensory system of FCD. Human sensory systems such as vision and hearing are not perfect and therefore there are differences between the actual external stimulus and perceived stimulus encoded by our neurons. This amount of deviation of the perceived stimulus from the actual stimulus forms the bias of our perceptions. One explanation for the observed bias is that our perceptions are heavily influenced by our prior beliefs. An example is a kilogram of feathers and a kilogram of lead where the lead is perceived to be heavier even though both are of the same weight. Intuitively, the bias observed can be attributed to our internal belief or our prior knowledge that lead is heavier. However, biases in perceptions also work in the opposite direction of our expectations. An example is when comparing the weights of two objects of the same mass but of different heights where results showed that shorter objects are perceived heavier, creating a size-weight illusion (Usnadze, 1931) .

The Bayesian hypothesis suggests that our perception is a result of the sensory system trying to optimize the computation of the sensed stimulus combined with prior knowledge (Curry, 1972). A Bayesian model of perception would therefore consists of two main components; the prior and the likelihood.

Efficient encoding of the stimulus statistics

However, the Bayesian approach has been heavily criticised because of the inclusion of the prior and likelihood components and that they are often chosen arbitrarily or out of mathematical conveniences (Gelman et al., 2008). Wei and Stocker (2015) presented a Bayesian Observer model based on the efficient encoding hypothesis which constraints the priors and likelihoods. The efficient encoding hypothesis suggests that because of the limitation imposed by the neural resources, the firing of neurons (which collectively is the sensory representation of the stimulus) are optimized to the prior distribution of stimulus (Barlow, 1961). In the context of FCD, the responses of *Dictyostelium* cells is akin to the firing of neurons. Using the efficient coding hypothesis, if observing changes of two fold in the surrounding cAMP concentration is statistically likely, the population of cells would optimally represent the uncertainties of the external stimulus fold change $F = 2$ compared to other unlikely fold changes in stimulus cAMP.

Anti-Bayesian effect

As a result of imposing constraints on the priors and likelihood by the efficient encoding hypothesis, the Bayesian Observer model derived by Wei and Stocker (2015) suggests that perceptions are often subject to the anti-Bayesian effect. We illustrated the anti-Bayesian effect in the context of FCD in Figure 6.1. In Figure 6.1, the uncertainties of the external fold changes in stimulus is represented by the prior $P(F)$, the likelihood $P(I_p|F)$ is the sensory representation of stimulus fold F and the posterior $P(F|I_p)$ is the perception. If the estimated F derived from the perception is repelled from the prior, then the bias observed is anti-Bayesian. In this way, perceptions that are influenced more by the prior are deemed Bayesian and those that are repelled away from the prior are deemed anti-Bayesian. The problem of weights of lead and feathers given earlier is an example of a Bayesian perception while the size-weight illusion problem correspond to an anti-Bayesian perception.

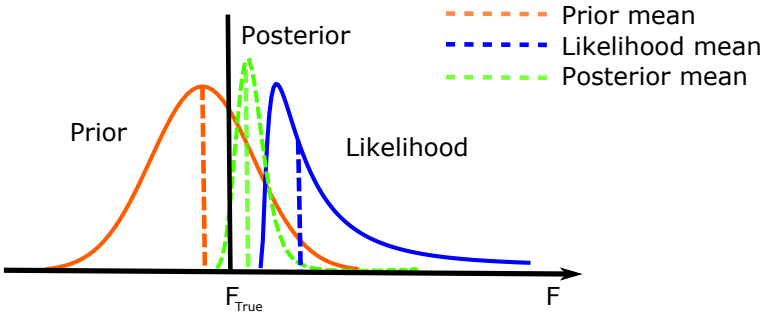

Figure 6.1: Illustration of the anti-Bayesian effect produced by the Bayesian model of perception (Wei and Stocker, 2015, 2012). Posterior estimate (mean) is biased away from the prior by the likelihood. Vertical black solid line represents the true value of stimulus denoted as F_{True}.

We ask whether it is possible to apply the Bayesian approach to model the perception of FCD by the population of (virtual) *Dictyostelium* cells. By casting the sensory system of FCD in this context, it is hoped that questions such as *What is the biases in the perceptions of FCD?* and *Does the biases also demonstrate anti-Bayesian effects?* can be addressed. The latter question has been partially addressed in the previous chapter where we showed that the inferred posterior exhibits anti-Bayesian effects.

6.2.2 Model components

In this section, we will see how the probability components derived in the previous chapter are used in modelling the cell's perception of fold change. The 'Observer Model' was proposed by Wei and Stocker (2015) as a model consisting of an encoding and a decoding mechanism to explain the possible computation of sensory information by cognitive systems. The model is illustrated in the context of FCD in Figure 6.2. The uncertainty in the extracellular stimulus fold $P(F)$ is encoded by the *Dictyostelium*

cells and represented internally by the sensory variable I_p as $P(I_p|F)$. The Bayesian decoding mechanism then incorporates the population of cells' own belief or prior about the uncertainty of the stimulus fold. The result is an estimation of F denoted as $\hat{F}$ which represents what the cells *perceive* the external fold to be. Some loss of information during both encoding and decoding process is inevitable as the model is assumed imperfect and subject to the influence of noise.

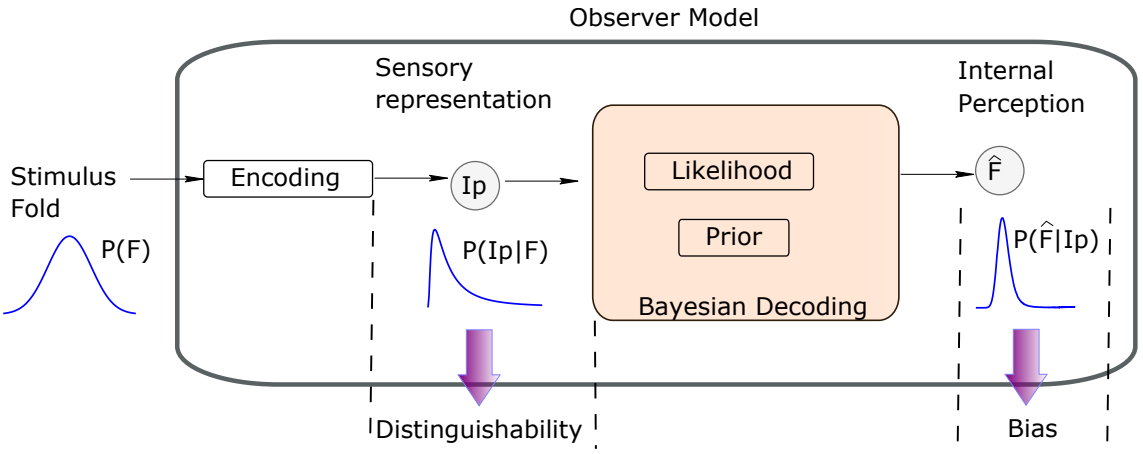

Figure 6.2: The Bayesian Observer Model by Wei and Stocker (2015)

Chapter 4 therefore can be considered as a characterization of the encoder and chapter 5 can be viewed as an attempt to model the decoder mechanism. The posterior probability of fold $P(F|I_p)$ inferred in chapter 5 then forms the 'internal perception' of fold change or what the population of virtual cells perceive the distribution of the extracellular stimulus fold to look like. Hereafter $P(F|I_p)$ is referred interchangeably as 'internal model' and 'internal perception'. The inferred posterior $P(F|I_p)$ is also referred interchangeably as $P(\hat{F}|I_p)$ when discussing in the context of posterior of estimates. What is yet to be characterized is the uncertainty of the extracellular fold change $P(F)$.

6.2.3 Bias and distinguishability threshold as measures of perception

Perception can be characterized by two measures; the perceptual bias and distinguishability threshold. As defined by Wei and Stocker (2017) and illustrated in Figure 6.3 in the context of FCD, perceptual bias is indicated by the amount of deviation of the perceived fold change F_{percept} from the actual stimulus F_{T}.

On the other hand, distinguishability or discriminability is indicated by the observer's ability to pick out minimal changes in the stimulus variable. In Figure 6.3, if the observer can tell the difference between perceptions, each differing by a small value of fold, then we would say that the distinguishability threshold is low.

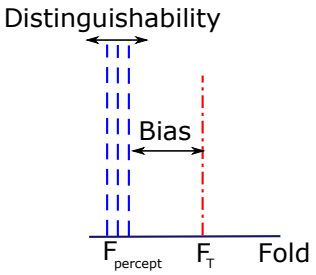

Figure 6.3: Definition of bias and distinguishability

By imposing constraints on the prior and likelihood using the efficient encoding, Wei and Stocker (2015) were able to derive a relation between between the prior distribution of stimulus $P(F)$ and the Fisher information $J(F)$ as

$$P(F) \propto \sqrt{J(F)} \tag{6.1}$$

If the likelihood of observing the sensory variable I_p given stimulus F is twice differentiable, then the Fisher information is defined as

$$J(F) = -\mathbb{E}\big[\big(\frac{d}{dF}\log f(I_p|F)\big)^2\big] \tag{6.2}$$

Further mathematical derivations by the same author in Wei and Stocker (2017) proved that the relation between perceptual bias $b(F)$ and the distinguishability threshold $D(F)$ is proportional

$$b(F) \propto (D(F)^2)' \tag{6.3}$$

We refer the reader to the paper by Wei and Stocker (2017) for detailed derivations of the bias-distingushability threshold relation as per equation above. We present only the significant assumptions asserted in the derivations in the context of FCD as below.

- The encoding is assumed to be efficient in the sense that mutual information between the sensory representation I_p and stimulus variable F (mutual information denoted as $I[I_p; F]$) is maximised. This entails that the conditional entropy is minimal where given an observed I_p, the uncertainty of the underlying F is reduced

$$I[I_p; F] = H(F) - H(F|I_p) \tag{6.4}$$

  where the entropy of $H(F|I_p)$ is approximated by the Fisher information $J(F)$.

- Mutual information I is constrained as $I[F, I_p] \leq I[F, \hat{F}]$

- The estimator $\hat{F}$ is assumed with variance $1/\sigma(\hat{F})$ by means of Cramer Rao can then be approximated by a gaussian with the same variance.
- The distribution of the sensory representation $P(I_p|F)$ is assumed to be gaussian distributed

We ask whether the relation of equation 6.3 holds true in the context of FCD as well. We have already characterized the distinguishability property in chapter 4 by looking at how much $P(I_p|F)$ overlaps. However, the distinguishability threshold and the perceptual bias are yet to be quantified and the relation between these two quantities in the context of FCD has yet to be examined.

6.3 Modelling the external fold change

In order to model the cell's perception of fold change, we characterize here the uncertainties of the extracellular stimulus fold, hereafter referred as the 'external model'. The distribution of cAMP by aggregating *Dictyostelium* cells was first visualized in the paper by Tomchik and Devreotes (1981) where a scheme for a travelling wave cAMP was suggested. Since then, various studies have proposed many models mainly focussed on describing the spiralling behaviour seen in Tomchik and Devreotes (1981). An example of such a study is the planar and spiralling cAMP wave model by Tyson and Murray (1989) based on the reaction-diffusion equation proposed earlier by Martiel and Goldbeter (1987). More often than not, models proposed involve detailed cellular attributes such as the surface area of cell, the rate of intracellular and extracellular cAMP, and the binding affinity of cAMP receptors (Monk and Othmer, 1989, 1990). Although the changes in concentration for a spiralling wave has been extensively studied, there is no such study that investigates the fold change in concentration of a propagated cAMP. Hence we derive here our own model using a statistical approach to describe how stationary cells would experience fold change as cAMP is being propagated. Note that this approach differs greatly to the dynamics of fold change modelled by the chemotaxis prior in chapter 5 where it is based upon movement of cells in a fixed linear cAMP gradient. We believe that the fold change modelled in this chapter would resemble the fold change found in the natural environment more.

6.3.1 Normal approximation of the total cAMP produced by a population

We assume that a single cell produces a cAMP concentration x. Due to cell-cell variability, different cells produce different amounts of cAMP. Hence x varies and we denote X as a random variable representing the amount of cAMP produced by a single cell. X

is randomly drawn from an unknown distribution of concentration cAMP with mean μ_{T} and standard deviation σ_{T}. Therefore a single cell on average is expected to produce μ_{T} amount of cAMP with some variance of σ_{T}. Suppose there are m populations of cells of a fixed size n with each cells in any population producing various amount of cAMP drawn from the unknown distribution. The total concentration produced by the k^{th} population is denoted as $\sum X_k$ where it is the sum of the cAMP produced by cells in the k_{th} population. The distribution of population sums is then derived by plotting $\sum X_k$ for all $k \in m$ populations. For such a distribution, the Central Limit Theorem for sums states that as the sample size n increases, the distribution of the total concentration $\sum X$ approximates the normal distribution such that

$$\sum X \sim \mathcal{N}(n\mu_{\mathrm{T}}, \sigma_{\mathrm{T}}\sqrt{n}) \tag{6.5}$$

Here, $n\mu_{\mathrm{T}}$ is the mean and $\sigma_{\mathrm{T}}\sqrt{n}$ is the standard deviation. As the number of cells in the population grows, a decrease in the standard deviation is expected. Hence the distribution of total cAMP produced by a population of cells can be approximated if we know μ_{T} and σ_{T} regardless of how stimulus cAMP is distributed.

6.3.2 Fold change as a ratio of two normals

Now we consider two populations of cells N_x, N_y where N_i indicates the number of cells in each population $i, i = \{x, y\}$. Specifically we consider N_y as the population of cells at the aggregation centre at time t_1. As more cells migrate to the centre, the population grows to N_x at time t_2 and therefore $N_x > N_y$. We denote X, Y as two random variables to represent the amount of cAMP produced by individual cells in each population and we assume X and Y are independent. The limitation of the independence assumption is acknowledged as a portion of cells in N_x also originates from N_y. Therefore there is a possibility that correlations exist between X and Y. However if we accept that the assumption is true, then using the Central Limit Theorem the total amount of cAMP produced by each population is drawn from two independent normal distribution of

$$\sum X \sim \mathcal{N}(\mu_x, \sigma_x) \tag{6.6}$$

$$\sum Y \sim \mathcal{N}(\mu_y, \sigma_y) \tag{6.7}$$

with mean of sums for population x and y denoted as μ_x and μ_y

$$\mu_x = N_x \mu_{\mathrm{T}} \tag{6.8}$$
$$\mu_y = N_y \mu_{\mathrm{T}} \tag{6.9}$$

Similarly the standard deviation of sums of population x and y are defined as

$$\sigma_x = \sigma_{\mathrm{T}} \sqrt{N_x} \tag{6.10}$$
$$\sigma_y = \sigma_{\mathrm{T}} \sqrt{N_y} \tag{6.11}$$

The fold change in concentration between the two population cells is then a ratio of the two independent normal random variables denoted as F where $F = X/Y$. In our case, both X and Y are always strictly positive due to the nature of the physical quantity that they represent. This means that the population of cells must have produce some amount of cAMP.

We briefly introduce previous studies on the distribution of ratio of two normals. In the paper by Marsaglia (1965) which later was revisited and extended in Marsaglia et al. (2006), it has been shown that the distribution of ratio of two normals can be linearly transformed and expressed in the terms of the standard normal. Díaz-Francés and Rubio (2013) presented a theoretical proof that the ratio can be approximated by a normal distribution when certain conditions on the coefficient are met. Both the density and distribution functions have complicated expressions (Marsaglia et al., 2006; Hinkley, 1969). Here we provide the density function of F as given by Díaz-Francés and Rubio (2013)

$$f_F(F; \mu_x, \mu_y, \sigma_x, \sigma_y, \delta_y) = \frac{(\sigma_y/\sigma_x)}{\pi(1 + (\sigma_y/\sigma_x)^2 F^2)} \exp\left(- \frac{((\sigma_y/\sigma_x)^2 (\mu_x/\mu_y)^2 + 1)}{2\delta_y^2} \right) \times \left\{ 1 + \sqrt{\frac{\pi}{2}} q \quad \mathrm{erf}\left(\frac{q}{2}\right) \exp\left(\frac{q^2}{2}\right) \right\} \tag{6.12}$$

where

$$q = \frac{(1 + (\mu_x/\mu_y)(\sigma_y/\sigma_x)^2 F)}{\delta_y \sqrt{1 + (\sigma_y/\sigma_x)^2 F^2}}$$

The density function is parameterised by the mean of sums μ_x, μ_y, standard deviation of sums σ_x, σ_y and coefficient of variance δ_y of Y. The means are of equation 6.8 and

equation 6.9 while the standard deviations are of equation 6.10 and equation 6.11. The parameters can be simplified by setting $\beta = \mu_x/\mu_y$ representing the ratio of means and $\rho = \sigma_y/\sigma_x$ as the ratio of standard deviations. β and ρ can be further expressed as

$$\begin{aligned} \beta &= \frac{N_x \mu_{\mathrm{T}}}{N_y \mu_{\mathrm{T}}} \\ &= \frac{N_x}{N_y} \end{aligned} \tag{6.13}$$

and

$$\begin{aligned} \rho &= \frac{\sigma_{\mathrm{T}} \sqrt{N_y}}{\sigma_{\mathrm{T}} \sqrt{N_x}} \\ &= \sqrt{\frac{N_y}{N_x}} \end{aligned} \tag{6.14}$$

where as we can see both β and ρ are only dependent on the ratio of the population size. On the other hand if we expand δ_y by substituting equation 6.9 and equation 6.11

$$\begin{aligned} \delta_y &= \frac{\sigma_y}{\mu_y} \\ &= \frac{\sigma_{\mathrm{T}}}{\mu_{\mathrm{T}}} \frac{\sqrt{N_y}}{N_y} \\ &= \delta_{\mathrm{T}} \frac{\sqrt{N_y}}{N_y} \end{aligned} \tag{6.15}$$

it is found that δ_y is dependant on δ_{T} and the size of population y. δ_{T} is the coefficient of variance of the concentration of cAMP which is assumed to be unknown. Among the properties of $f_F(.)$ is that it is heavy tailed, has no finite moments and its shape is primarily determined by δ_y. Studies have come up with different bounds on the values of δ_y and δ_x as listed in table 6.1 where $f_F(.)$ can be approximated by the normal distribution. The rule of thumb is to keep δ_y as small as possible in order to achieve a good approximation.

Because many of the parameters are ratios or combinations of other parameters, the essential element boils down to only three parameters which are $\mu_{\mathrm{T}}, \sigma_{\mathrm{T}}$ and Ny. These are also the parameters that makes up δ_y. To demonstrate the changes in the landscape of the density function, we computed f_F for different values of $\mu_{\mathrm{T}}, \sigma_{\mathrm{T}}, Ny$ with β fixed as $\beta = 3$. The result is shown in Figure 6.4A,B and C. Results of $f_F(.)$ for different β is shown in Figure 6.4D for reference. It can be seen from Figure 6.4A,B and C that

Table 6.1: Different constraint on the values of δ_y and δ_x to enable approximation of $f_F(.)$ by the normal distribution.

Author	Constraints
Geary (1930)	$\delta_y \leq 1/3$
Hayya et al. (1975)	$\delta_y \leq 0.09, \delta_x \geq 0.19$
Kuethe et al. (2000)	$\delta_y \leq 0.1$
Marsaglia et al. (2006)	$\delta_y \leq 0.25, \delta_x \geq 0.443$

a smaller δ_y can be achieved by either increasing μ_T and Ny or by decreasing σ_T. As expected, smaller δ_y results in a density curve that is sharper and narrower. Figure 6.4D shows that as the ratio of the means β increases, the density curve becomes more right tailed with a larger standard deviation. Therefore if there is a large increase in the number of cells from the initial population N_y to N_x, there is more uncertainty in the resulting fold distribution. The right tailed property entails that the distribution is always more biased towards smaller fold and the chance of observing larger fold increases as β increases although it still remains highly unlikely.

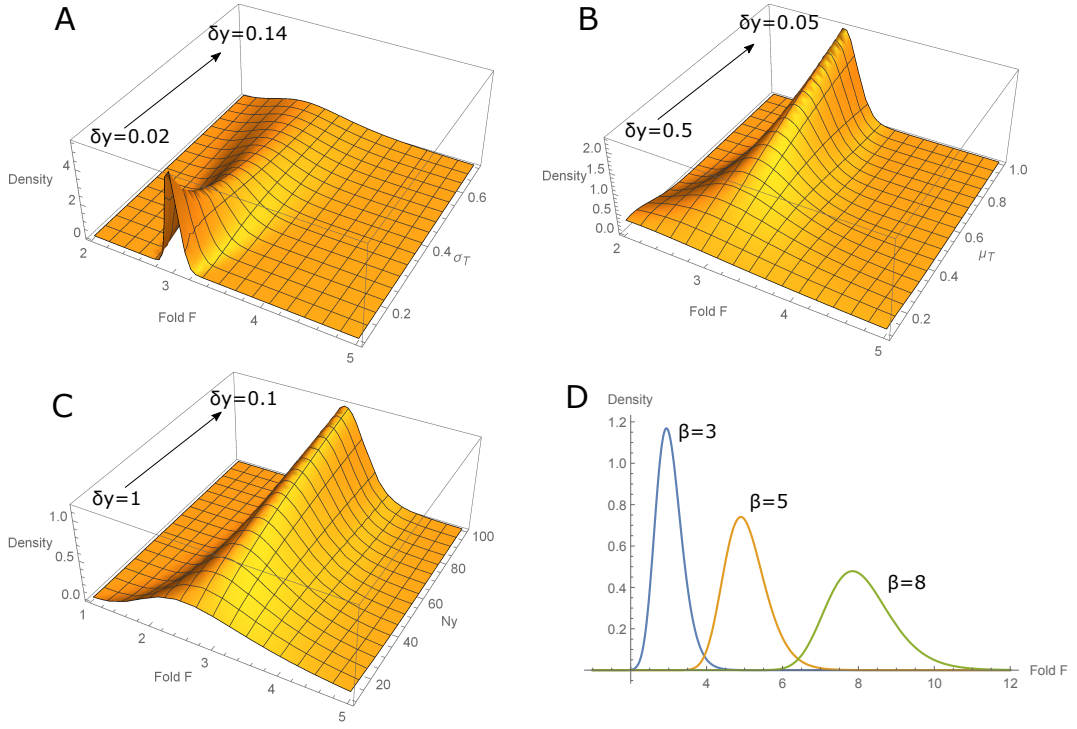

Figure 6.4: Dynamics of the density function f_F when its parameters are varied. The parameters when not varied are fixed as $\mu_T = 0.5, \sigma_T = 0.5, N_y = 100$. Arrows shown to indicate how δ_y changes when the parameter of interest is increased. Due to the complexity of the density function, computation is done with the help of Mathematica file provided by Weisstein (2003).

In the following sections, with the exception of $\beta = \mu_x/\mu_y$ all other parameters of the density function will be assigned values and treated as constants for simplicity purposes.

Therefore the density function of external fold change $f_F(F;\beta)$ is parameterised by a single parameter β.

6.3.3 External Fold model has similar characteristics with Internal Fold despite modelled independently.

The probability of the extracellular stimulus fold is then solved for all β in $\mathbf{B} = (1.1, 1.2, \ldots, 100)$ by integrating the density function of equation 6.12

$$P(F \in F \pm \delta_F|\beta; \mu_{\mathrm{T}}, \sigma_{\mathrm{T}}, N_y) = \int_{F-\delta_F}^{F+\delta_F} f_F(F; \mu_x, \mu_y, \sigma_x, \sigma_y, \delta_y)dF \tag{6.16}$$

where its parameters are fixed as $\mu_{\mathrm{T}} = 2.0, \sigma_{\mathrm{T}} = 1.5, N_y = 100$. In the following sections, $P(F \in F \pm \delta_F|\beta; \mu_{\mathrm{T}}, \sigma_{\mathrm{T}}, N_y)$ is denoted as $P(F|\beta)$ for brevity. For $\beta = 1.1$, $F < 1$ is possible if the total amount of cAMP produced by population N_x cells is less than what population of N_y cells produced although $F \geq 0$ is still true in any scenario. The sample result of the probability distributions conditioned on $\beta = 1.1, 2.1, \ldots, 9.1$ is shown in Figure 6.5. We refer to the conditional probability distribution of fold $P(F|\beta)$ derived here as the **External Model** to contrast the internal model $P(F|Ip)$ derived in chapter 5. While the external model represents the uncertainty of the fold change found in the natural environment, the internal model correspond to the internal belief or perception of the *Dictyostelium* cells regarding the state of the extracellular fold given an internal response I_p.

Given that the parameters $\mu_{\mathrm{T}}, \sigma_{\mathrm{T}}$ and N_y are fixed, the external model can be viewed as the probability of fold conditioned only on ratio of means β, $P(F|\beta)$. β in essence is the expected fold change upon a level of cell aggregation. Figure 6.5 where $P(F|\beta = 2.1)$ shows that when the expected fold is low, the likelihood of the expected fold is so dominant that it is quite unlikely to observe other nearby fold. However this likelihood becomes more similar with other nearby folds as β increases as shown by the distribution of $P(F|\beta = 9.1)$.

Surprisingly the external fold change modelled here has similar characteristics as the internal model. The external model approximates the fold change in cAMP produced by two populations of cells using the Central Limit Theorem. On the other hand, the internal model takes into account intricate biochemical model fitted to experiment data. In spite of the contrasting approach, both models are right tailed with bias towards lower fold change. As the conditioned β in $P(F|\beta)$ of the external model increases, the positive skewness of the distribution also increases. This behaviour is similar to when I_p of $P(F|I_p)$ increases in the same manner.

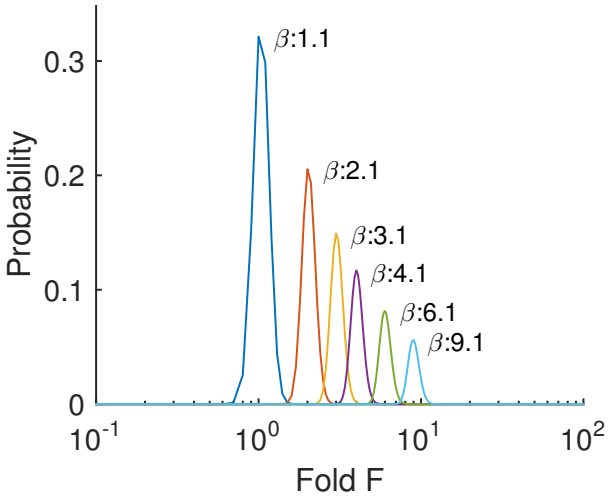

Figure 6.5: External model of Fold Change $P(F|\beta)$ derived by integrating equation 6.12. Parameters are set as $\mu_T = 0.5, \sigma_T = 0.1, N_y = 100$. Only sample results are shown for readability purposes.

6.3.4 External model is valid regardless of location by means of the cAMP diffussion-degradation model.

So far we have modelled the extracellular fold based on the amount of cAMP produced by two population of cells found at the aggregation centre. In this section we provide further arguments and justifications as to why the external model is valid even outside the aggregation centre. We know from literature that cAMP produced at the aggregation centre is then propagated outwards in the form of spiralling wave in order to guide the chemotaxis of cells far away. We ask how does the fold change propagated behave at some distance L from the centre? If the fold change produced by the two populations is $F = 4$, would the magnitude of the fold change propagated be reduced such that $F = 2$ at L? We can describe the diffusion of cAMP molecules produced by a population of cells at the aggregation center with a two-dimensional diffusion equation as

$$\frac{\partial C}{\partial t} = D\left(\frac{\partial^2 C}{\partial x^2} + \frac{\partial^2 C}{\partial y^2}\right)$$

where $C(x, y, t)$ is the cAMP concentration, D is the diffusion constant, x, y are the cartesian coordinates and t is the time variable. The solution to the partial differential equation above gives us a normalized gaussian function

$$C(r, t) = \frac{1}{4\pi Dt}\exp\left(\frac{-r^2}{4Dt}\right)$$

where r is the radial coordinate. This indicates that the diffused cAMP is independent of direction and what counts is the actual distance from the source. However, we know

that *Dictyostelium* cells also secrete cyclic nucleotide phosphodiesterase (PDE)(Sucgang et al., 1997) to degrade the cAMP in the environment. Considering both the effect of PDE and the independence of direction, the extracellular cAMP dynamics can be modelled with a one dimensional diffusion-degradation equation as

$$\frac{\partial C(x,t)}{\partial t} = D\frac{\partial^2 C(x,t)}{\partial x^2} - \alpha C(x,t)$$

where α is the cAMP degradation rate by PDE. The distance from cAMP source is represented by variable x. If the production of cAMP at the aggregation centre is stable and reaches the state of equilibrium where there are no changes in cAMP with respect to time, the equation above can be solved as

$$C(x) = C_0 \exp\left(\frac{-x}{\sqrt{D/\alpha}}\right)$$

where C_0 is the initial concentration at the centre. The level of cAMP concentration is therefore simplified by elimination of both time and direction variables. Now let us again consider the population of N_y cells at the aggregation centre that is producing a stable flow cAMP where we assume the amount of cAMP is dependent only on the number of cells. The level of cAMP is then governed by

$$C_{N_y}(L) = C_0 \exp\left(\frac{-L}{\sqrt{D/\alpha}}\right)$$

To avoid confusion with population of cells N_x, we denote L as the distance variable from the source. The initial concentration at the aggregation centre ($L = 0$) is C_0. The population of cells then grows to N_x and similarly

$$C_{N_x}(L) = C_0' \exp\left(\frac{-L}{\sqrt{D/\alpha}}\right)$$

producing a consistent cAMP level of C_0'. The transition time between C_0 to C_0' is assumed to be brief enough such that it is negligible. Both population are further assumed to have the same diffusion and degradation rate of $\mathcal{D}$ and α. The fold change F in concentration at location L is then derived as

$$\begin{aligned} F &= \frac{C_{N_x}(L)}{C_{N_y}(L)} \\ &= \frac{C_0'}{C_0}\exp\left(\frac{-L+L}{\sqrt{D/\alpha}}\right) \\ &= \frac{C_0'}{C_0} \end{aligned}$$

where using the probabilistic approach derived earlier, both C_0 and C_0' are drawn from two independent normal distributions. Hence, a stationary *Dictyostelium* cell which experiences a sudden rise in the surrounding level of cAMP would sense the same fold change regardless of its distance nor direction from the aggregation centre. The possibility of this scenario is largely supported by the the same constants D and α that govern the cAMP dynamics of the two populations. The sole dependency of fold change on the ratio of the initial concentration is equivalent to being dependent only on the ratio of the number of cells in population N_x and N_y. Therefore the external model is also valid outside the aggregation centre.

6.4 Matching External and Internal fold model

As we have derived a model for the external fold change, we continue evaluating the FCD accuracy by comparing the external model to the internal model. As stated in the introduction, the external model represents the state of extracellular fold change while the internal model is what the cells perceive the extracellular fold to be. If *Dictyostelium* cells sense with 100% accuracy then we would expect that when a certain $I_p = a$ is observed, the resulting distribution of fold $P(F|I_p = a)$ overlaps and matches perfectly with the external model with a certain $\beta = b, P(F|\beta = b)$ i.e, what the cells perceive is exactly the same with what the state of the world is. However as we will see this is not necessarily the case. We can view the discrepancy between the two models as a result of the cell's (possibly) imperfect sensing mechanism trying to optimally sense fold change amidst biological noise (both extrinsic and intrinsic) combined with the stimulus statistics that it has computed over time.

To quantify how much this perception deviates from the externally set of distribution of fold changes, we compute the Kullback-Leibler divergence (Kullback and Leibler, 1951) between the two models. This method would also be used to understand how the divergence of the external distribution constructed above from the internal model $P(F|I_p)$ changes the internal model $P(F|I_p)$, when different priors are used or when the background dependency $P(F|I_p, x)$ is considered. The Kullback-Leibler Divergence between two probability distributions P and Q is given as

$$D_{\mathrm{KL}}(P||Q) = \sum_i P(i)\log\frac{P(i)}{Q(i)}$$

where $P(i)$ and $Q(i)$ are the probability values at i for each respective distribution. The sum operation applies as we are handling discrete values of probability. Note that the divergence is asymmetric and therefore $D_{\mathrm{KL}}(P||Q) \neq D_{\mathrm{KL}}(Q||P)$. If the divergence equation is expressed as

$$D_{\mathrm{KL}}(P||Q) = \sum_i P(i)\log P(i) - \sum_i P(i)\log Q(i)$$

then we can see that the first term on the right side of the equation is the negative entropy of the P distribution. The entropy is reduced only when Q overlaps P at i. In our case P and Q represents the external and internal model respectively. The above equation can be rewritten in terms of the external and internal model as

$$D_{\mathrm{KL}}(P(F|\beta)||P(F|I_p)) = \sum_F P(F|\beta)\log\frac{P(F|\beta)}{P(F|I_p)}$$

Note that the base of the comparison is the external model $P = P(F|\beta)$. A low divergence score indicates that the internal model is more similar and closer to the compared external model. Hence in such case, we consider the internal perception to be of high accuracy. Otherwise when the D_{KL} score is high, the perception is deemed of low accuracy.

6.4.1 A simple example

Before we proceed to evaluate the divergence between the full range of our external $P(F|\beta), \beta \in \mathbf{B}, \mathbf{B} = (1.1, 1.2, \ldots, 100)$ and internal model $P(F|I_p), I_p \in \mathbf{I_p}, \mathbf{I_p} = (0.14, 0.15, \ldots, 1.14)$, we first demonstrate here the Kullback-Leibler divergence result between $P(F|\beta = 2)$ and $P(F|I_p)$. The objective is to show the overlapping behaviour of the two models as I_p, the internal response increases. The divergence is expressed as

$$D_{\mathrm{KL}}(P(F|\beta = 2)||P(F|I_p)) = \sum_{\forall j \in \mathbf{F}} P(F = j|\beta = 2)\log\left(\frac{P(F = j|\beta = 2)}{P(F = j|I_p)}\right)$$

and solved for all $I_p \in \mathbf{I_p}$. The internal model compared in this example is the uniform prior based posterior ($P(F) = \text{uniform}$). The result is shown in Figure 6.6A. As can be seen from the figure, the two models becomes more similar as I_p increases in the range of $I_p = 0.1$ to $I_p = 0.24$ indicated by the decrease in the D_{KL}. The internal model that is

most similar to the external model of $P(F|\beta = 2)$ is the distribution of $P(F|I_p = 0.24)$ with the minimum score of $D_{\mathrm{KL}} = 0.09563$. Hence when the external state is given by the distribution of $P(F|\beta = 2)$, population cells with internal model of $P(F|I_p = 0.24)$ perceives the external state most accurately.

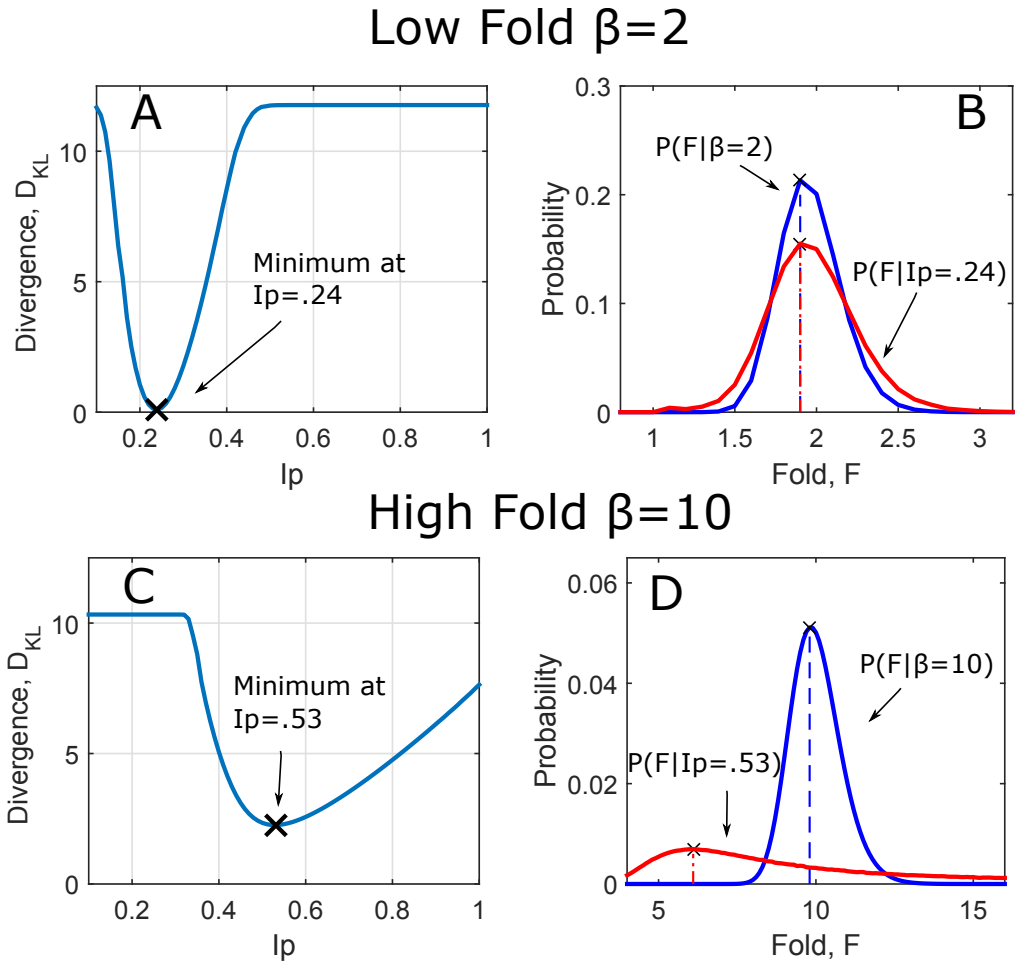

Figure 6.6: Kullback-Leibler Divergences between $P(F|\beta), \beta = 2, 10$ and $P(F|I_p), I_p = 0.1, 0.11, \ldots, 1$. The result for $P(F|\beta = 2)$ is shown in (A) with the most similar models visualized in (B). Likewise the result for $P(F|\beta = 10)$ is shown in (C) and the most similar models are visualized in (D).

To visualize how the most similar models overlap each other, we plotted the distribution of $P(F|\beta = 2)$ and $P(F|I_p = 0.24)$ as blue and red curves respectively in Figure 6.6B. As we can see, the external and internal almost completely overlap each other, hence the very low divergence score. Both models have the same peak at $F^* = 1.9$ indicated by the overlapping vertical blue and red dashed lines. When I_p increases such that $I_p > 0.24$, the corresponding distribution $P(F|I_p)$ shifts away from the external $P(F|\beta = 2)$ to the right, leading to more divergence. The divergence or separation is complete when $P(F|I_p = 0.54)$ as indicated by the maximum divergence score reached in Figure 6.6A.

How would the overlapping behaviour changes when the external model is of a a higher β? To answer this we also computed the divergence $P(F|\beta = 10)$ against $P(F|I_p), \forall I_p \in$

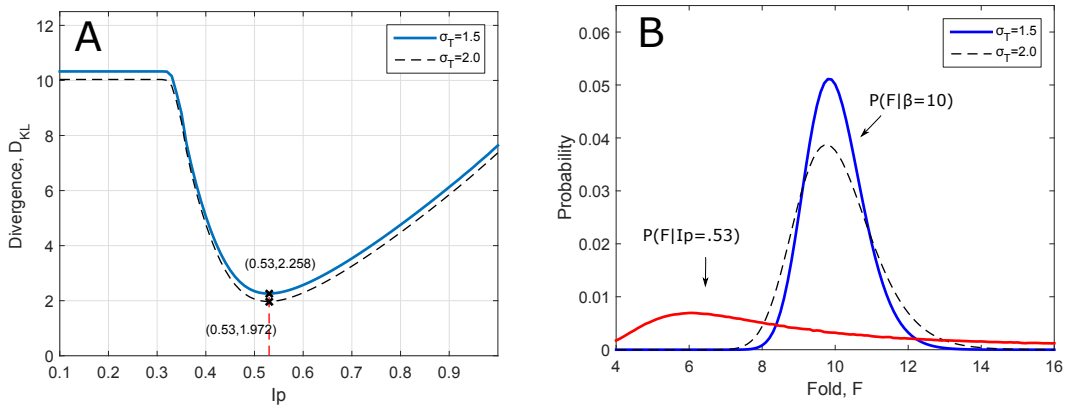

Figure 6.7: The effect of changing parameter σ_{T} on the Kullback-Leibler Divergences between $P(F|\beta = 10)$ and $P(F|I_p), I_p = 0.1, 0.11, \ldots, 1$. The internal is computed from the uniform prior.

$\mathbf{I_p}$. The result is shown in Figure 6.6C. A quick glance of the figure reveals that the overlapping behaviour is similar to when $P(F|\beta = 2)$ except that there is no clear separation reached between the two models even as I_p increases to $I_p = 1$. The divergence reaches its minimum at $P(F|I_p = 0.53)$ with $D_{\mathrm{KL}} = 2.258$. Note that the minimum score here is larger than when $P(F|\beta = 2)$. Therefore the accuracy of perception by the population of cells given that the extracellular state is characterized by $P(F|\beta = 10)$ is relatively lower than when $P(F|\beta = 2)$.

As before, we plotted the distributions curves of the most similar models in Figure 6.6D. We found that the peaks or mode of the distribution do not overlap as when $P(F|\beta = 2)$. If we compare to Figure 6.6C with Figure 6.6A, it can be seen that the rate at which models becomes more dissimilar is also much slower. This is due to external models with large β tends to overlap the right tail of the internal as in Figure 6.6D. Thus a short conclusion that can be made here is that internal models perceive more accurately external models conditioned on low β. As the compared β of the external model increases, the divergence is greater.

Before we compute the divergence for the full range of $\beta \in \mathbf{B}$, we ask what happens if the parameters $\mu_{\mathrm{T}}, \sigma_{\mathrm{T}}$ and N_y of the external model are varied and how would it effect the divergence? We can change any one of the three parameters and achieve the same effect because we would eventually be tuning δ_y. Therefore here we varied σ_{T} and analysed the computed divergence for $D_{\mathrm{KL}}(P(F|\beta = 10; \sigma_{\mathrm{T}} = 1.5)||P(F|I_p))$ and $D_{\mathrm{KL}}(P(F|\beta = 10; \sigma_{\mathrm{T}} = 2.0)||P(F|I_p))$ for all $I_p \in \mathbf{I_p}$.

The result is shown in Figure 6.7A. As we can see, increasing σ_{T} and thus flattening the distribution curve of $P(F|\beta)$ yields a lower minimum score of $D_{\mathrm{KL}} = 1.972$. Figure 6.7B illustrates how the external models in solid blue and black dashed lines become closer to the internal model as μ_{T} increases. However, $D_{\mathrm{KL}} = 1.972$ is the smallest divergence

that can be achieved by changing σ_{T} due to the constraint $\delta_T \leq 1$ that we imposed on the external model.

6.4.2 Results for all β and Ip

Continuing our analysis, here we investigate the Kullback-Leibler divergence when β of $P(F|\beta)$ is varied. Specifically we computed $D_{\mathrm{KL}}(P(F|\beta)||P(F|I_p))$ for all $\beta \in \mathbf{B}$ and $I_p \in \mathbf{I_p}$ and for all type of priors. To understand the effects of two parameters β and I_p, we first study the resulting Kullback-Leibler divergence visualized in a 3D landscape as shown in Figure 6.8.

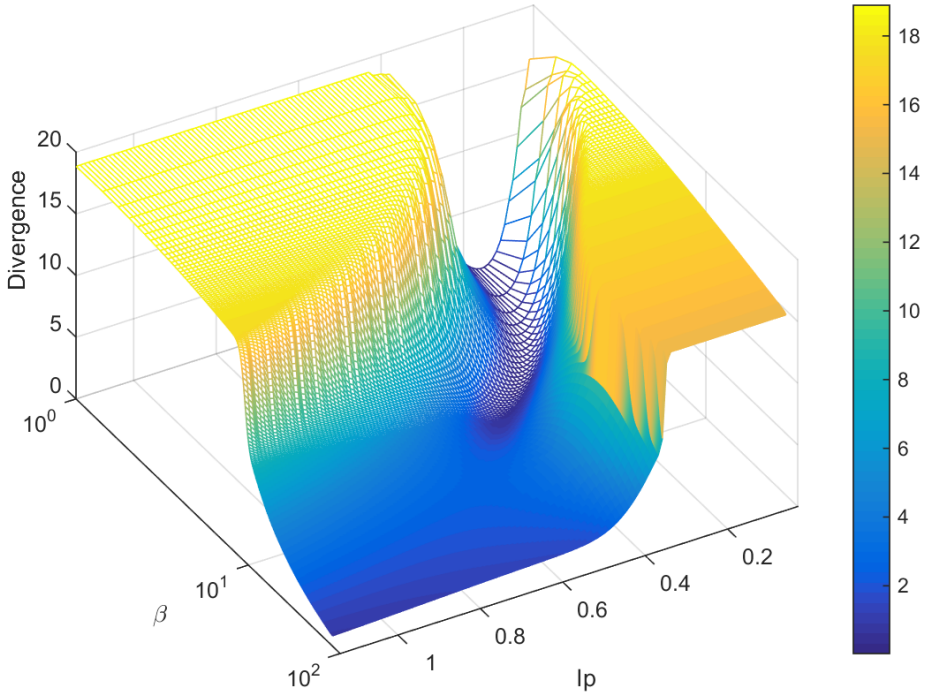

Figure 6.8: Kullback-Leibler Divergence $D_{\mathrm{KL}}(P(F|\beta)||P(F|I_p))$ for all $I_p \in \mathbf{I_p}, \beta \in \mathbf{F}$ and $F \in \mathbf{F}$. The $P(F|I_p)$ compared is the uniform prior based model.

Note that the $P(F|I_p)$ compared in Figure 6.8 is also of the uniform prior based model. From Figure 6.8, a valley can be observed where its lowest point indicates the region where the divergences are minimal and the two models are most similar. For small values of β, there exist a small range of I_p when conditioned upon give rise to internal models similar to the compared external model, hence the observed narrow valley. The existence of plateaus on both sides of the valley shows a clear separation between the two models compared.

However, the width of the valley widens as the compared β of the external increases. As β and I_p both reaches approximately $\beta \geq 10, I_p \geq 0.5$, the plateau on one side diminishes and the valley flattens out. This indicate that within the range of $\beta \geq 10, I_p \geq 0.5$, the external model is relatively similar to all internal models regardless of the I_p that the internal is conditioned upon. Does this mean that within this range, all internal models perceive the compared external fold changes accurately? To answer this question, we plotted the external and internal distribution parameterised by $\beta = 20, 50$ and $I_p = 0.6, 0.8, 1.0$ shown as Figure 6.9. One of the reason for the flat region is the significant decrease in the probability value as β increases from $\beta = 20$ to $\beta = 50$ which then contributes to a lower divergence score. Moreover the external for $\beta \geq 10$ overlaps only the right tail of the internal model regardless of the conditioned I_p. Due to the probability in the right tail region remains largely unchanged, the resulting divergence scores are kept low and does not vary much. Therefore it would be misleading to say that the low divergence score observed in the flat region in Figure 6.8 indicates that the accuracy of the internal perception is high.

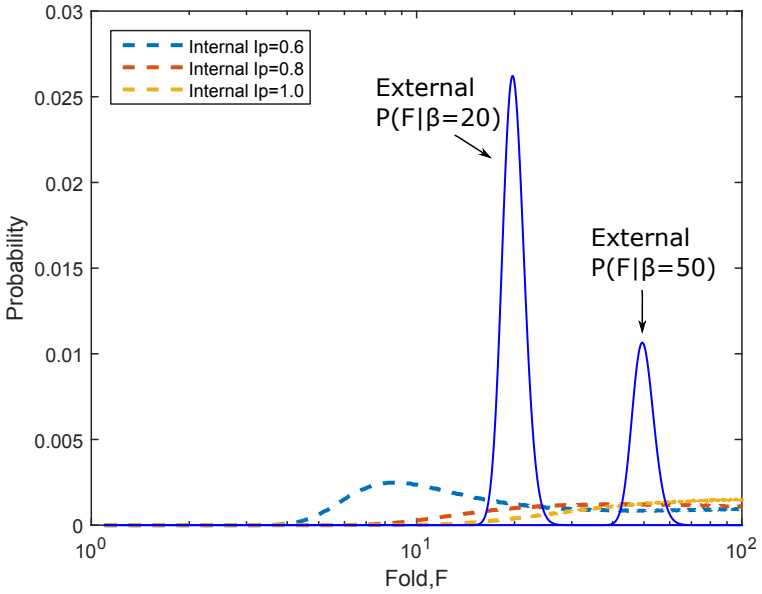

Figure 6.9: Comparison between the probability distribution curves of the external model $P(F|\beta), \beta = 20, 50)$ and internal model $P(F|I_p), I_p = (0.6, 0.8, 1.0)$ demonstrates how overlaps in region of $\beta \geq 10, I_p \geq 0.5$ leads to lower divergence scores and the flat surface observed in Figure 6.8. All internal models are uniform prior based. Solid blue line indicates the external model and dashed curves are the internal conditioned on various I_p.

6.4.3 Effects of priors

To see the effects of internal models with different priors, we plotted the Kullback-Leibler divergence landscape shown as Figure 6.10. For readability and contrasting purposes

the landscapes are visualized as contours. We also truncated the result to ignore some part of the insignificant flat region. As can be seen, the contours for all priors share the same characteristics of having a narrow valley initially which widens as β increases. All type of priors also have flat regions in the range of approximately $\beta \geq 10, I_p \geq 0.5$. Therefore we can further add to the previous conclusion that regardless of the type of priors, the Kullback-Leibler divergence is an inappropriate measure of accuracy of the internal perception in the region of $\beta \geq 10$ and $I_p \geq 0.5$.

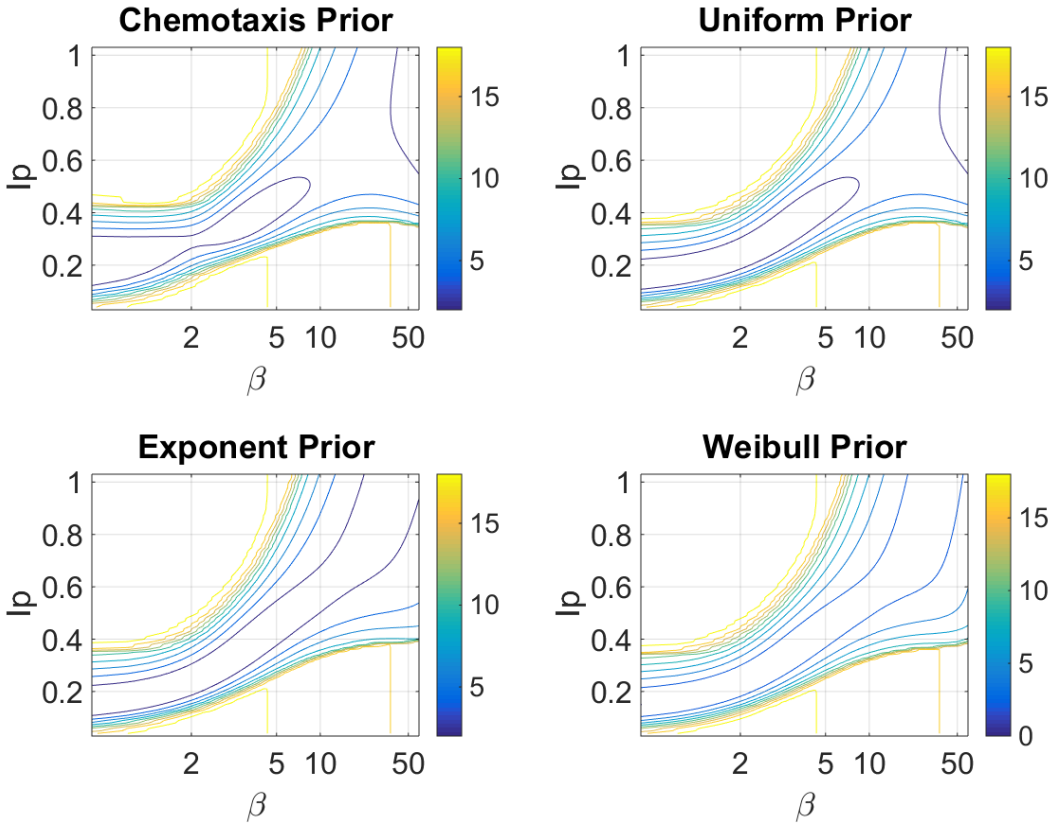

Figure 6.10: The effect of internal models with different priors on the Kullback-Leibler Divergence.

One point that stands out in Figure 6.10 is that the divergence computed with chemotaxis prior based internal model has a very narrow valley, almost bottleneck like at (β, I_p) coordinate of $(2, 0.27)$ and $(2, 0.31)$. It is also observed that the contour for the exponent and Weibull prior based internal are almost similar to each other. To gain more insights on the effect of different priors, we extracted the minimum points of the valley for each landscape. For a range of external $P(F|\beta), \beta \in \mathbf{B}$, internal models based on a certain type of prior would have a set of $I_p^*(\beta) = (a_1, a_2, \ldots, a_N)$ that when are conditioned upon produce $P(F|I_p)$ most similar to the compared external. Thus, $P(F|I_p), I_p \in I_p^*$ represents most accurate perception on the entire range of external $P(F|\beta), \beta \in \mathbf{B}$. Intuitively, if the type of priors plays any role in determining the amount of divergence, internal models based on a different prior would have a different set of I_p^* and consequently, a different set of minimum divergence scores as well.

In order to determine $I_p^*(\beta)$, we treated the divergence landscape result as a function of I_p and β denoted as $D(I_p, \beta) = D_{\mathrm{KL}}(P(F|\beta)||P(F|I_p)))$, for all $I_p \in \mathbf{I_p}$ and $\beta \in \mathbf{B}$. For a given β we then find

$$I_p^*(\beta) = \underset{I_p}{\operatorname{argmin}}\, D(I_p, \beta) \tag{6.17}$$

Subsequently the corresponding minimum divergence score for $I_p^*(\beta)$ denoted as $D_{min}(\beta)$ is then derived as

$$D_{min}(\beta) = \min D(I_p; \beta) \tag{6.18}$$

and is found for all $\beta \in \mathbf{B}$. The range of $\mathbf{B}$ here is chosen as $\mathbf{B} = (1.4, 1.5, \ldots, 10)$ because this is the range where the computed divergence result is considered as a suitable measure of the internal perception's accuracy. We plotted the curves of $I_p^*(\beta)$ and $D_{min}(\beta)$ for different type of priors in Figure 6.11A and Figure 6.11B respectively. Figure 6.11A answers the question *'For a particular prior based internal model, which I_p when conditioned upon produces $P(F|I_p)$ that matches most with the compared external $P(F|\beta)$?'*. The corresponding Figure 6.11B then provides the answer for *'If $P(F|I_p = a)$ is found to match most with $P(F|\beta = b)$, what would the minimum score be?'*. Figure 6.11A shows that the set of I_p^* derived by internal models with uniform, exponent or Weibull prior are similar in the range of $\beta = 1.14$ to $\beta = 4$. Hence in this range internal models based on the mentioned three priors share a similar perception of the external state. Only the chemotaxis prior based internal provides a different set of I_p^* and therefore perceives the external state differently. For the case when the external state is determined by $\beta > 4$, the perception varies among different priors albeit the chemotaxis and uniform prior based perception are exactly the same.

Figure 6.11B tells us the accuracy of the perception in Figure 6.11A. With the exception of the chemotaxis prior, in general perceptions are of high accuracy across all priors when the compared external has a very low β as shown by the low D_{min} score. The accuracy of perception then deteriorates as β increases. However, the chemotaxis prior based internal tells a slightly different story. If we analyse the blue line trajectory in Figure 6.11B, we can see that the chemotaxis prior based has two regions where the accuracy of perception is relatively high. The first is for $\beta < 1.6$ and second is when $2.8 \leq \beta < 4$. The accuracy of the perception temporarily worsens at a considerably high rate in the range of $1.6 \leq \beta < 2.8$. We can see here the strong effect of the chemotaxis prior in determining the perception of the internal model. The perception then continues to resembles the uniform prior based for $\beta > 4$ and deteriorates as β increases.

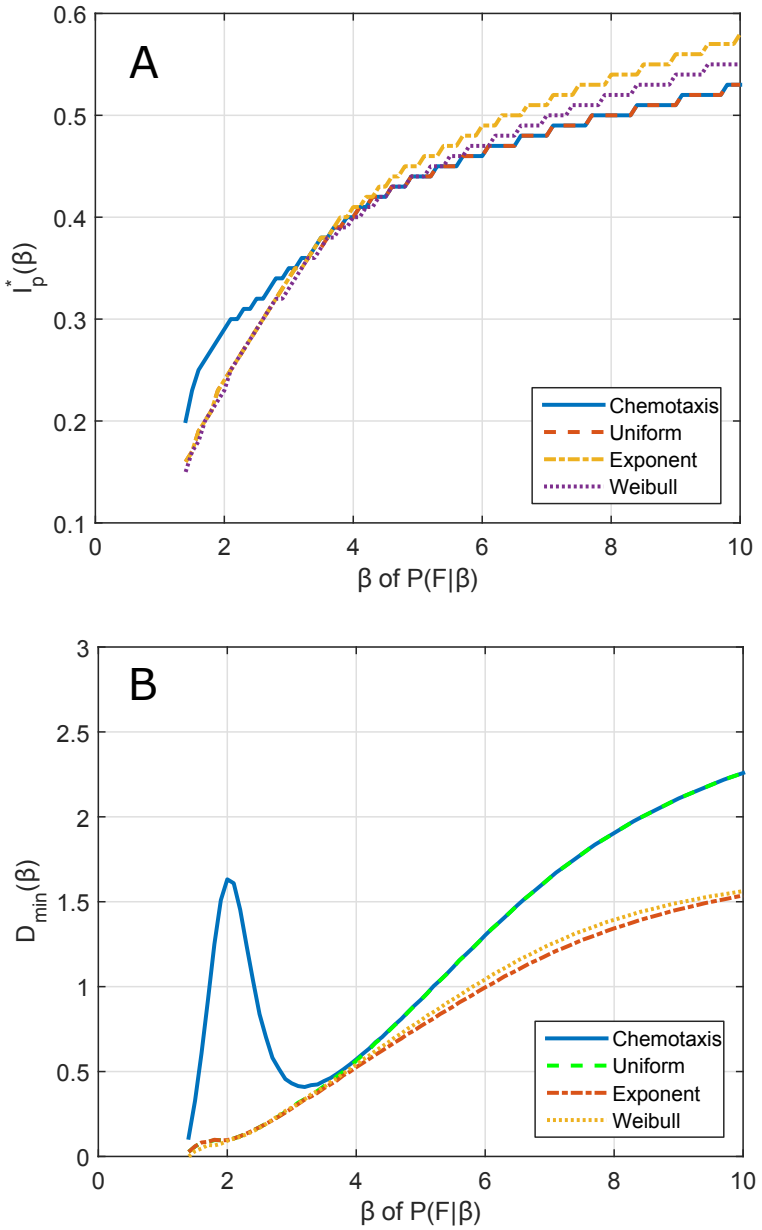

Figure 6.11: The effect of priors on the minimum divergence score. (A) I_p that must be conditioned upon to derive internal model that best match the compared external given by β. (B) The corresponding divergence score for (A).

6.4.4 Effects of background dependency

We have seen the effects of internal models computed from different priors on the accuracy of perception as quantified by the minimum divergence score. As shown in the previous chapter, the internal model of posterior fold can also be conditioned on both I_p

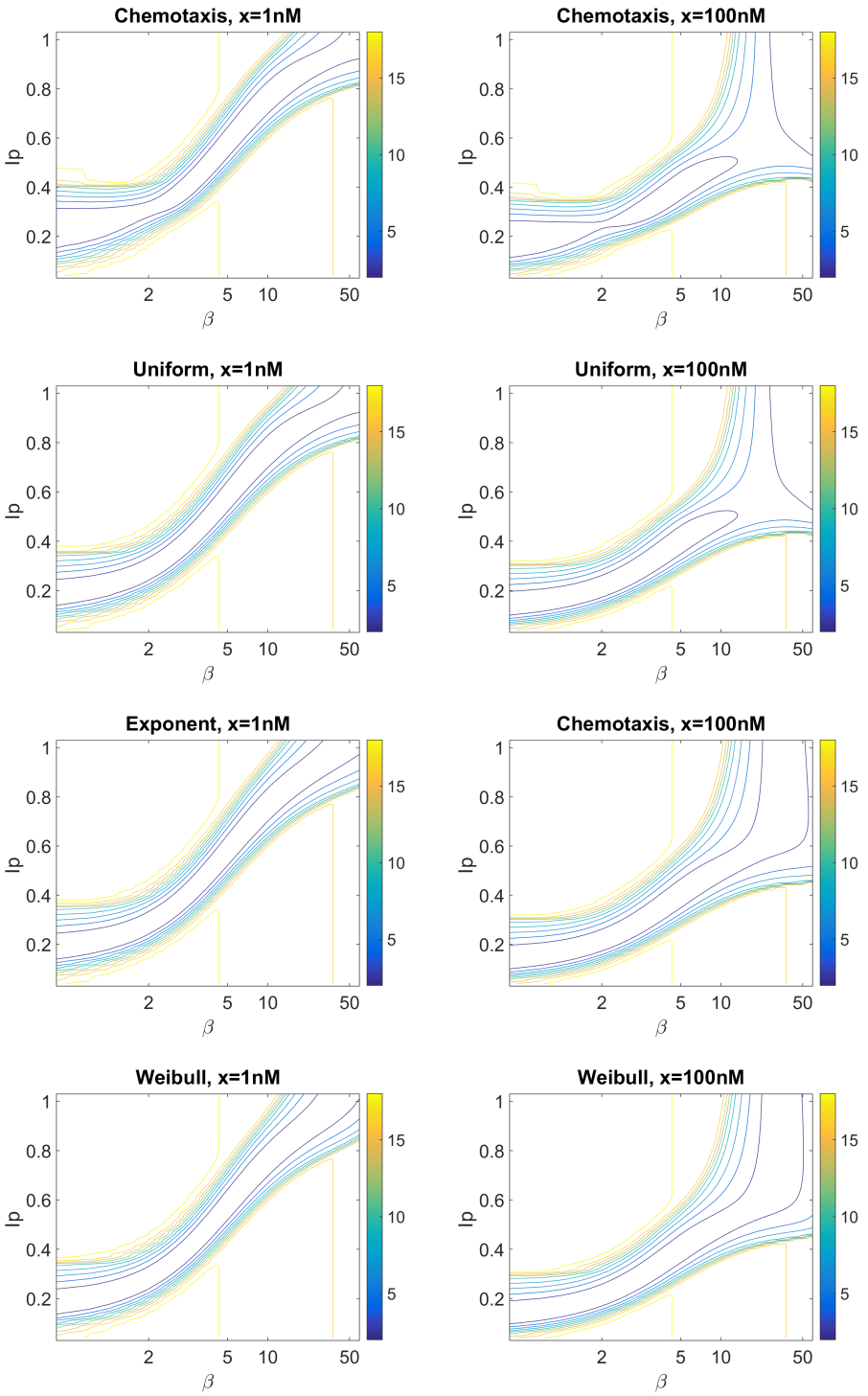

Figure 6.12: Kullback-Leibler Divergence landscape for different prior based internal with background dependencies.

and background cAMP x denoted as $P(F|I_p, x)$. How would background cAMP affect the divergence between the two models? We computed $D_{\mathrm{KL}}(P(F|\beta)||P(F|I_p, x))$ for all $\beta \in \mathbf{B}$, $I_p \in \mathbf{I_p}$ and for $x = 1, 100$. The divergence is computed for all types of priors.

The x values are deliberately chosen such that the comparison is done between a weak and a strong background cAMP.

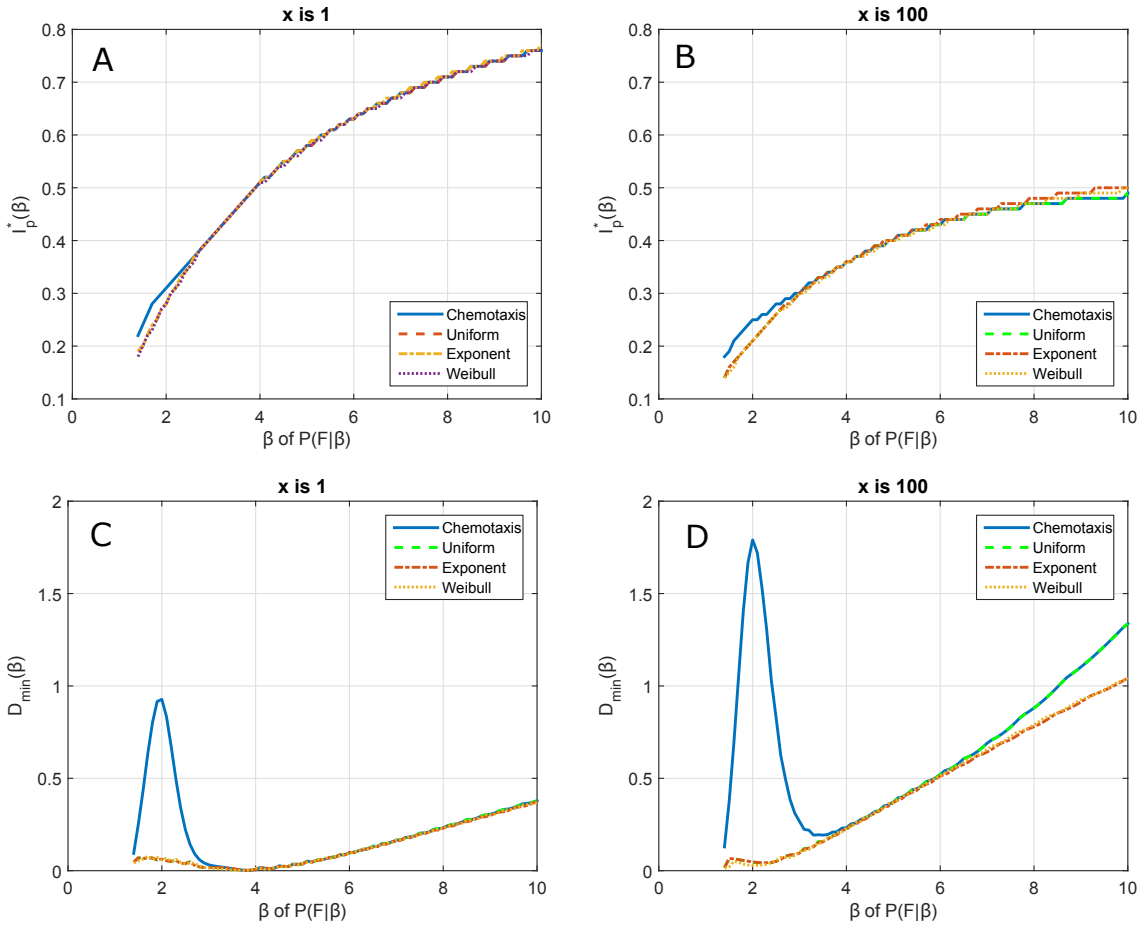

Figure 6.13: The effect of priors on the minimum divergence score. Rows separate the effect of priors on the best set of internal models $P(F|I_p^*)$ (Top) and their corresponding divergence score (Bottom). Columns separates results of when the internal models are stimulated with fold of weak background cAMP (Left) and strong background cAMP (Right).

Similar to the previous section, we visualized the landscape of D_{KL} score as contours in Figure 6.12. Figure 6.12 shows that regardless of priors, a stark difference can be observed in the divergence result computed by different background cAMP. A weak background cAMP of $x = 1$nM seems to yield a more consistent and narrower valley compared to the result by $x = 100$nM. This indicates that there is a better separation between the distributions of the compared internal $P(F|I_p, x = 1), I_p \in \mathbf{I_p}$ and external $P(F|\beta), \beta \in \mathbf{B}$ model. The clear separation is due to the symmetricness found in the distribution of $P(F|I_p, x = 1)$ for all $I_p \in \mathbf{I_p}$. In contrast, contours of background $x = 100$nM show flat regions as seen previously in section 6.4.3. This is caused by the heavy tailness of $P(F|I_p, x = 100)$ (for all $I_p \in \mathbf{I_p}$) distributions especially when conditioned upon high I_p.

As seen in the previous section, it is difficult to extract meaningful insights just by observing the contours of Figure 6.12. Therefore we derived the set of perceptions with minimum divergence scores $I_p^*(\beta)$ and the corresponding minimum divergence score $D_{\min(\beta)}$ for $P(F|I_p, x = 1)$ and $P(F|I_p, x = 100)$ in the similar manner as what we have done previously in section 6.4.3. The result is shown in Figure 6.13 where a quick glance reveals that the effects of priors between different background cAMP are hardly distinguishable. In general the profiles of $I_p^*(\beta)$ derived by internal conditioned on $x = 1$nM across all priors in Figure 6.13A are more unique compared to when $x = 100$nM indicated by the saturation in Figure 6.13B. The divergence score of internal with weaker background $x = 1$nM is also significantly better as shown in Figure 6.13C,D. Therefore we can conclude that internal model of a weaker background has a higher accuracy of perceiving what the external distribution of fold is .

6.5 Validating the bias-distinguishability relation

In this section our primary goal is to examine whether the bias-distinguishability relation as described by equation 6.3 is valid in the context of FCD. In order to achieve this goal, we first quantify bias and distinguishability threshold and examine their characteristics.

6.5.1 Bias

In the previous section, we have quantified the accuracy between the internal perception of fold change given observed sensory response $P(F|I_p)$ and external fold change distribution $P(F|\beta)$. The divergences between $P(F|I_p)$ and $P(F|\beta)$ can also be considered as biases. However, as illustrated in Figure 6.1, biases are defined in the context the Observer model as deviations between posterior estimates and the true stimulus. We further illustrate the definition of bias in Figure 6.14[1]. When an observer model is stimulated by a true fold denoted as F_{T} drawn from some distribution $P(F)$, the model then produces a posterior distribution of estimates $P(\hat{F}|F_{\mathrm{T}})$ to represent its 'overall perception'. In Figure 6.14 we have illustrated $P(\hat{F}|F_{\mathrm{T}})$ as a gaussian distribution. Given F_{pre} as the best estimator, the perceptual bias for estimating true stimulus F_{T} denoted as $b(F_{\mathrm{T}})$ is defined as

$$b(F_{\mathrm{T}}) = |F_{\mathrm{T}} - F_{\mathrm{pre}}| \tag{6.19}$$

[1] In Wei and Stocker (2017), for a given stimulus θ, the bias of stimulus $b(\theta)$ is expressed in the term of $\hat{\mu}(\theta) = \theta + b(\theta)$ where $\hat{\mu}(\theta)$ is the mean of a gaussian distribution. The relation of bias and prior distribution of stimulus is given as $b(\theta) \propto (1/p(\theta)^2)'$ and is proven true for various loss functions that the Bayesian decoder minimizes.

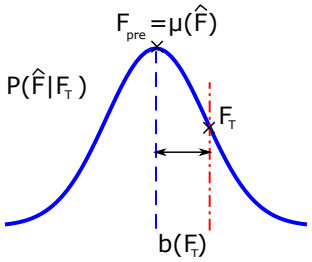

Figure 6.14: Definition of overall bias

where in the case of Figure 6.14 we used the mean of $P(\hat{F}|F_{\mathrm{T}})$ distribution as F_{pre}. In the context of our study we derive the posterior distribution of estimates or the 'overall internal perception' $P(\hat{F}|F_{\mathrm{T}})$ by averaging over all $I_p \in \mathbf{I_p}$ as

$$P(\hat{F}|F_{\mathrm{T}}) = \sum_{I_p \in \mathbf{I_p}} P(\hat{F}|I_p)P(I_p|F_{\mathrm{T}}) \tag{6.20}$$

where $P(\hat{F}|I_p)$ and $P(I_p|F_{\mathrm{T}})$ are respectively the posterior and conditional distribution from chapter 5. We already know the underlying stimulus F_{T} that resulted in the approximated $P(I_p|F_{\mathrm{T}})$. We then solve our prediction of the true stimulus denoted as F_{pre}

$$F_{\mathrm{pre}} = \underset{\hat{F}}{\operatorname{argmax}}\, P(\hat{F}|F_{\mathrm{T}}) \tag{6.21}$$

where we take the maximum value or the mode of the distribution $P(\hat{F}|F_{\mathrm{T}})$ as our best estimator. We computed $P(\hat{F}|F_{\mathrm{T}})$ for all $F_{\mathrm{T}} \in \mathbf{F}_{\mathrm{T}}, \mathbf{F}_{\mathrm{T}} = (2, 2.1, \ldots, 10)$ and derived their corresponding F_{pre}. We plotted samples of results of $P(\hat{F}|F_{\mathrm{T}})$ and F_{pre} for given $F_{\mathrm{T}} = 2, 6, 10$ for all priors in Figure 6.15. Figure 6.15 shows that in general the bias increases across all priors when the sensed true stimulus F_{T} increases.

We then computed the perceptual bias $b(F_{\mathrm{T}})$ (equation 6.19) evaluated using F_{pre} derived from all $F_{\mathrm{T}} \in \mathbf{F}_{\mathrm{T}}, \mathbf{F}_{\mathrm{T}} = (2, 2.1, \ldots, 10)$ and show the result in Figure 6.16. As can be seen from Figure 6.16, there are two different regions of bias for chemotaxis prior based perception. In the range of small fold $F_{\mathrm{T}} < 4$ the perceptual bias modelled with chemotaxis prior increases at a relatively fast rate. For the range of $F_{\mathrm{T}} \geq 4$ the bias then drops drastically and is equal to the bias of the uniform based perception. One reason for the increasing bias in $F_{\mathrm{T}} < 4$ is because the prediction $F_{\mathrm{pre}} = 1.1$ yielded is the same for all $P(\hat{F}|F_{\mathrm{T}})$ within this range. As can be seen in Figure 6.15 left panels, the indifferent prediction is further caused by the fact that the chemotaxis prior based perception will always assign the highest probability to $F = 1.1$ when stimulated with $F_{\mathrm{T}} < 4$. The decision to maximise $P(\hat{F}|F_{\mathrm{T}})$ in equation 6.21 will always yield the same

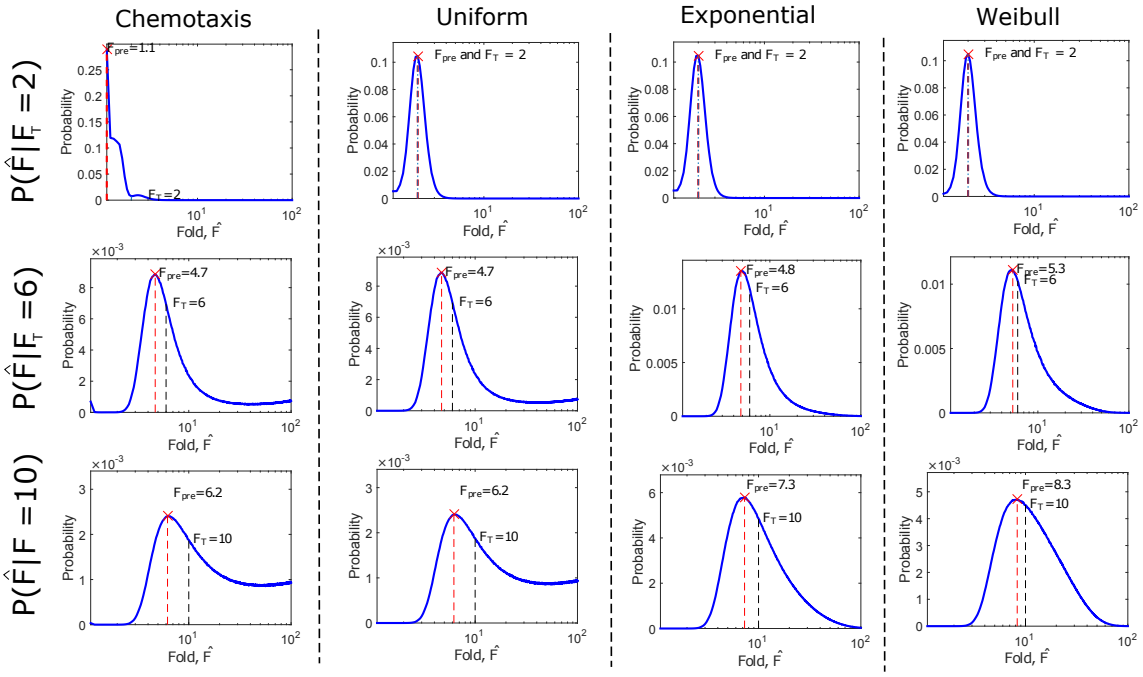

Figure 6.15: The effect of priors on bias. Vertical dashed red lines indicate predictions F_{pre} from the overall internal perceptions while the vertical black lines indicate the true stimulus F_{T}.

perception regardless of the true stimulus. The origin of this phenomenon can be traced back to the chemotaxis prior $P(F)$ which assigns strong probability values for $F < 2$.

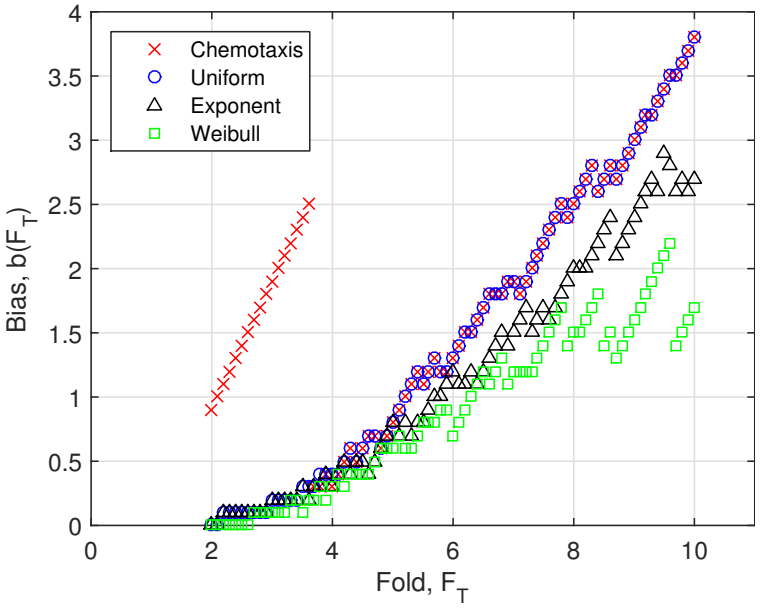

Figure 6.16: Bias for different priors.

6.5.2 Distinguishability threshold

Previously in chapter 4 we have quantified the distinguishability between two folds F_x and F_y and showed the result of overlapping areas in Figure 4.6. Here we extract the 'distinguishability threshold' as a function of fold denoted as $D(F)$ by first finding all possible pair values of x and y that satisfies $A^F[x, y] = 0.4$. Essentially what we are looking for are the x, y combinations that lies on the two red curves of Figure 4.6 where they represent the first combination that are deemed distinguishable. The distinguishability threshold $D(F)$ is then solved by $D(F)_{\text{large}} = x - y$ for $x < y$ and $D(F)_{\text{small}} = y - x$ for $x > y$. The former is the threshold between fold x and larger folds while the latter is the threshold between fold x and smaller folds. This requirement of having to define two distinguishability threshold is due to the fact that the overlapped distribution $P(I_p|F)$ computed is asymmetric. The result of computing both $D(F)_{\text{large}}$ and $D(F)_{\text{small}}$ are shown in Figure 6.17.

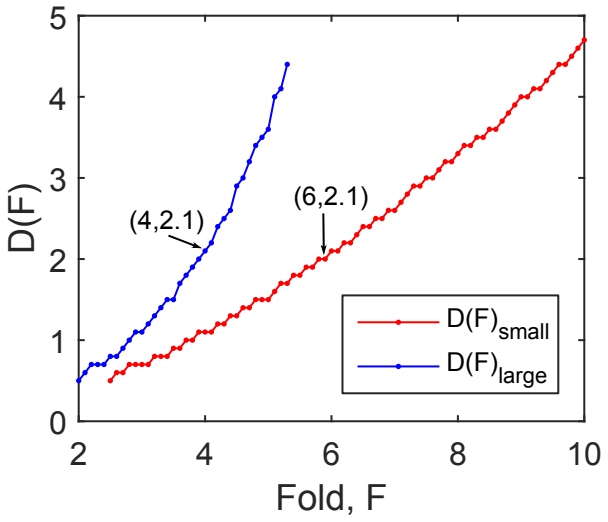

Figure 6.17: Distinguishability threshold. $D(F)_{\text{small}}$ is the minimally distinguishable smaller fold and $D(F)_{\text{large}}$ is the minimally distinguishable larger fold.

An example of how Figure 6.17 should be analysed is as follow. For $F = 4$ that lies on the blue line, the discrimination threshold is $D(F)_{\text{large}} = 2.1$. This means that the minimally distinguishable larger fold for $F = 4$ is $F = 6.1$. Likewise the minimally distinguishable smaller fold for $F = 6$ is $F = 3.9$ indicated by the coordinate on the red line pointed by the arrow. The result from Figure 6.17 shows that in general distinguishability threshold increases with stimulus fold.

6.5.3 Bias-distinguishability threshold relation

Now that we have quantified both bias and distinguishability threshold, we examine the validity of equation 6.3 describing the relation between the two measures of perception.

We ask whether the relation between bias and distinguishability threshold in the observer model of sensing stimulus

$$b(F) \propto (D(F)^2)'$$

is also true in the context of FCD. The bias-distinguishability relation established by Wei and Stocker (2017) is supported by results from studies on sensory system of circular variables such as visual orientation. However, Wei and Stocker (2017) state that for sensory systems operating with magnitude variables, the relation between distinguishability threshold and stimulus variable is expected to obey Weber's law where threshold must increase linearly with stimulus. Consequently it is predicted that the perceptual bias is also a linear function of stimulus.

We first examine the relation between distinguishability threshold and stimulus fold as observed in Figure 6.17 by fitting linear and quadratic curves to the data. The result of fitting both functions is shown in Figure 6.18 and the corresponding sum squared of residuals are listed in table 6.2. As can be observed, the distinguishability threshold-fold relation is better described by quadratic function as indicated by the red solid curves in Figure 6.17 rather than linear functions. Therefore it is more accurate to say that the distinguishability threshold increases in a quadratic manner as the stimulus fold change increases. It is important to note that the distinguishability threshold derived here is for fold change in concentration and not of the magnitude of the concentration itself. If it was the latter case, then the linear relation of the Weber's Law as emphasised by Wei and Stocker (2017) is expected to hold.

Given that $D(F)$ is governed by quadratic functions, $(D(F)^2)'$ would then yield cubic functions. Hence, the perceptual bias $b(F)$ would need to be proportional to distinguishability threshold defined as a cubic function of stimulus fold in order for the relation of equation 6.3 to be valid. However as can be seen from Figure 6.16, bias is better described by a linear or a quadratic function of fold F. Therefore, it can be concluded that the validity of equation 6.3 does not hold true when the bias is defined as equation 6.19.

Table 6.2: Sum of Squared Residuals for linear and quadratic curves fitted to the distinguishability threshold data.

$D(F)$	Linear	Quadratic
$D(F)_{\text{large}}$	1.0946	0.0853
$D(F)_{\text{small}}$	1.9147	0.0943

As we have defined two different distinguishability threshold, we plotted $b(F)$ of Figure 6.16 against $D(F)$ (instead of plotting $b(F)$ against $D((F)^2)')$) of Figure 6.17 in Figure

6.19A,B. Figure 6.19A,B indicate a possible linear relation between $b(F)$ and $D(F)$ for both $D(F_{\text{large}})$ and $D(F_{\text{small}})$. As distinguishability threshold increases, the perceptual bias also increases. The correlation is expected to be stronger for $D(F_{\text{small}})$ compared to $D(F_{\text{large}})$ regardless of the type of priors. When the threshold for higher fold to distinguish smaller fold increases, there is a greater perceptual bias as the bias is of the higher fold. The existence of two regions of bias can be seen when the internal model is computed using the chemotaxis prior.

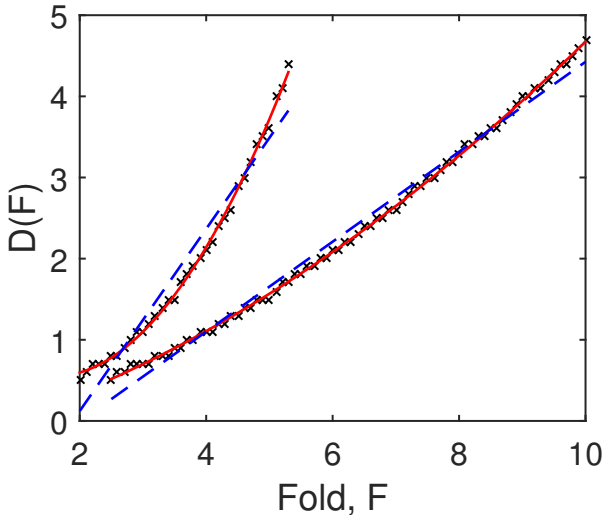

Figure 6.18: Distinguishability threshold (black crosses) fitted with linear(dashed blue lines) and quadratic curve (solid red lines).

Hence our current conclusion is that the relation of $b(F) \propto (D(F)^2)'$ as derived by Wei and Stocker (2017) does not hold true in the case of FCD in *Dictyostelium* cells. Instead, a linear relation of $b(F) \propto D(F)$ as demonstrated by Figure 6.19A,B would be more plausible.

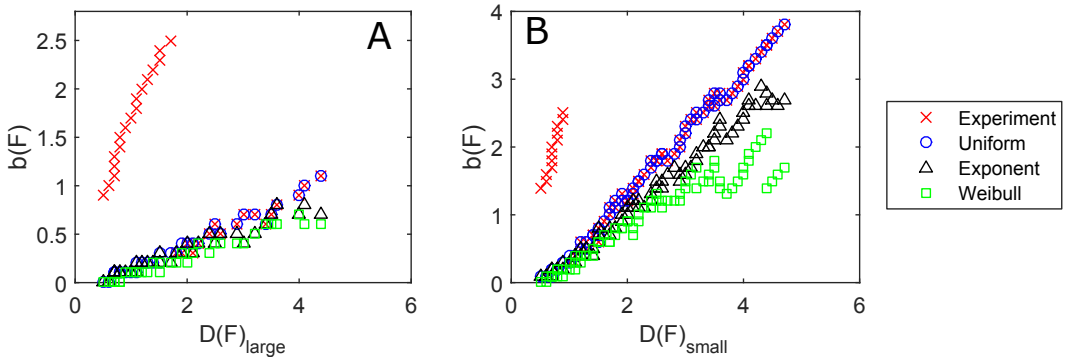

Figure 6.19: Bias-distinguishability threshold relation plotted for internal model based on different types of priors. (A) Minimally distinguishable threshold for larger folds. (B) Minimally distinguishable threshold for smaller folds.

6.6 Summary

This chapter focusses on the evaluation of the internal model derived in chapter 5. In order to quantify the accuracy of perception by the internal model, we have characterized a model of the external fold change. We have also explored how the model is constrained by its parameter $\mu_{\mathrm{T}}, \sigma_{\mathrm{T}}, N_y$ and showed that the two most important factors are the coefficient of variance δ_y and ratio of means of sums β. A mathematical justification is also given to show the validity of the external model. The most surprising result is that the external model displayed similar characteristics to the internal model despite they are derived independently. The former was derived using a statistical approach to model simple sums of cAMP produced, while the latter is a result of a long and complex process involving a Bayesian inference of the posterior distribution of fold changes preceded by the 1000 variation of model ODEs representing the bio-chemical attributes of the signalling pathway.

Using the Kullback-Leibler divergence as a measure of accuracy of perception, we showed that the perception is more accurate when compared with external distribution of lower fold. The accuracy diverges more as the compared mean of the external fold increases. We also demonstrated the limitation of Kullback-Leibler divergence as a measure of perception's accuracy when the compared external fold is high. We derived sets of most accurate perceptions and showed that perceptions are similar across different priors except for internal model based upon the chemotaxis prior. In fact, the chemotaxis prior based model is the only model with the distinct feature of two region of perceptions. The accuracy of the internal perception is also much higher when stimulated with folds of weaker background cAMP.

We also described the Observer model, characterized the prediction from the overall internal perception and defined bias in the context of FCD. We showed that bias increases as the stimulated fold is stronger across all type of priors except for the chemotaxis prior based internal. The distinguishability threshold is characterized for two different cases- one for the minimally distinguishable larger folds and the other for the minimally distinguishable smaller folds. We showed that the bias-distinguishability threshold as established by Wei and Stocker (2017) does not hold true for FCD in *Dictyostelium* cells.

Chapter 7

Summary and Conclusions

In this thesis, we have presented various characterization of the FCD sensing mechanism in *Dictyostelium* cells through a well described mathematical model of the upstream signalling pathway. We acknowledge that only the sense-perception components of the cyclic-AMP sense-peception-response mechanism has been successfully characterized. The study of FCD accuracy derived from upstream models is significant in characterizing the constraints that models impose on downstream models. The accuracy of FCD of upstream models then acts as a criteria for model selection, limiting plausible downstream models. One of the issues that we have identified from literature when modelling the sense-response mechanism such as the oscillation of cAMP in single or population of cells (Sgro et al., 2015; Noorbakhsh et al., 2015) is that the assumptions of upstream models often do not emulate significant properties that allow for accurate sensing. We argue that if the properties of the upstream signalling pathway are not captured correctly, then the modelled actuator would yield unrealistic results. Or even if the results concur with experimental data, the derived model would not be a sensible approximation of the sense-response mechanism.

We summarise and conclude our thesis here in the context of the questions posed in chapter 1 and derive several conclusions from our findings. To answer what is the accuracy of FCD observed in mathematical models of the *Dictyostelium* cell, we started by probing the model ODEs described by Takeda et al. (2012). We found that the dynamics of the model are stable and exhibit adaptation as a crux component of FCD when the input to the model ODEs continuously increases. Hence we deem that this initial analysis provided enough support to validate the investigation of the accuracy of FCD using the model ODEs by Takeda et al. (2012).

7.1 Criteria enabling FCD by the model

We studied what are some of the criteria that enable the validated model to exhibit FCD in the first place, regardless whether the fold changes detected are accurate or not. Half of the parameters of the model were then estimated using the ABC-SMC method where we derived posterior densities of parameters. This provided the operating ranges of parameters in detecting fold changes where some of the ranges deviate far from what Takeda et al. (2012) estimated. The variability observed in the posterior distributions showed that some parameters are less variant and implies that some strict constraints are necessary in order for the model to exhibit FCD. It has also been shown through PCA that no single principal component of the sampled parameters can primarily capture the exhibited FCD behaviour. However, different posterior distributions might be obtained if we estimated the full 18 parameters of the model ODEs or if we chose a different set of data for data fitting. To estimate the full parameters of the model would be computationally expensive, a problem common to the SMC method when dealing with complex models. An alternative approach is to apply Gibbs sampling, where estimated parameters are divided into blocks. Some blocks are sampled from the conditional probability with the remaining blocks of parameters fixed. The blocks are then switched and the sampling process is repeated.

7.2 Lower fold changes are being detected more accurately and are more distinguishable

Nevertheless, the posterior parameters do give us a measure of the model's variability in capturing the FCD in *Dictyostelium* experiment. The densities of sparsely generated responses from the estimated parameters were modelled using the log-normal density function where its coefficients were approximated using quadratic functions. We found that responses free from background dependencies are more consistent to stimulant with lower fold changes. This provides the first hint to the accurateness of FCD by the model—lower fold changes are being detected more accurately as opposed to higher fold changes. We also quantified the fold distinguishability property by measuring the overlapping area of distribution of responses. Our results showed that responses to lower fold changes are more distinguishable and therefore lower fold changes in stimulant are also more distinguishable than higher fold changes. The characterization of the stimulus-response relation showed that the hyperbolic equation describes the relation better than the logarithmic law proposed by Adler et al. (2014). We also found that the uncertainties in the responses are better described by a logarithmic relation as opposed to a linear relation. The conclusions reached here are limited by the properties of the model and are further restricted by the log-normal density function used to approximate the responses of the model. Although the heavy right tailness seen in the distribution of responses

can be characterized using many other families of distributions such as the Gamma or F distribution, we justify the choice of the log-normal as studies have shown that responses of sensory systems can be described using the logarithmic compression hypothesis.

7.3 The probability of lower fold changes is higher

We inferred the posterior probability of fold changes being detected given the sensory responses generated from the model using Bayes' theorem. In doing so we modelled a novel prior probability of fold changes encountered by *Dictyostelium* cells based on chemotaxis experiment and compared with other known priors. We found that the posterior probability is significant in ranges of low fold changes and decreases drastically as the observed responses increases. Therefore, given lower responses, the probability of lower fold change is higher. The inferred posterior is constrained by the conditional and prior probability. We showed that with the exception of the chemotaxis based prior, the inferred posterior displays an 'anti-Bayesian effect' where it is biased away from the prior by the conditional probability. It can be argued that the stark differences in distribution profiles between the chemotaxis based prior and the alternative priors suggest that comparison of posteriors computed by these priors are impractical. An alternative approach is to choose model parameters such that the resulting alternative priors are also significant in a narrow range in order to influence the posterior. It is acknowledged that the choice of prior although indispensable in the Bayesian approach remains a controversial subject.

7.4 Perceptions of lower extracellular fold changes and of weaker initial stimulus are more accurate

Using the inferred posteriors, we characterized the perception of *Dictyostelium* cells regarding the state of the extracellular fold changes. In doing so, a novel model of the extracellular fold changes was derived and divergences between the two distributions were computed. We found that *Dictyostelium* cells characterized by the model ODEs of Takeda et al. (2012) perceive fold changes better when the extracellular fold changes are of lower range and worsens as the fold changes in the environment increases. We derived sets of most accurate perceptions and showed that there are different regions of perceptions if the prior beliefs are derived from chemotaxis experiments. From the modelled perceptions we derived the predictions of fold changes by the population of cells and computed the biases. We showed that bias increases as the stimulated fold change is stronger. We also characterized the minimally distinguishability threshold and showed that the threshold increases almost quadratic like as the stimulus fold increases.

7.5 Future work

We describe here several future research directions in modelling the complete cyclic AMP sense-response mechanism of the *Dictyostelium* cells. The next step is to probe and characterize the response or actuator component of the *Dictyostelium* cells. In the studies by Sgro et al. (2015) and Noorbakhsh et al. (2015) the peak levels of the transient generated by the sensing component are treated as inputs to a postulated autonomous excitable, oscillatory model system introduced in the neuroscience literature. This mechanism contains a threshold for oscillations via a Hopf bifurcation suggests a variable response based on a stochastic triggering mechanism. In contrast, a different mechanism is proposed in Kamino et al. (2017) that makes explicit reference to the FCD property and follows similar lines to Martiel and Goldbeter (1987) where intracellular production of cAMP by adenylyl cyclase (ACA) sets up the relay mechanism forming a positive feedback loop, and the desensitisation of the CAR receptor (another mechanism for adaptation) enables an oscillatory behaviour.

In both sets of studies the link to the specific mechanism proposed in Takeda et al. (2012) is only obliquely made, with Kamino et al. (2017) extending the FCD mechanism of the IFF networks to a cell density-dependent secretion module, and Sgro et al. (2015) disputing the relevance of the IFF module to the oscillatory responses. Although model simplifications makes it easier to analyse the system's mathematical properties, we are in the opinion that future research should characterize the sense-secrete system of the *Dictyostelium* cell by incorporating the upstream signalling pathway model ODEs described by Takeda et al. (2012). One approach is by restructuring the model ODEs by Takeda et al. (2012) from a feedforward network to a feedback network model. This can be achieved by defining the secretion of cAMP as

$$\frac{dx(t)}{dt} = \frac{k_x^+ Ras(t)^3}{K_D^3 + Ras(t)^3} - k_x^- x(t)$$

where cAMP is denoted here by $x(t)$ in contrast to the experimentally controlled extracellular levels x and x'. The parameters k_x^+ and k_x^- are the production and decay rate of the molecule cAMP and $K_D = k_x^-/k_x^+$ is the corresponding dissociation constant. $x(t)$ is a variable that combines intracellular levels of cAMP and that which is secreted, summarising a two-step description. The decay rate k_x^- can be attributed to a intracellular phosphodiesterase-enabled process (Dinauer et al., 1980a) or by dilution in the extracellular environment.

Another approach is to link the inputs from the sensing module modelled in Takeda et al. (2012) to the oscillatory FitzHugh-Nagumo based actuating module (Sgro et al., 2015; Noorbakhsh et al., 2015) that secretes cAMP to establish the feedforward amplification

(Wang et al., 2012) of responses. The model ODEs of Takeda et al. (2012) can be extended by adding two equations to described the oscillatory dynamics as

$$\begin{aligned} \frac{dA}{dt} &= A - (\frac{A^3}{3}) - Re + Ras \\ \tau\frac{dRe}{dt} &= A - \gamma Re + c_0 \end{aligned}$$

where in this coupled model, A and Re is the activator and repressor of the FitzHugh-Nagumo, γ, c_0, τ are the FitzHugh-Nagumo model parameters. It is important to note that although this coupled model can characterize the single cell level cAMP oscillation observed in experiments, it does not capture the sense-secrete mechanism in its system.

In both suggested models, the parameters of the extended equations can be constrained by the range of the posterior parameters estimated in chapter 3. The possible oscillating responses by both systems are then restricted by the experiments based constraints. Reversely the sets of parameters resulting in responses which are not oscillatory can be also identified. It has been reported in the experiments by Sgro et al. (2015) that the oscillation of cAMP by single *Dictyostelium* cells have a refractory period of 2 to 3 minutes which then governs the frequency of the cAMP pulses. This refractory period can be associated to the desensitization of the receptor or the adaptation time of the Ras protein. Indeed, the focus of this thesis has been on the maximum level of responses. There is a need to explore the role of the adaptation time for the maximum responses to return to its pre-stimulus level. The 1000 sets of parameters derived in chapter 3 would yield different adaptation time. This would in turn lead to different refractory periods of the extended model and would yield an estimate of the variability in the possible refractory period.

7.5.1 A broader perspective

The examples of future works given so far are of research projects that can be implemented directly using the results obtained in this thesis. The goal of incorporating a feedback model is to enhance the modelling of the sense-perception mechanism. On the other hand, the coupling of an oscillation module is to evaluate how the sense-perception mechanism constraints or is constrained by the oscillation module. However, if we look from a broader perspective, the research framework developed in this thesis can be applied to understand the functional characteristics of different models across different biological systems. For example, future works can focus on evaluating the distribution of responses of other alternative mathematical models used to describe the chemotaxis pathway of *Dictyostelium* cells and characterize the sense-perception mechanism. How different would the perception of the population of cells be if it is modelled using other

models? It is also possible to characterize in the same manner the accuracy of FCD by the three models of *Rhodobacter sphaeroides* chemotaxis as introduced in Hamadeh et al. (2013) that is said to exhibit FCD and are robust to structural changes and variation in parameters. What would the characteristics of the probability of fold changes by the three models of *Rhodobacter sphaeroides* chemotaxis be? Would any of the models share the same characteristics as the model of FCD in *Dictyostelium* cells derived in this thesis? Hence, the comparison of characteristics of FCD is not only between models of *Dictyostelium* but is also possible across different organism that is said to exhibit the FCD property. This enables future research to further extract design principles of FCD by probing the relation between the likelihood of displaying functional properties and the underlying model structures. The research framework introduced in this thesis is by no means limited to the FCD property only and can be further generalized to other observed behaviour. One interesting study would be the characterization of adaptation as this behaviour is observed in many organism and is widely documented compared to FCD.

In the conventional approach of mathematical modelling of biological systems, the goal is to identify model structures and parameters that is compatible with experimental data and provide predictions to future experiments. However, by analysing population of responses and models of perception as demonstrated in this thesis, the goal then changes to identifying a model that is likeliest to exhibit functional behaviour as required by the system. We argue that mathematical models that fit well with experiment data but do not exhibit desirable functional properties are not realistic representations of the biological system.

Appendix A

Approximate Bayesian Computation (ABC) method

Bayesian methods can be used to estimate parameters of models of biological systems by Ordinary Differential Equations(ODEs). By using Bayes' rule, we can estimate model parameter θ by inferring the posterior probability of θ given observed data X, denoted as $P(\theta|X)$

$$P(\theta|X) = \frac{P(X|\theta)P(\theta)}{P(X)} \tag{A.1}$$

where the likelihood $P(X|\theta)$ is the probability of data given parameter, $P(\theta)$ is the prior probability of parameter θ and $P(X)$ is the marginalized likelihood.

However, in the case where the likelihood and model evidence are analytically intractable, approximation method is more suitable in inferring the posterior probability. A well known algorithm is the Approximation Bayesian Computation (ABC) rejection sampler, developed earlier by Pritchard et al. (1999) and Beaumont et al. (2002) in population genetics. The posterior distribution is simplified by eliminating the constant of proportionality as,

$$P(\theta|X) \propto f(X|\theta)\pi(\theta) \tag{A.2}$$

where $f(X|\theta)$ is the likelihood of parameter θ given data X (Toni et al., 2009). θ is generated from $\pi(\theta)$ and accepted with probability $f(X|\theta)$. The method is further improved when the calculation of likelihood is replaced by comparing simulated data X_s to the observed data X_d. X_s is simulated from a generative model M_θ with θ drawn from $\pi(\theta)$ such that $X_s \sim M_\theta$. The posterior is then expressed as

$$P(\theta, X_s|X_d) = \frac{\bullet(d(X_d, X_s) \leq \epsilon)(X_s \sim M_\theta)\pi(\theta)}{\int_\theta \int_{X_s} \bullet(d(X_d, X_s) \leq \epsilon)(X_s \sim M_\theta)\pi(\theta)} \tag{A.3}$$

where $\epsilon > 0$ is the tolerance value, $\bullet$ is the indicator function and $d(X_d, X_s)$ is the distance function. The ABC generic algorithmic form is given as

1. Sample candidate parameter vector θ^* from prior distribution $\pi(\theta)$ independently.
2. Simulate dataset X_s from model M_θ with parameter θ^*: $X_s \sim M_\theta|_{\theta \leftarrow \theta^*}$
3. Compare the simulated dataset X_s, with the observed data X_d, using some distance function d and tolerance $\epsilon \geq 0$. If $d(X_d, X_s) \leq \epsilon$ accept θ^*, else reject.

The output is a set of parameter values sampled from distribution of $P(\theta|d(X_d, X_s) \leq \epsilon)$. If the tolerance ϵ is small enough, then the distribution $P(\theta|d(X_d, X_s) \leq \epsilon)$ is close to the true posterior $P(\theta|X_d)$. For dynamical models, comparison between the simulated and observed data can be carried out directly without having to use summary statistics. The pseudo-code for ABC rejection sampler (Pritchard et al., 1999) is given as Algorithm 1.

Algorithm 2 ABC Rejection Sampler

```
Sample candidate parameter θ* from prior P(θ)
Simulate dataset X_s ~ M_θ|_{θ←θ*}
if d(X_d, X_s) ≤ ε then
    Accept θ*
else
    reject
end if
```

If the gap between the prior and posterior distribution is very large, then the sampled candidates are from parameter space with low likelihood, causing a low acceptance rate. The algorithm is therefore inefficient as it is time consuming. Other ABC methods such as Markov Chain Monte Carlo (MCMC) (Marjoram et al., 2003) and Sequential Monte Carlo (SMC) (Sisson et al., 2007) have been introduced to overcome the inefficiency of ABC rejection sampler. However, in MCMC method it is still possible to have low acceptance probability and correlated samples. This will result in a long chain that is difficult to escape the parameter space of low likelihood (Beaumont, 2010). For this reason and simplification purposes, we will focus the discussion on Sequential Monte Carlo (SMC) method as it is more relevant for our work.

A.1 Approximate Bayesian Computation-Sequential Monte Carlo (ABC-SMC) method

To overcome the disadvantages of ABC rejection sampler and MCMC, Sequential Monte Carlo(SMC) based ABC method was introduced by Sisson et al. (2007) based on the algorithm by Del Moral et al. (2006). A further refined version of ABC-SMC was developed by Beaumont et al. (2009) and Toni et al. (2009). We will focus on the SMC algorithm varied by Toni et al. (2009). This algorithm is similar to the algorithm by Beaumont et al. (2009) and Sisson et al. (2007).

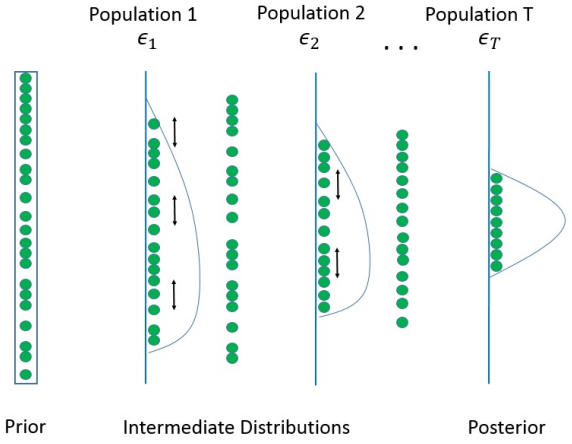

Figure A.1: Particle filter mechanism of ABC-SMC method reillustrated from Toni and Stumpf (2009). Population of particles are gradually filtered through the intermediate distributions. With enough population levels T and small tolerance ϵ_T, the last distribution approximates close to the true posterior distribution.

The mechanism of ABC-SMC works like a particle filter with many cascaded tolerance level $\epsilon_1 > \epsilon_2 > \cdots > \epsilon_T > 0$. This concept would enable the algorithm to escape low probability sampling space that made previous ABC method inefficient. At level $t = 1$, N numbers of candidate parameter values called *'particles'* are sampled independently from prior distribution $\pi(\theta)$. Accepted particles would form an initial population of N particles, $\theta_1, ..., \theta_N$ with intermediate distribution $P(\theta|d(X_d, X_s) \leq \epsilon_1)$. At $t = 2$, the particles are weighted and sampled from a new prior which is set as the previous intermediate distribution, $\pi(\theta) = P(\theta|d(X_d, X_s) \leq \epsilon_1)$. Particles surviving the rejection step with tolerance ϵ_i are perturbed with perturbation kernel K_{i+1} and evaluated against tolerance ϵ_{i+1}. In this way, particles are propagated and filtered through a series of intermediate distribution $P(\theta|d(X_d, X_s^*) \leq \epsilon_i), i = 1...T-1$, gradually approaching the target posterior distribution. With a large enough population , it can escape low probability space otherwise difficult with ABC MCMC.

The pseudo-code for the algorithm is shown in Algorithm 2. Single asterisk (θ^*) indicates particles before perturbation while double asterisk (θ^{**}) indicates particles after

perturbation. Perturbation kernel K_t is chosen as random walk (uniform or gaussian). For a illustration of the particle filtering mechanism, refer to Figure A.1.

Algorithm 3 ABC-SMC

1: Initialize tolerance $\epsilon_1, \epsilon_2 ..., \epsilon_T$, population $t = 0$,
2: Initialize particle indicator $i = 1$
3: **if** $t = 0$ **then**
4: Sample particle θ^{**} independently from $\pi(\theta)$
5: **else**
6: Sample particle θ^{*} from previous population θ^{i}_{t-1} weighted with w_{t-1}
7: Perturb θ^{*} with perturbation kernel K_t to get θ^{**} $K_t(\theta|\theta^{*})$
8: **end if**
9: **if** new prior $\pi(\theta^{**}) = 0$ **then**
10: Return to 3
11: **else**
12: Simulate candidate dataset from generative model $X_s \sim M_\theta|_{\theta \leftarrow \theta^{*}}$
13: **end if**
14: **if** $d(X_d, X_s) \geq \epsilon_t$ **then**
15: Go to 3
16: **else**
17: Set $\theta^{i} = \theta^{**}$, calculate weight for particle $\theta^{(i)_t}$,

$$w_t^{(i)} = \begin{cases} 1, & \text{if } t = 0 \\ \frac{\pi(\theta_t^{(i)})}{\sum_{j=1}^{N} w_{t-1}^{(j)} K_t(\theta_{t-1}^{(j)}, \theta_t^{(i)})} & \text{if } t > 0 \end{cases}$$

18: **end if**
19: **if** $i < N$ **then**
20: $i = i + 1$
21: Go to 3
22: **else**
23: Normalize weights
24: **end if**
25: **if** $t < T$ **then**
26: Set $t = t + 1$
27: Go to 2
28: **end if**

References

Adler, M., Mayo, A., and Alon, U. (2014). Logarithmic and power law input-output relations in sensory systems with fold-change detection.

Adler, M., Szekely, P., Mayo, A., and Alon, U. (2017). Optimal regulatory circuit topologies for fold-change detection. *Cell systems*, 4(2):171–181.

Alon, U. (2007a). *Introduction to Systems Biology: And the Design Principles of Biological Networks*, volume 10. CRC press.

Alon, U. (2007b). Network motifs: theory and experimental approaches. *NATURE REVIEWS— GENETICS*, 8:451.

Amselem, G., Theves, M., Bae, A., Bodenschatz, E., and Beta, C. (2012). A stochastic description of dictyostelium chemotaxis. *PloS one*, 7(5):e37213.

Barkai, N. and Leibler, S. (1997). Robustness in simple biochemical networks. *Nature*, 387(6636):913–917.

Barlow, H. B. (1961). Possible principles underlying the transformations of sensory messages.

Beaumont, M. A. (2010). Approximate bayesian computation in evolution and ecology. *Annual review of ecology, evolution, and systematics*, 41:379–406.

Beaumont, M. A., Cornuet, J.-M., Marin, J.-M., and Robert, C. P. (2009). Adaptive approximate bayesian computation. *Biometrika*, page asp052.

Beaumont, M. A., Zhang, W., and Balding, D. J. (2002). Approximate bayesian computation in population genetics. *Genetics*, 162(4):2025–2035.

Bonner, J. T. and Savage, L. (1947). Evidence for the formation of cell aggregates by chemotaxis in the development of the slime mold dictyostelium discoideum. *Journal of Experimental Zoology*, 106(1):1–26.

Brannon, E. M., Wusthoff, C. J., Gallistel, C., and Gibbon, J. (2001). Numerical subtraction in the pigeon: Evidence for a linear subjective number scale. *Psychological Science*, 12(3):238–243.

Burris, R. H. and Newcomb, E. H. (1991). Kenneth bryan raper: July 11, 1908-january 15, 1987. *Biographical memoirs. National Academy of Sciences (US)*, 60:251.

Clarke, M., Yang, J., and Kayman, S. C. (1988). Analysis of the prestarvation response in growing cells of dictyostelium discoideum. *Developmental genetics*, 9(4-5):315–326.

Cohen-Saidon, C., Cohen, A. A., Sigal, A., Liron, Y., and Alon, U. (2009). Dynamics and variability of erk2 response to egf in individual living cells. *Molecular cell*, 36(5):885–893.

Comer, F. I., Lippincott, C. K., Masbad, J. J., and Parent, C. A. (2005). The pi3k-mediated activation of crac independently regulates adenylyl cyclase activation and chemotaxis. *Current biology*, 15(2):134–139.

Comer, F. I. and Parent, C. A. (2006). Phosphoinositide 3-kinase activity controls the chemoattractant-mediated activation and adaptation of adenylyl cyclase. *Molecular biology of the cell*, 17(1):357–366.

Curry, R. E. (1972). A bayesian model for visual space perception. In *Seventh Annual Conference on Manual Control*, volume 281, page 187.

Dehaene, S. (2001). Subtracting pigeons: Logarithmic or linear? *Psychological Science*, 12(3):244–246. PMID: 11437308.

Dehaene, S. (2003). The neural basis of the weber–fechner law: a logarithmic mental number line. *Trends in cognitive sciences*, 7(4):145–147.

Dehaene, S., Izard, V., Spelke, E., and Pica, P. (2008). Log or linear? distinct intuitions of the number scale in western and amazonian indigene cultures. *Science*, 320(5880):1217–1220.

Del Moral, P., Doucet, A., and Jasra, A. (2006). Sequential monte carlo samplers. *Journal of the Royal Statistical Society: Series B (Statistical Methodology)*, 68(3):411–436.

Devreotes, P. N. and Steck, T. L. (1979). Cyclic 3', 5'amp relay in dictyostelium discoideum. ii. requirements for the initiation and termination of the response. *The Journal of cell biology*, 80(2):300–309.

Díaz-Francés, E. and Rubio, F. J. (2013). On the existence of a normal approximation to the distribution of the ratio of two independent normal random variables. *Statistical Papers*, 54(2):309–323.

Dinauer, M. C., MacKay, S. A., and Devreotes, P. N. (1980a). Cyclic 3-5-amp relay in dictyostelium discoideum. iii. the relationship of camp synthesis and secretion during the camp signaling response. *The Journal of Cell Biology*, 86(2):537–544.

Dinauer, M. C., Steck, T. L., and Devreotes, P. N. (1980b). Cyclic 3,5-amp relay in dictyostelium discoideum. iv. recovery of the camp signaling response after adaptation to camp. *The Journal of Cell Biology*, 86(2):545–553.

Dinauer, M. C., Steck, T. L., and Devreotes, P. N. (1980c). Cyclic 3,5-amp relay in dictyostelium discoideum. v. adaptation of the camp signaling response during camp stimulation. *The Journal of Cell Biology*, 86(2):554–561.

Edgington, M. P. and Tindall, M. J. (2014). Fold-change detection in a whole-pathway model of escherichia coli chemotaxis. *Bulletin of mathematical biology*, 76(6):1376–1395.

Ferrell, J. E. (2009). Signaling motifs and weber's law. *Molecular cell*, 36(5):724–727.

Geary, R. C. (1930). The frequency distribution of the quotient of two normal variates. *Journal of the Royal Statistical Society*, 93(3):442–446.

Gelman, A. et al. (2008). Objections to bayesian statistics. *Bayesian Analysis*, 3(3):445–449.

Goentoro, L. and Kirschner, M. W. (2009). Evidence that fold-change, and not absolute level, of β-catenin dictates wnt signaling. *Molecular cell*, 36(5):872–884.

Goentoro, L., Shoval, O., Kirschner, M. W., and Alon, U. (2009). The incoherent feedforward loop can provide fold-change detection in gene regulation. *Molecular cell*, 36(5):894–899.

Gutenkunst, R. N., Waterfall, J. J., Casey, F. P., Brown, K. S., Myers, C. R., and Sethna, J. P. (2007). Universally sloppy parameter sensitivities in systems biology models. *PLoS Computational Biology*, https://doi.org/10.1371/journal.pcbi.0030189.

Hamadeh, A., Ingalls, B., and Sontag, E. (2013). Transient dynamic phenotypes as criteria for model discrimination: fold-change detection in rhodobacter sphaeroides chemotaxis. *Journal of The Royal Society Interface*, 10(80):20120935.

Hart, Y. and Alon, U. (2013). The utility of paradoxical components in biological circuits. *Molecular cell*, 49(2):213–221.

Hart, Y., Antebi, Y. E., Mayo, A. E., Friedman, N., and Alon, U. (2012). Design principles of cell circuits with paradoxical components. *Proceedings of the National Academy of Sciences*, 109(21):8346–8351.

Hayya, J., Armstrong, D., and Gressis, N. (1975). A note on the ratio of two normally distributed variables. *Management Science*, 21(11):1338–1341.

Hinkley, D. V. (1969). On the ratio of two correlated normal random variables. *Biometrika*, 56(3):635–639.

Hironaka, K.-i. and Morishita, Y. (2014). Cellular sensory mechanisms for detecting specific fold-changes in extracellular cues. *Biophysical journal*, 106(1):279–288.

Iglesias, P. A. (2016). The use of rate distortion theory to evaluate biological signaling pathways. *IEEE Transactions on Molecular, Biological and Multi-Scale Communications*, 2(1):31–39.

Iijima, M. and Devreotes, P. (2002). Tumor suppressor pten mediates sensing of chemoattractant gradients. *Cell*, 109(5):599–610.

Ingram, P. J., Stumpf, M. P., and Stark, J. (2006). Network motifs: structure does not determine function. *BMC genomics*, 7(1):108.

Jeffreys, H. (1946). An invariant form for the prior probability in estimation problems. *Proc. R. Soc. Lond. A*, 186(1007):453–461.

Jeon, N. L., Dertinger, S. K., Chiu, D. T., Choi, I. S., Stroock, A. D., and Whitesides, G. M. (2000). Generation of solution and surface gradients using microfluidic systems. *Langmuir*, 16(22):8311–8316.

Kae, H., Kortholt, A., Rehmann, H., Insall, R. H., Van Haastert, P. J., Spiegelman, G. B., and Weeks, G. (2007). Cyclic amp signalling in dictyostelium: G-proteins activate separate ras pathways using specific rasgefs. *EMBO reports*, 8(5):477–482.

Kamino, K., Kondo, Y., Nakajima, A., Honda-Kitahara, M., Kaneko, K., and Sawai, S. (2017). Fold-change detection and scale invariance of cell–cell signaling in social amoeba. *Proceedings of the National Academy of Sciences*, page 201702181.

Kashtan, N., Itzkovitz, S., Milo, R., and Alon, U. (2004). Topological generalizations of network motifs. *Physical Review E*, 70(3):031909.

Klein, P., Theibert, A., Fontana, D., and Devreotes, P. (1985). Identification and cyclic amp-induced modification of the cyclic amp receptor in dictyostelium discoideum. *Journal of Biological Chemistry*, 260(3):1757–1764.

Kojadinovic, M., Armitage, J., Tindall, M., and Wadhams, G. (2013). Rhodobacter sphaeroides chemotaxis response kinetics: complexities in signalling but similarities in responses. *JR Soc. Interface*, 10.

Kölsch, V., Charest, P. G., and Firtel, R. A. (2008). The regulation of cell motility and chemotaxis by phospholipid signaling. *J Cell Sci*, 121(5):551–559.

Konijn, T. M., Van De Meene, J., Bonner, J. T., and Barkley, D. S. (1967). The acrasin activity of adenosine-3', 5'-cyclic phosphate. *Proceedings of the National Academy of Sciences*, 58(3):1152–1154.

Kortholt, A., Kataria, R., Keizer-Gunnink, I., Van Egmond, W. N., Khanna, A., and Van Haastert, P. J. (2011). Dictyostelium chemotaxis: essential ras activation and accessory signalling pathways for amplification. *EMBO reports*, 12(12):1273–1279.

Koshland, D. (1974). Chemotaxis as a model for sensory systems. *FEBS Letters*, 40:S2.

Kuethe, D. O., Caprihan, A., Gach, H. M., Lowe, I. J., and Fukushima, E. (2000). Imaging obstructed ventilation with nmr using inert fluorinated gases. *Journal of applied physiology*, 88(6):2279–2286.

Kullback, S. and Leibler, R. A. (1951). On information and sufficiency. *The annals of mathematical statistics*, 22(1):79–86.

Lazova, M. D., Ahmed, T., Bellomo, D., Stocker, R., and Shimizu, T. S. (2011). Response rescaling in bacterial chemotaxis. *Proceedings of the National Academy of Sciences*, 108(33):13870–13875.

Ma, W., Trusina, A., El-Samad, H., Lim, W. A., and Tang, C. (2009). Defining network topologies that can achieve biochemical adaptation. *Cell*, 138(4):760–773.

Macía, J., Widder, S., and Solé, R. (2009). Specialized or flexible feed-forward loop motifs: a question of topology. *BMC systems biology*, 3(1):84.

Mangan, S. and Alon, U. (2003). Structure and function of the feed-forward loop network motif. *Proceedings of the National Academy of Sciences*, 100(21):11980–11985.

Mangan, S., Zaslaver, A., and Alon, U. (2003). The coherent feedforward loop serves as a sign-sensitive delay element in transcription networks. *Journal of molecular biology*, 334(2):197–204.

Marjoram, P., Molitor, J., Plagnol, V., and Tavaré, S. (2003). Markov chain monte carlo without likelihoods. *Proceedings of the National Academy of Sciences*, 100(26):15324–15328.

Marsaglia, G. (1965). Ratios of normal variables and ratios of sums of uniform variables. *Journal of the American Statistical Association*, 60(309):193–204.

Marsaglia, G. et al. (2006). Ratios of normal variables. *Journal of Statistical Software*, 16(4):1–10.

Martiel, J. and Goldbeter, A. (1987). A model based on receptor desensitization for cyclic amp signaling in dictyostelium cells. *Biophys J.*, 52(5):807–28.

Marzen, S. E. and DeDeo, S. (2017). The evolution of lossy compression. *Journal of The Royal Society Interface*, 14(130):20170166.

Masson, J.-B., Voisinne, G., Wong-Ng, J., Celani, A., and Vergassola, M. (2012). Non-invasive inference of the molecular chemotactic response using bacterial trajectories. *Proceedings of the National Academy of Sciences*, 109(5):1802–1807.

Mato, J. M., Losada, A., Nanjundiah, V., and Konijn, T. M. (1975). Signal input for a chemotactic response in the cellular slime mold dictyostelium discoideum. *Proceedings of the National Academy of Sciences*, 72(12):4991–4993.

Meier, B., Zielinski, A., Weber, C., Arcizet, D., Youssef, S., Franosch, T., Rädler, J. O., and Heinrich, D. (2011). Chemotactic cell trapping in controlled alternating gradient fields. *Proceedings of the National Academy of Sciences*, 108(28):11417–11422.

Meili, R., Ellsworth, C., Lee, S., Reddy, T., Ma, H., and Firtel, R. A. (1999). Chemoattractant-mediated transient activation and membrane localization of akt/pkb is required for efficient chemotaxis to camp in dictyostelium. *The EMBO journal*, 18(8):2092–2105.

Mesibov, R., Ordal, G. W., and Adler, J. (1973). The range of attractant concentrations for bacterial chemotaxis and the threshold and size of response over this range weber law and related phenomena. *The Journal of general physiology*, 62(2):203–223.

Milo, R., Shen-Orr, S., Itzkovitz, S., Kashtan, N., Chklovskii, D., and Alon, U. (2002). Network motifs: simple building blocks of complex networks. *Science*, 298(5594):824–827.

Mitzenmacher, M. (2004). A brief history of generative models for power law and lognormal distributions. *Internet mathematics*, 1(2):226–251.

Monk, P. and Othmer, H. (1990). Wave propagation in aggregation fields of the cellular slime mould dictyostelium discoideum. *Proc. R. Soc. Lond. B*, 240(1299):555–589.

Monk, P. B. and Othmer, H. G. (1989). Cyclic amp oscillations in suspensions of dictyostelium discoideum. *Phil. Trans. R. Soc. Lond. B*, 323(1215):185–224.

Nakagaki, T. (2001). Smart behavior of true slime mold in a labyrinth. *Research in Microbiology*, 152(9):767 – 770.

Nieder, A. and Miller, E. K. (2003). Coding of cognitive magnitude: Compressed scaling of numerical information in the primate prefrontal cortex. *Neuron*, 37(1):149–157.

Noorbakhsh, J., Schwab, D. J., Sgro, A. E., Gregor, T., and Mehta, P. (2015). Modeling oscillations and spiral waves in *Dictyostelium* populations. *Phys. Rev. E*, 91:062711.

Parent, C. A., Blacklock, B. J., Froehlich, W. M., Murphy, D. B., and Devreotes, P. N. (1998). G protein signaling events are activated at the leading edge of chemotactic cells. *Cell*, 95(1):81–91.

Postma, M. and van Haastert, P. J. (2009). Mathematics of experimentally generated chemoattractant gradients. pages 473–488.

Pritchard, J. K., Seielstad, M. T., Perez-Lezaun, A., and Feldman, M. W. (1999). Population growth of human y chromosomes: a study of y chromosome microsatellites. *Molecular Biology and Evolution*, 16(12):1791–1798.

Raj, A. and van Oudenaarden, A. (2008). Nature, nurture, or chance: Stochastic gene expression and its consequences. *Cell*, 135(2):216–226.

Raper, K. B. (1935). Dictyostelium discoideum, a new species of slime mold from decaying forest leaves. *J. Agricul. Res.*, 50:135–147.

Raper, K. B. (1940). Pseudoplasmodium formation and organization in dictyostelium discoideum. *Journal of the Elisha Mitchell Scientific Society*, 56(2):241–282.

Samadani, A., Mettetal, J., and van Oudenaarden, A. (2006). Cellular asymmetry and individuality in directional sensing. *Proceedings of the National Academy of Sciences*, 103(31):11549–11554.

Saran, S., Meima, M. E., Alvarez-Curto, E., Weening, K. E., Rozen, D. E., and Schaap, P. (2002). camp signaling in dictyostelium. *Journal of Muscle Research & Cell Motility*, 23(7-8):793–802.

Sasaki, A. T., Chun, C., Takeda, K., and Firtel, R. A. (2004). Localized ras signaling at the leading edge regulates pi3k, cell polarity, and directional cell movement. *J Cell Biol*, 167(3):505–518.

Sgro, A. E., Schwab, D. J., Noorbakhsh, J., Mestler, T., Mehta, P., and Gregor, T. (2015). From intracellular signaling to population oscillations: bridging size- and time-scales in collective behavior. *Molecular Systems Biology*, 11(1).

Shen-Orr, S. S., Milo, R., Mangan, S., and Alon, U. (2002). Network motifs in the transcriptional regulation network of escherichia coli. *Nature genetics*, 31(1):64–68.

Shlens, J. (2014). A tutorial on principal component analysis. *arXiv preprint arXiv:1404.1100*.

Shoval, O., Alon, U., and Sontag, E. (2011). Symmetry invariance for adapting biological systems. *SIAM Journal on Applied Dynamical Systems*, 10(3):857–886.

Shoval, O., Goentoro, L., Hart, Y., Mayo, A., Sontag, E., and Alon, U. (2010). Fold-change detection and scalar symmetry of sensory input fields. *Proceedings of the National Academy of Sciences*, 107(36):15995–16000.

Siegert, F. and Weijer, C. J. (1995). Spiral and concentric waves organize multicellular dictyostelium mounds. *Current Biology*, 5(8):937–943.

Sims, C. R. (2016). Rate–distortion theory and human perception. *Cognition*, 152:181–198.

Sisson, S. A., Fan, Y., and Tanaka, M. M. (2007). Sequential monte carlo without likelihoods. *Proceedings of the National Academy of Sciences*, 104(6):1760–1765.

Skataric, M., Nikolaev, E. V., and Sontag, E. D. (2014). Fundamental limitation of the instantaneous approximation in fold-change detection models. *IET systems biology*, 9(1):1–15.

Skoge, M., Adler, M., Groisman, A., Levine, H., Loomis, W. F., and Rappel, W.-J. (2010). Gradient sensing in defined chemotactic fields. *Integrative Biology*, 2(11-12):659–668.

Song, L., Nadkarni, S. M., Bödeker, H. U., Beta, C., Bae, A., Franck, C., Rappel, W.-J., Loomis, W. F., and Bodenschatz, E. (2006). Dictyostelium discoideum chemotaxis: threshold for directed motion. *European journal of cell biology*, 85(9-10):981–989.

Sterling, P. and Laughlin, S. (2015). *Principles of Neural Design*. MIT Press.

Strogatz, S. H. (2018). *Nonlinear Dynamics and Chaos with Student Solutions Manual: With Applications to Physics, Biology, Chemistry, and Engineering*. CRC Press.

Sucgang, R., Weijer, C. J., Siegert, F., Franke, J., and Kessin, R. H. (1997). Null mutations of thedictyosteliumcyclic nucleotide phosphodiesterase gene block chemotactic cell movement in developing aggregates. *Developmental biology*, 192(1):181–192.

Sun, T. J. and Devreotes, P. (1991). Gene targeting of the aggregation stage camp receptor car1 in dictyostelium. *Genes & Development*, 5(4):572–582.

Takeda, K., Shao, D., Adler, M., Charest, P. G., Loomis, W. F., Levine, H., Groisman, A., Rappel, W.-J., and Firtel, R. A. (2012). Incoherent feedforward control governs adaptation of activated ras in a eukaryotic chemotaxis pathway. *Science signaling*, 5(205):ra2.

Tomchik, K. and Devreotes, P. (1981). Adenosine 3', 5'-monophosphate waves in dictyostelium discoideum: a demonstration by isotope dilution–fluorography. *Science*, 212(4493):443–446.

Toni, T. and Stumpf, M. P. (2009). Tutorial on abc rejection and abc smc for parameter estimation and model selection. *arXiv preprint arXiv:0910.4472*.

Toni, T., Welch, D., Strelkowa, N., Ipsen, A., and Stumpf, M. P. (2009). Approximate bayesian computation scheme for parameter inference and model selection in dynamical systems. *Journal of the Royal Society Interface*, 6(31):187–202.

Tu, Y., Shimizu, T. S., and Berg, H. C. (2008). Modeling the chemotactic response of escherichia coli to time-varying stimuli. *Proceedings of the National Academy of Sciences*, 105(39):14855–14860.

Tyson, J. J., Chen, K. C., and Novak, B. (2003). Sniffers, buzzers, toggles and blinkers: dynamics of regulatory and signaling pathways in the cell. *Current opinion in cell biology*, 15(2):221–231.

Tyson, J. J. and Murray, J. (1989). Cyclic amp waves during aggregation of dictyostelium amoebae. *Development*, 106(3):421–426.

Usnadze, D. (1931). Über die gewichtstäuschung und ihre analoga. *Psychologische Forschung*, 14(1):366–379.

Van Haastert, P. and De Wit, R. (1984). Demonstration of receptor heterogeneity and affinity modulation by nonequilibrium binding experiments. the cell surface camp receptor of dictyostelium discoideum. *Journal of Biological Chemistry*, 259(21):13321–13328.

Wang, C. J., Bergmann, A., Lin, B., Kim, K., and Levchenko, A. (2012). Diverse sensitivity thresholds in dynamic signaling responses by social amoebae. *Science Signaling*, 5(213):ra17–ra17.

Wei, X.-X. and Stocker, A. A. (2012). Efficient coding provides a direct link between prior and likelihood in perceptual bayesian inference. In *Advances in neural information processing systems*, pages 1304–1312.

Wei, X.-X. and Stocker, A. A. (2015). A bayesian observer model constrained by efficient coding can explain'anti-bayesian'percepts. *Nature neuroscience*, 18(10):1509.

Wei, X.-X. and Stocker, A. A. (2017). Lawful relation between perceptual bias and discriminability. *Proceedings of the National Academy of Sciences*, 114(38):10244–10249.

Weisstein, E. W. (2003). Normal ratio distribution, from mathworld–a wolfram web resource. http://mathworld.wolfram.com/NormalRatioDistribution.html.

Xiong, Y., Huang, C.-H., Iglesias, P. A., and Devreotes, P. N. (2010). Cells navigate with a local-excitation, global-inhibition-biased excitable network. *Proceedings of the National Academy of Sciences*, 107(40):17079–17086.

Yi, T.-M., Huang, Y., Simon, M. I., and Doyle, J. (2000). Robust perfect adaptation in bacterial chemotaxis through integral feedback control. *Proceedings of the National Academy of Sciences*, 97(9):4649–4653.

Zwickl, D. J. and Holder, M. T. (2004). Model parameterization, prior distributions, and the general time-reversible model in bayesian phylogenetics. *Systematic Biology*, 53(6):877–888.